Lawrence Berkeley Laboratory
UNIVERSITY OF CALIFORNIA

Materials & Molecular Research Division

Presented at the 100th Fermi School of Physics, Varenna, Italy, July 8-18,1986; and to be published in the Proceedings

LECTURES ON PULSED NMR

A. Pines

September 1986

Prepared for the U.S. Department of Energy under Contract DE-AC03-76SF00098

DISCLAIMER

LBL-22316

LECTURES ON PULSED NMR*

A. Pines

Materials and Molecular Research Division
Lawrence Berkeley Laboratory
and
Department of Chemistry
University of California
Berkeley, CA 94720

SUMMARY

These lectures discuss some recent developments in pulsed NMR, emphasizing fundamental principles with selected illustrative applications. Major topics covered include multiple-quantum spectroscopy, spin decoupling, the interaction of spins with a quantized field, adiabatic rapid passage, spin temperature and statistics of cross-polarization, coherent averaging, and zero field NMR.

---

*Presented at the 100th Fermi School of Physics, Varenna, Italy, July 1986

TABLE OF CONTENTS

LECTURES ON PULSED NMR

A. Pines

University of California, Berkeley

(Presented at the 100th Fermi School on Physics, Varenna, Italy, July 1986)

1. Introduction

What has made NMR such a prominent and exciting modern spectroscopic technique? One fundamental reason of course is that NMR illustrates some beautiful phenomena in physics, providing "textbook" examples of the coherent interaction of radiation with matter. But there are other reasons as well, related to the practical applications of NMR, which we may assemble into four categories according to the types of information that can be obtained:

1. Site identification. Sites on a molecule (or, for that matter, in a crystal or even on a surface) often can be identified by the different chemical shifts, quadrupolar couplings and other NMR parameters that affect the spectrum. Quantitative measurements of intensities then can provide information on the occupancy of sites, obviously an important question in structure determination.

2. Correlations between sites. Beyond the question of site occupancy (e.g., how many carbons are there of this type or that type), it is possible to investigate relationships between sites by NMR. Such relationships may arise both through structure and through dynamics. On the one hand, we may seek static information, such as bond distances, bond angles, and the sizes of spin clusters; on the other hand, we may wish to study correlated motions

at different sites.

3. Dynamics. NMR is sensitive to motion both through the effects on spectra and through the regulation of relaxation. The range of dynamical phenomena covered by NMR is enormous, from molecular reorientation times of picoseconds to crystal impurity hopping times of hours.

4. Imaging. With NMR it is now possible to observe, non-invasively, cross sections through objects, and thus obtain information about density, flow, and spatially localized chemical composition.

Clearly these four categories of information are invaluable in applications to many areas of science, including biology and medicine. Needed to enjoy these benefits, however, is the ability to record signals with sufficient sensitivity, resolution and selectivity, and then to be able to interpret and analyze the spectra. A number of factors frequently conspire to make this an awkward task. Accordingly, in these lectures I shall discuss some developments that have helped to surmount many of these problems. For instance, when it became practical to introduce large numbers of rf quanta into spin systems, an exciting range of possibilities was opened, many of which are still being actively investigated by several groups. These new techniques are relevant to all four areas mentioned above. For example, sites of quadrupolar nuclei can be identified by high resolution double-quantum NMR; connectivities, correlations, and structures can be established by magnetic couplings in multiple-quantum proton spectra; correlated fluctuations can be studied by multiple-quantum relaxation; and NMR imaging in solids can be facilitated by multiple-quantum methods.

The focus of these lectures is on the fundamental physics, with a few examples of illustrative applications. The topics covered are largely from

areas of research in which our own group has engaged, and they are intended to contribute to the school's framework of fundamental principles of modern pulsed NMR. The subjects treated rely on many concepts and principles (such as density matrix, two-dimensional spectroscopy, quadrupolar operators, coherence, spin temperature, etc.) covered by other lecturers.

Some of the subjects I have been requested to address are: multiple-quantum spectroscopy, two-dimensional NMR in liquid crystals, interaction of spins with a quantized field, adiabatic rapid passage, spin temperature and cross-polarization, coherent averaging, and zero field NMR. I apologize for being unable to do all of them the justice they deserve.I also apologize for any inconsistencies in notation and convention between the different subjects. I have done my best to help my colleagues teaching at this school in providing a consistent and uniform presentation for students who are entering, or working in, the field of NMR applications in biology and medicine, and who wish to acquire some appreciation of the underlying physical principles.

2. Dipolar Couplings and Molecular Structure

In high magnetic field, the dipolar coupling d_{jk} between two spins j and k on a molecule depends on the distance r_{jk} between the spins and on the angle θ_{jk} of the j-k vector relative to the field:

$$d_{jk} \sim \frac{1}{r_{jk}^3} (3\cos^2\theta_{jk} - 1) \qquad (1)$$

Measurements of time-averaged dipolar couplings from the NMR spectrum therefore can provide information about molecular structure and dynamics. **Figure 1** illustrates the sensitivity of NMR spectra to structure by showing an experimental spectrum of benzene oriented in a liquid crystal, as well as simulated spectra for different possible structures of symmetrical six-carbon frameworks. This figure, provided by Z. Luz, demonstrates clearly how precise the determination of the authentic hexagonal structure is in this simple pedagogical case.

3. Onset of Spectral Complexity

The case of benzene, with six proton spins, exemplifies a resolved tractable spectrum of dipolar couplings. The situation rapidly becomes more complex, however, as the number of spins is increased. This effect is illustrated in **Figure 2**, also courtesy of Z. Luz. Beyond eight or so spins, depending on symmetry, an exponential increase in the number of NMR transitions renders the spectrum intractably complex. The case of eight spins is illustrated in **Figure 3**, which shows the spectrum of n-hexane-d_6 (methyls deuterated) in isotropic solution, where the dipolar couplings are averaged to zero and where at this resolution the chemical shifts are essentially the same; and in **Figure 4**, which shows the spectrum of the same

molecule oriented in a liquid crystal, displaying an enormously complex spectrum of dipolar couplings.

A rough estimate of the complexity can be made by looking at **Figure 5**, which shows the energy level diagram for a group of N coupled spins-1/2 in high field. The conventional one-quantum NMR transitions, shown as solid vertical lines, are subject to the selection rule

$$|\Delta M| = 1. \qquad (2)$$

The number of energy levels with magnetic quantum number M is $\binom{N}{N/2+M}$, and if one is restricted to transitions between neighboring M's, then

$$Z_1 = \sum_M \binom{N}{N/2 + M}\binom{N}{N/2 + M+1} = \binom{2N}{N+1} \qquad (3)$$

is an upper bound to the number of one-quantum transitions. For N = 4 this number is 56, for N = 8 it is 11,440, and for N = 12 it is 2,496,144.

4. Simplification by Multiple-Quantum Transitions

Having encountered the problem of spectral complexity, we may also discern in Figure 5 a possible solution. The dashed arrows indicate multiple-quantum transitions, in which several spins flip together subject to the general rule

$$|\Delta M| = n \quad . \qquad (4)$$

As n, the number of quanta, increases, the number of transitions decreases and the spectra therefore should become simpler. The generalization of (3) to n-quantum transitions is

$$Z_n = \binom{2N}{N+n} \quad , \qquad (5)$$

and for zero quantum transitions is

$$Z_o = \left[\binom{2N}{N} - 2^N \right] \quad . \qquad (6)$$

Examining these expressions, we can see that the dependence of the number of transitions on N for high n (n = N, N-1, N-2) is roughly

$$Z_N \sim 1$$

$$Z_{N-1} \sim N \qquad (7)$$

$$Z_{N-2} \sim N^2 \quad .$$

Thus the number of (N-2) quantum transitions is quadratic in the number of spins, and since the maximum number of couplings is

$$Z_d = \frac{N(N-1)}{2} \sim N^2 \quad , \qquad (8)$$

the (N-2) and (N-1)-quantum spectra should contain sufficient information to determine the d_{jk}.

5. **Analogy to Chemical Isotopic Labeling**

There are other ways to simplify spectra. One conceptually simple but synthetically demanding method is to isotopically label spins at selected positions in the molecule. For example, deuteration of all but two positions on a molecule dramatically reduces the number of lines in the proton spectrum and thus facilitates the direct determination of the d_{jk}'s. We may then ask about the relationship of this simplification to the simplification realized in multiple-quantum spectra. Note that the number of isotopically substituted species with single labels is at most N and that the number of isotopically doubly labeled species is at most N(N-1)/2 - the same order as the number of (N-1) and (N-2)-quantum transitions, respectively. In effect, when we flip N-1 out of N spins, the remaining

spin (or, equivalently, the one labeled spin) can be in any one of N positions. When we flip N-2, the remaining two can be in N(N-1)/2 configurations. Hence the N-p quantum spectrum is a superposition of spectra from all possible arrangements of p isotopic labels.

As an example, consider oriented benzene, whose one-quantum spectrum was shown in Figure 1. The 6-quantum spectrum should contain one line, since there is only one way to absorb six quanta and thereby flip all six spins. The 5-quantum spectrum arises from, roughly speaking, flips of five spins in the field of a sixth. Since this last spin may be up or down, and since all positions on the molecule are equivalent, the 5-quantum spectrum should contain just one doublet. In general there will be a doublet for each inequivalent position or each different singly labeled species. Next we have the 4-quantum spectrum, which involves the flip of four spins in the field of the remaining two. These two can be ORTHO, META or PARA (the three doubly labeled isomers), so we expect three triplets (seven lines). **Figure 6** clearly shows these predictions realized in the multiple-quantum NMR spectra of oriented benzene.

6. Obtaining Multiple-Quantum Spectra

Since multiple-quantum transitions are not directly observable with an NMR coil, they must be detected indirectly by two-dimensional spectroscopic methods, as described in the lectures by Ernst. The general scheme of such an experiment is

$$\text{Preparation}(\tau)\text{-Evolution}(t_1)\text{-Mixing}(\tau')\text{-Detection}\ (t_2)\ . \qquad (9)$$

During the time period t_2, direct detection of allowed one-quantum frequencies provides information about the multiple-quantum frequencies in the earlier time period t_1. The two-dimensional Fourier transform spectrum then displays the directly detected one-quantum spectrum parallel to the frequency axis ω_2 and the multiple-quantum spectrum parallel to the frequency axis ω_1. An example is shown in **Figure 7.** The multiple-quantum spectrum of Figure 6 is the projection of such a two-dimensional spectrum, in absolute value mode, onto the ω_1 axis. Figure 7b clearly shows the seven four-quantum lines of benzene and their connections to the one-quantum transitions. To obtain uniform multiple-quantum intensities, multiple-quantum spectra are typically averaged over a range of values of the excitation time τ ($= \tau'$).

7. Theory of Multiple-Quantum NMR: Preliminaries

Since we will be interested only in the multiple-quantum spectrum, that is, the projection onto the ω_1 axis, we need detect just the integrated ω_2 signal, which is given by the value of the magnetization at the first point ($t_2 = 0$). Furthermore, since the system usually begins in equilibrium at high temperature and in high field, where its density operator is proportional to I_z, we shall find it convenient to monitor I_z at $t_2 = 0$ following the mixing. This formulation, outlined in **Figure 8**, frames the problem in its most symmetric form with no loss of generality. **U** is the preparation propagator, $\mathbf{L}(t_1)$ the evolution propagator, and **V** the mixing propagator. The value of $\langle I_z \rangle$ is detected at $t_2 = 0$ as a function of t_1. For simplicity, I suppress the subscript in t_1 and write t, since only this one dimension will be relevant for the remaining discussion.

In general, the initial quantum statistical state of a system is characterized by a density operator $\rho(0)$, which we depict as a ket $|\rho(0)\rangle$ (and its dual bra $\langle\rho(0)|$) in Liouville space. Under the influence of a propagator $\mathbf{L}(t)$ the system develops into a state $|\rho(t)\rangle$; i.e.,

$$|\rho(t)\rangle = \mathbf{L}(t)|\rho(0)\rangle \ . \tag{10}$$

Diagrammatically, this transformation looks as follows:

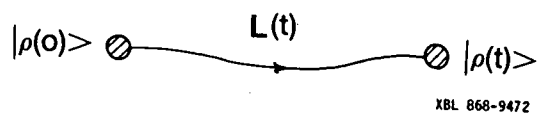

XBL 868-9472

(11)

$\mathbf{L}(t)$ is a superoperator, or superpropagator, which I will continue to term propagator for short. (This usage should be distinguished from the propagator $L(t)$ that acts on quantum mechanical kets in Hilbert space; context will normally render this distinction evident, but for clarity, superoperators will be denoted in bold type.) $\mathbf{L}(t)$ derives from the Hamiltonian superoperator or Liouvillian $\mathbf{H}$ by

$$\mathbf{L}(t) = T \exp\left((-i/\hbar \int_0^t \mathbf{H}(t')dt'\right) \ , \tag{12}$$

where T is a time ordering operator.

I remind you that the density operator

$$\rho = \overline{|\psi\rangle\langle\psi|} \tag{13}$$

is the ensemble average of the projectors of the states ψ for the constituent members of the ensemble, and furthermore that the ensemble

average expectation value of any observable Q (what we measure or observe) is given by

$$\overline{\langle Q \rangle} = \mathrm{Tr}\ (\rho Q) = \langle \rho | Q \rangle \quad , \tag{14a}$$

where

$$\langle A | B \rangle = \mathrm{Tr}\ A^{\dagger} B \tag{14b}$$

is the scalar product in Liouville space.

8. **Multiple-Quantum Signal**

We shall be concerned with the detection of the normalized signal $\langle I_z \rangle$ as a function of evolution time t - the multiple-quantum free induction decay F(t). Of course τ and τ' will be parameters in F(t) as well. In the superoperator notation, the state of the system $|\rho(t)\rangle$ at the end of the mixing in the scheme of Figure 8 is given by

$$|\rho(t)\rangle = \mathbf{V}(\tau')\mathbf{L}(t)\mathbf{U}(\tau)|\rho(0)\rangle. \tag{15}$$

If we now assume a high temperature, high field equilibrium initial condition,

$$|\rho(0)\rangle = |I_z\rangle \quad , \tag{16}$$

and detect $\langle I_z \rangle$, then (15) yields the multiple-quantum free induction decay

$$F(t) = \frac{\langle I_z | \mathbf{V}(\tau')\mathbf{L}(t)\mathbf{U}(\tau) | I_z \rangle}{\langle I_z | I_z \rangle} \quad . \tag{17}$$

Henceforth, I take the signal to be normalized, ($\langle I_z | I_z \rangle = 1$), so that

$$F(t) = \langle I_z | \mathbf{V}(\tau')\mathbf{L}(t)\mathbf{U}(\tau) | I_z \rangle \quad . \tag{18}$$

So now you see the general rule with superoperators: begin on the right with a ket for the original state, propagate from right to left, and end on

the left with a bra for the detected state. From (18), given the Hamiltonians for the three periods (τ, t, τ'), F(t) can be evaluated, and from the Fourier transform of this signal the multiple-quantum spectrum can be obtained. Let us examine some examples.

9. Special Case: One-Quantum FID Point-by-Point

First we consider a "normal" one-quantum free induction decay (FID) within the framework of Figure 8 and (18). In such a normal FID, the transverse magnetization, say $\langle I_x \rangle$, is detected directly. Permit me to assume, however, that we perform the experiment in a silly way - indirectly and point-by-point - by making $\mathbf{U}(\tau)$ a $(\pi/2)_y$ pulse, $\mathbf{V}(\tau')$ a $(\pi/2)_{\bar{y}}$ pulse, and then detecting $\langle I_z \rangle$. This procedure is equivalent to detecting $\langle I_x \rangle$ versus t. The scheme of Figure 8 then becomes

$$\mathbf{P} - t - \mathbf{P}^{\dagger} - \text{detect } \langle I_z \rangle \quad , \tag{19}$$

where $\mathbf{P}$, $\mathbf{P}^{\dagger}$ are the $\pi/2$ pulse superoperators. We now insert these expressions into (18) and expand in a basis set of kets in Liouville space. Here several basis sets can be considered - fictitious spin operators, product operators, spherical tensors or multipole operators, and eigenoperators. The non-Hermitian eigenoperators of $\mathbf{L}(t)$, $|j\rangle\langle k|$, are in fact particularly well suited to these problems. For $j \neq k$ these correspond to coherences and for $j = k$ they correspond to populations. We represent the eigenoperators of $\mathbf{L}(t)$ as kets written $|j\text{-}k\rangle$, so that

$$\mathbf{L}(t)|j\text{-}k\rangle = e^{-i\omega_{jk}t}|j\text{-}k\rangle \quad , \tag{20}$$

where ω_{jk} is the frequency of the transition between eigenstates j and k of the (time-independent) evolution Hamiltonian. Hence we have

$$F(t) = \langle I_z | \mathbf{P}^\dagger \mathbf{L}(t) \mathbf{P} | I_z \rangle$$
$$= \sum_{j,k} \langle I_z | \mathbf{P}^\dagger | j-k \rangle \langle j-k | \mathbf{L}(t) | j-k \rangle \langle j-k | \mathbf{P} | I_z \rangle \quad . \quad (21)$$

We now use (20) and evaluate the other matrix elements in (21), for example,

$$\langle j-k | \mathbf{P} | I_z \rangle = \mathrm{Tr}\{ |k\rangle\langle j| P I_z P^\dagger \}$$
$$= \langle j | P I_z P^\dagger | k \rangle = (P I_z P^\dagger)_{jk} = I_{xjk} \quad , \quad (22)$$

where I_{xjk} is the (j,k)th matrix element of the operator I_x. In this way, (21) yields finally the well known result

$$F(t) = \sum_{jk} |I_{xjk}|^2 e^{-i\omega_{jk}t} \quad , \quad (23)$$

with its Fourier transform,

$$G(\omega) = \sum_{jk} |I_{xjk}|^2 \delta(\omega - \omega_{jk}) \quad , \quad (24)$$

giving the spectrum of $\langle I_x | I_x(t) \rangle$ - the time autocorrelation function of I_x. The spectrum yields the one-quantum frequencies since $I_{xjk} \neq 0$ only for one-quantum transitions; consequently, we term I_x a one-quantum operator. An important point to note is that we obtain all lines in phase because of the appearance of squares of the absolute magnitudes of $(P I_z P^\dagger)_{jk} = I_{xjk}$.

10. General Case: Multiple-Quantum FID

We now expand (18) in the $|j-k\rangle$ basis set for general **U**, **V** to obtain

$$F(t) = \langle I_z | \mathbf{V}(\tau') \mathbf{L}(t) \mathbf{U}(\tau) | I_z \rangle$$

$$= \langle I_z | \mathbf{V}(\tau') | j-k \rangle \langle j-k | \mathbf{L}(t) | j-k \rangle \langle j-k | \mathbf{U}(\tau) | I_z \rangle$$

$$= \sum_{jk} (I_z(-\tau'))_{kj} (I_z(\tau))_{jk} e^{-i\omega_{jk}t} \quad , \tag{25}$$

where

$$I_z(\tau) = U(\tau) I_z U^{\dagger}(\tau)$$

and (26)

$$I_z(-\tau') = V^{\dagger}(\tau') I_z V(\tau')$$

are the effective preparation and mixing operators. These operators, however, are multiple-quantum, unlike I_x. As a consequence, the phases vary from line to line since $(I_z(-\tau'))_{kj}(I_z(\tau))_{jk}$ are, in general, <u>complex</u> numbers.

As an example, consider the simplest and most widely used multiple-quantum sequence, the three pulse sequence

$$(\tfrac{\pi}{2})_y - \tau - (\tfrac{\pi}{2})_{\bar{y}} - t - (\tfrac{\pi}{2})_y - \text{ detect } \langle I_x \rangle \quad . \tag{27}$$

In the present framework, if the detection is to be matched to the preparation so that $\tau = \tau'$, then an additional $(\pi/2)_{\bar{y}}$ pulse must be inserted a time τ after the third $(\pi/2)_y$ to create

$$\mathbf{U}(\tau) = \mathbf{V}(\tau) \quad . \tag{28}$$

Here both **U** and **V** derive from the Hamiltonian H_{xx}, transformed by the y pulses from the normal bilinear (e.g. dipolar) Hamiltonian H_{zz}.

Inserting (28) into (25) yields

$$F(t) = \sum_{jk} (I_z(\tau)_{jk})^2 \, e^{-i\omega_{jk}t} \quad . \tag{29}$$

Note that we have $(\ )^2$ not $|\ |^2$ for the matrix element in (29). For closely spaced multiple-quantum lines, the arbitrary phases will cause a cancellation of intensity, a crucial problem in complex molecules and solids that is illustrated schematically in **Figure 9a.**

11. Time-Reversal Detection

One solution to the phase problem mentioned above follows from the realization that the integrated intensity of the multiple-quantum frequency spectrum is given by the first point, F(t = 0), of the free induction decay; i.e.,

$$F(0) = \langle I_z | \mathbf{V}(\tau')\mathbf{U}(\tau) | I_z \rangle \quad . \tag{30}$$

Clearly, if we ensure that

$$\mathbf{V}(\tau')\mathbf{U}(\tau) = \mathbf{1} \quad , \tag{31}$$

then we recover the full intensity, with all the lines necessarily in phase. This phasing happened naturally in the one-quantum case of (23), and for the multiple-quantum case the same effect can be achieved if the Hamiltonian for the preparation period τ is the negative of that for the mixing period τ', namely

$$\mathbf{V}(\tau') = \mathbf{U}^{\dagger}(\tau) \quad . \tag{32}$$

Given (32), we can evaluate (25) as

$$F(t) = \sum_{jk} |(I_z(\tau))_{jk}|^2 \, e^{-i\omega_{jk}t} \tag{33}$$

to yield "in-phase" lines with maximum integrated intensity, as depicted schematically in **Figure 9b.** (We shall see later that a more general condition, allowing all lines within a multiple-quantum order to be in

phase, is also possible.)

12. **Effect of Phase Shifts**

Consider the effect of a phase shift of ϕ, i.e., a rotation by ϕ around the z axis. For example, if $\mathbf{U}(\tau)$ derives from a secular (high field) Hamiltonian plus rf pulses, then such a phase shift is induced by changing the phases of all rf pulses by ϕ. We define

$$\mathbf{U}_\phi = \mathbf{R}_z^\dagger(\phi)\mathbf{U}\mathbf{R}_z(\phi) \quad , \tag{34}$$

where $\mathbf{R}_z(\phi)$ is a z rotation superoperator

$$\mathbf{R}_z(\phi) = \exp(-i\phi\mathbf{I}_z) \quad , \tag{35}$$

and we see that its effect on the eigenoperators is obviously

$$\mathbf{R}_z(\phi)|j\text{-}k\rangle = e^{-i\phi n_{jk}}|j\text{-}k\rangle \quad , \tag{36}$$

where

$$n_{jk} = M_k - M_j \tag{37}$$

is the number of quanta, or order, of the coherence or transition j-k. Thus, as we might expect, a phase shift of ϕ in any radiation inducing multiple-quantum transitions will be "seen" by a n-quantum transition as $n\phi$.

Suppose we now perform a multiple-quantum experiment with time-reversal detection as in section 11 but modify (32) to obtain

$$\mathbf{U}(\tau) = \mathbf{V}_\phi^\dagger(\tau) = \mathbf{R}_z^\dagger(\phi)\mathbf{V}^{\dagger(\tau)}\mathbf{R}_z(\phi) \quad , \tag{38}$$

so that the phase of the preparation sequence is shifted by ϕ. Inserting this propagator into (25) and using (36), we find that (32) now becomes

$$F_\phi(t) = \sum_{jk} |I_z(\tau)_{jk}|^2 \, e^{-i\omega_{jk}t} \, e^{-i\phi n_{jk}} \quad . \tag{39}$$

Thus each complete n-quantum spectrum is phase shifted by $n\phi$. For $t = 0$, we have

$$F_\phi(0) = \sum_{jk} |I_z(\tau)_{jk}|^2 \, e^{-i\phi n_{jk}} \quad , \tag{40}$$

so the integrated intensities of the multiple-quantum spectra for each τ may be determined by Fourier transformation with respect to ϕ. This determination may be made more efficiently by varying ϕ proportionately to τ to yield the full τ dependence of the n-quantum intensities in one experiment.

13. Time Proportional Phase Incrementation (TPPI)

The phase behavior above provides a convenient way to separate multiple-quantum coherences from each other (as shown for example in the benzene spectrum of Figure 6.) In (39), if we set

$$\phi = \Delta\omega t \quad , \tag{41a}$$

then we have

$$F(t) = \sum_{jk} |I_z(\tau)_{jk}|^2 \, e^{-it(\omega_{jk} + \Delta\omega n_{jk})} \quad , \tag{41b}$$

so each n-quantum line is shifted by $n\Delta\omega$, thereby allowing a clear separation of orders in one experiment.

14. Double-Quantum NMR in Solids

An area where double-quantum NMR has played a useful role is in spin I = 1 systems, e.g., deuterium. The appropriate energy level diagram is

depicted in **Figure 10.** Owing to electric quadrupolar coupling the non-spherical deuterium nucleus experiences an orientation dependent splitting of its resonance lines leading to broad powder signals (~100 kHz) in solids, as described in the lectures by Bloom. This inhomogeneous broadening obscures the small chemical shifts. It is pleasant to realize, however, that this problem can be overcome by detecting the double-quantum spectrum (transitions between M = ±1), which is unencumbered by electric quadrupole broadening. This approach allowed the first measurement of the chemical shielding anisotropy (~-6ppm) of hydrogen in benzene. An example of these effects is provided in **Figures 11** and **12,** which show the double-quantum free induction decay and spectrum of solid benzene-d_1. The double-quantum coherence was prepared by irradiating the center of the spectrum with a weak pulse, for which the rf amplitude ω_1 is much less than the quadrupole coupling ω_Q, resonant only with the double-quantum transition at ω_0. The effective $\pi/2$ pulse is then characterized by the condition

$$\frac{\omega_1^2}{\omega_Q}\tau = \frac{\pi}{2} \quad , \tag{42}$$

where τ is the pulse length. I shall expand on this idea later when we get to double-quantum decoupling in section 23 and double-quantum excitation in section 32.

The double-quantum transition of a single spin I = 1 is analogous to the full N-quantum spectrum of N coupled spins-1/2. We recall that an N-quantum spectrum arises from just one transition, unaffected by any spin-spin couplings.

15. Double-Quantum Spin Locking

Spin locking is a widely used technique for extending the lifetimes of coherences in the rotating frame, and is essential in various relaxation and cross-polarization experiments. It can be performed by applying a $(\pi/2)_y$ rf pulse to the z magnetization, and then shifting the rf phase by $\pi/2$ to x while irradiating continuously. The magnetization is thus aligned along the rf field, hence the term locking. The decay of the magnetization order now depends on spin-lattice processes in the rotating frame. An appealing question is whether one can lock double-quantum coherence in a similar fashion, even though the one-quantum spectrum may be extremely broad. In other words, can we create double-quantum coherence and then apply radiation to lock it? Suppose the double-quantum coherence is prepared with a weak pulse applied at the center of the resonance. From the discussion in section 11 we know a $\pi/4$ phase shift in the radiation is needed to deliver an effective phase shift of $\pi/2$ to the double-quantum transition. A pictorial representation of this behavior appears in **Figure 13.** The dipolar one-quantum coherences of Figure 13(a) act like vectors (i.e., first rank tensors), which are shown in the diagram as p_x and p_y orbitals that are created from a p_z orbital representing the equilibrium magnetization. In these circumstances, a $\pi/2$ phase shift takes p_x into p_y. The quadrupolar double-quantum coherences of Figure 13(b), however, act like second rank tensors - $d_{x^2-y^2}$ and d_{xy} orbitals. A $\pi/4$ phase shift interchanges these orbitals, whereas a $\pi/2$ phase shift changes their signs. (Here recall our earlier discussion of time reversal.)

The extension of a double-quantum free induction decay time from a few hundred microseconds to a few milliseconds by a spin locking experiment of

this sort is shown in **Figure 14.** The technique has been used in double-quantum cross-polarization of broad deuterium and nitrogen-14 resonances in solids.

Of course these types of coherence do not occur exclusively in spin systems, but rather they are a general manifestation of the superposition of stationary states, which results in real or fictitious multipolar oscillations. For example, as shown in **Figure 15,** a coherent superposition between the ψ_0 and ψ_1 states of a one-dimensional harmonic oscillator exhibits "dipolar-like" oscillations, and a coherent superposition between the ψ_0 and ψ_2 states exhibits "quadrupolar-like" oscillations as the superpositions evolve between the $\pm$ combinations.

16. Molecular Structure by Multiple-Quantum NMR

In our previous discussions of multiple-quantum NMR, oriented benzene served as a convenient pedagogical prototype. Another example, perhaps closer to "real life", is given in **Figure 16,** which shows the normal one-quantum spectrum of a cyanobiphenyl liquid crystal molecule containing 8 protons. The result is to be contrasted with the six-quantum spectrum in **Figure 17,** where an analysis of the spectrum in terms of dipole couplings may be made to study the structure and dynamics of this flexible molecule. Using the structure,

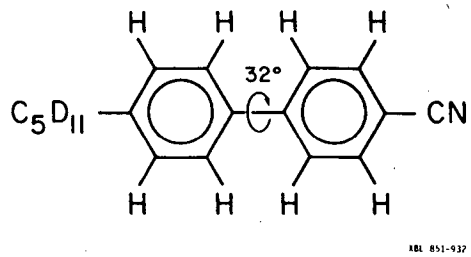

with jumps between the four equivalent conformations, the five-quantum

spectrum can also be simulated, and this spectrum is compared with experiment in **Figure 18.**

A further application of multiple-quantum methods combines multiple-quantum filtering with two-dimensional correlation spectroscopy to investigate randomly deuterated molecules in liquid crystals. This method allows a separation of the different proton-containing isotopomers in situations where the normal proton spectra might be too complex (recall, for example, hexane-d_6 in Figure 4). An example of such simplified spectra, obtained for 80% randomly deuterated hexane is shown in **Figure 19.** Spectrum 19(a) was obtained with the pulse sequence

$$(\tfrac{\pi}{2})_\phi - t_1 - (\tfrac{\pi}{2})_\phi - \tfrac{\tau_1}{2} - \pi_x - \tfrac{\tau_1}{2} - (\tfrac{\pi}{2})_x - \tfrac{\tau_2}{2} - \pi_x - \tfrac{\tau_2}{2} - \text{sample} \quad (43a)$$

where ϕ is incremented in 90° steps while alternating the detector phase between 0° and 180° and increasing τ_1 after every fourth shot to reduce contributions from three-spin systems. Spectrum 19(b) was obtained with the sequence

$$(\tfrac{\pi}{2})_\phi - \tfrac{\tau_1}{2} - \pi_\phi - \tfrac{\tau_1}{2} - (\tfrac{\pi}{2})_\phi - t_1 - (\tfrac{\pi}{2})_x - \tfrac{\tau_2}{2} - \pi_x - \tfrac{\tau_2}{2} - \text{sample}, \quad (43b)$$

where ϕ and the detector are again cycled. In this way, all 16 dipolar couplings of oriented hexane have been determined and partly assigned to positions on the molecules. Note that hexane is a formidable spin system, with 14 strongly coupled protons, and that its conventional spectrum is considerably more complex than that shown in Figure 4. This technique should help determine conformational dynamics of flexible molecules of this kind, and may be extended to molecules of biological interest.

17. Selective n-Quantum Excitation

High n-quantum transitions, though desirable, generally are of annoyingly low intensity. This problem can be partly overcome, however, by selective n-quantum excitation, under which a phase shifted string of sequences with propagators U_ϕ

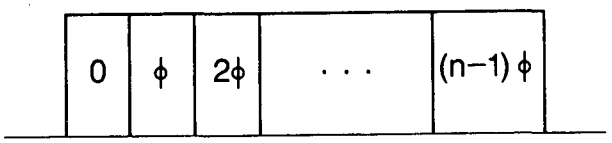

XBL-866-6351

(44a)

is concatenated.

The total propagator U_T is given by

$$U_T = U_{(n-1)\phi} \cdot \cdot \cdot \cdot \cdot U_\phi U_0 \quad , \tag{44b}$$

with each U_ϕ obtained from a basic U_0 by transformation (34). If $\phi = 2\pi/n$, then only n-quantum operators survive in the overall propagator, thereby making the propagator n-quantum selective. But in order for this selectivity to be achieved **U** must contain n-quantum operators. One approach is to construct a "sandwich"

$$U_0 = Q^\dagger U Q \tag{44c}$$

where **U** describes a brief excitation and **Q** and $Q^\dagger$ describe a pair of lengthy sequences, related by time reversal, which induce multiple-quantum operators in **U**. An example of selective excitation of the 4-quantum spectrum of oriented benzene is shown in **Figure 20.**

Selective excitation can be viewed in the frequency domain as shown in **Figures 21** and **22.** Two-quantum excitation involves phase shifts of $2\pi/2 = \pi$, i.e. 0, π, 0, π, 0, π... This operation is symmetric in time and yields

a symmetric nearest sideband structure about the resonance at ω_0 in Figure 21. The first resonant process is a 2-quantum transition involving one photon from each sideband. The phase shifts of $2\pi/3$ for 3-quantum excitation yield the sequence 0, $2\pi/3$, $4\pi/3$, 0, $2\pi/3$, $4\pi/3$, ... with the unsymmetrical nearest sideband disposition shown in Figure 22. The first resonant process must now involve two photons from one sideband and one from the other. Bear in mind that this is a linear Fourier argument for the obviously nonlinear process of multiple-quantum excitation, so it is wrong in general. Nevertheless, it prescribes the correct symmetry and is useful if carefully applied.

18. **Multiple-Quantum NMR in Solids**

Time reversal detection as described in section 11 is necessary in solids because the transition frequencies are distribute almost continuously. Consequently, there is an essentially complete cancellation of intensity if the phases of the lines are random, as in Figure 9(a). An alternative view of the same problem is depicted in **Figure 23.** Suppose we use the normal three pulse sequence (27) to excite and observe multiple-quantum transitions in a solid. The integrated intensity of the multiple-quantum spectrum is given by the initial amplitude of the magnetization sampled in t_2 when $t_1 = 0$. But in a solid, after long τ the magnetization will have decayed to zero and hence little or no multiple-quantum intensity will be observed.

Using the appropriate time reversal detection, however, we can indeed obtain solid-state spectra with high n - in excess of 100 quanta. An example of a suitable time reversal excitation experiment is shown in **Figure**

24. The two pulses of the simple excitation sequence are replaced by a train of pulses whose average Hamiltonian (see section 39) is given by

$$H_{DQ} = (H_{xx} - H_{yy})/3 \tag{45}$$

where DQ denotes a pure double quantum operator. The nonsecular Hamiltonian H_{xx} was mentioned in section 10.

If the phases of the x and $\bar{x}$ rf pulses in the lower sequence of Figure 24 are all shifted by $\pi/2$ to y and $\bar{y}$ pulses, then we simply exchange the x and y indices in (45) and obtain

$$R_z^{\dagger}(\tfrac{\pi}{2})H_{DQ}R_z(\tfrac{\pi}{2}) = -(H_{xx} - H_{yy})/3 \quad . \tag{46}$$

Hence, from (12), the unitary propagator **U** is shifted to its adjoint

$$\mathbf{U} \longrightarrow \mathbf{U}^{\dagger} \quad , \tag{47}$$

as required for detection by (32) or by (38) for use with TPPI.

Figure 25 shows multiple-quantum spectra obtained in solid hexamethylbenzene for different preparation and mixing times τ with the lower sequence of Figure 24. Solid hexamethylbenzene is an essentially infinite network of coupled spins, so we expect the multiple-quantum absorption to increase continuously with τ. If at any given τ we consider that a finite cluster of spins, say N, has become involved, then, from (5), the integrated intensity of the n-quantum transitions should go approximately as

$$Z_n = \binom{2N}{N+n} \sim \frac{4^N}{(N\pi)^{1/2}} e^{-n^2/N} \tag{48}$$

according to Stirling's approximation for large N and $n \ll N$. So we expect a roughly Gaussian distribution of intensities, a prediction borne out well

in **Figure 26**, where even-order multiple-quantum spectra from a finite cluster of 21 spins are shown. The time dependence of the Gaussian width, also shown in Figure 26, can provide information on the distribution of atoms in materials, as depicted schematically in **Figure 27**. This method should be particularly useful for the study of clusters and, indeed, preliminary results have been realized in a number of cases, including liquid crystals, organic and inorganic solids, molecules in zeolite cavities, hydrogen in amorphous semiconductors, and molecules adsorbed on metal surfaces.

19. Selection Rules in Multiple-Quantum Dynamics

If the pure double-quantum Hamiltonian (45) is used for preparation and detection, then for $\rho(0) = I_z$ only even quantum transitions are excited. If we characterize the dynamical evolution of the system by the number of spins N and the number of quanta, or coherence order, n then the dynamical selection rules

$$\Delta N = \pm 1$$

and (49)

$$\Delta n = \pm 2$$

are imposed. With the initial condition for $\rho(0) = I_z$

$$N = 1 \qquad (50)$$

$$n = 0 \quad ,$$

the states (N = 4, n = 4), (N = 8, n = 8),... are not accessible, i.e., we have the surprising consequence that it should not be possible to observe 4-quantum coherence in a 4 spin system, etc. A detailed study of such multiple-quantum dynamics has been made by Mehring and Munowitz and will be

published shortly.

20. Heteronuclear Double-Quantum Coherence

Techniques related to multiple-quantum NMR frequently are useful for heteronuclear spectroscopy in isotropic liquids. Bilinear rotation decoupling (BIRD), a method for the homonuclear decoupling of protons in weakly coupled liquid spin systems, can be thought of as follows. Suppose a hard π pulse is applied to all protons and a heteronuclear double-quantum π pulse is then applied to directly coupled carbon-13 proton pairs. This selective pulse restores to +z all proton spins coupled directly to carbon-13. The net effect is to invert all other spins, thus enabling them to be decoupled.

A pulse sequence that induces the double-quantum or bilinear rotation is

$$\begin{array}{ll} \mathbf{I}\ (^{1}\mathrm{H}) & \left(\frac{\pi}{2}\right) - \frac{\tau}{2} - \pi - \frac{\tau}{2} - \left(\frac{\pi}{2}\right) \\ \mathbf{S}\ (^{13}\mathrm{C}) & \qquad\qquad\quad \pi \end{array} \qquad (51a)$$

If the Hamiltonian for the coupled I-S system is $H_{IS} = JI_zS_z$ then (51a) produces a propagator of the form $U(\tau) = \exp(-i2\pi\tau I_yS_z)$. For $\tau = 1/J$ this propagator is a π pulse only for the directly bonded (satellite) protons.

A further use of heteronuclear multiple-quantum coherence is to obtain sharp NMR spectra in the presence of inhomogeneous magnetic fields or susceptibility broadening. One technique, termed SHARP, uses echoes during the evolution of carbon-13 or nitrogen-15 coherence in the presence of coupled protons. This procedure should be useful in spatially selective NMR of heteronuclear systems with two rf coils, in particular where the relevant spatial region is in an inhomogeneous field or broadened by magnetic

susceptibility effects. An example, shown in **Figure 28,** demonstrates a simple version of spatial selectivity and high resolution with a surface coil on tubes containing ethanol and alanine. The pulse sequence used for this experiment was

$$\begin{array}{lll} \mathbf{I} & (^1H) & (\frac{\pi}{2})_x - \frac{\tau}{2} - \pi - \frac{\tau}{2} - x(\frac{4t_1}{5}) - \frac{\tau'}{2} - \pi - \frac{\tau'}{2} - \frac{t_1}{5} - \text{sample}(\pm) \\ \mathbf{S} & (^{13}C) & \pi \qquad\qquad \frac{\pi}{2}(\pm) - \frac{\pi}{2} \qquad\qquad \pi \qquad\qquad \pi \end{array} \tag{51b}$$

where $x(4t_1/5)$ implies continuous irradiation and the $\pm$ indicate that signals from experiments differing by 180° in phase are subtracted to further suppress non-satellite peaks.

21. **Comment on Relationship of Spatially Selective Pulses to Zero Field NMR**

I'd like to make a brief comment on the connection between spatial selectivity with a surface coil (mentioned also in the lectures of Styles) and a seemingly unrelated area - Zero Field NMR. In normal high field NMR we are accustomed to exciting and detecting the NMR of different spins (e.g. ^1H, ^{13}C,...) separately and selectively according to their different frequencies. If we wish to work with protons we may use 400 MHz, for example, and for carbon-13 we would then use 100 MHz. In zero field, however, all basic resonance frequencies are zero. So how do we differentiate between different species? The answer is that we use the magnetogyric ratio, which is analogous to the rf amplitude ω_1 in high field NMR. If we apply <u>DC</u> pulses the spins respond differently according to their magnetogyric ratios. But is this notion not identical to the idea of spatial selectivity using a surface coil with composite pulses in high field

NMR? The two tubes in Figure 28 experience different ω_1 fields and this distinction is what is often used to label such regions. So some of this work in spatial selectivity has been useful in Zero Field NMR, a topic about which I shall say a few words at the end.

22. Spin Decoupling

To prepare for the case of double-quantum decoupling let us first consider the decoupling of a spin I = 1/2 from an observed spin S = 1/2. The I spin is irradiated near resonance with an rf field of amplitude ω_1. In the rotating frame the Hamiltonian is

$$H = H_0 + H_{IS} \quad , \tag{52}$$

where

$$H_0 = -\Delta\omega I_z - \omega_1 I_x \quad , \tag{53}$$

describes the I fields in the rotating frame in frequency units and

$$H_{IS} = dI_z S_z \tag{54}$$

is the I - S coupling. We now transform to a tilted frame with z along the effective I field. The tilt operator is given by

$$T = \exp(-i\theta I_y) \quad , \tag{55}$$

where

$$\cos\theta = \frac{\Delta\omega}{(\omega_1^2 + \Delta\omega^2)^{1/2}} = \frac{\Delta\omega}{\omega_e} \quad . \tag{56}$$

In this frame

$$H = -\omega_e I_z + dS_z(I_z\cos\theta - I_x\sin\theta)$$
$$\omega_e = (\omega_1^2 + \Delta\omega^2)^{1/2} \quad . \tag{57}$$

We now go into a frame defined by $-\omega_e I_z$ and take the average Hamiltonian (see section 39) of the I-S coupling term, obtaining

$$\bar{H}_{IS}^{(0)} = d\cos\theta S_z I_z \tag{58}$$

$$\bar{H}_{IS}^{(1)} = d^2\sin\theta \frac{1}{\omega_e} S_z{}^2(\cos I_x - \frac{1}{2}\sin\theta I_z) \quad , \tag{59}$$

and, at resonance ($\Delta\omega = 0$, $\theta = \pi/2$),

$$\bar{H}_{IS}^{(2)} = -\frac{d^3}{2\omega_1^2} S_z^3 I_x \quad . \tag{60}$$

For a spin S = 1/2 the term $\bar{H}_{IS}^{(1)}$ in (59) commutes with the spin vector $\underset{\sim}{S}$ so only $\bar{H}_{IS}^{(0)}$ and $\bar{H}_{IS}^{(2)}$ are relevant.

Away from resonance, where $\Delta\omega \neq 0$, the effective coupling between I and S is dominated by $\bar{H}_{IS}^{(0)}$, and the decoupling efficiency δ_s (roughly the relative S linewidth) goes as

$$\delta_s \sim \cos\theta = \frac{\Delta\omega}{(\omega_1^2 + \Delta\omega^2)^{1/2}} \quad . \tag{61}$$

Thus for small $\Delta\omega$, more precisely $d \ll \Delta\omega \ll \omega_1$, the S linewidth should depend linearly on $\Delta\omega$.

At resonance ($\Delta\omega = 0$) the dominant term is $\bar{H}_{IS}^{(2)}$, and we expect

$$\delta_s \sim (\frac{d}{\omega_1})^2 \quad , \tag{62}$$

i.e., the decoupling efficiency should increase (the S linewidth should

decrease) inverse quadratically with ω_1 ($\delta_S \sim 1/\omega_1^2$) for large ω_1.

I note here that the cosθ factor is a scaling of an I_z term analogous to scaling of chemical shifts or resonance offsets due to strong irradiation off resonance. We have recognized that this scaling originates from the same source as the "mysterious" geometrical phase factor in certain closed circuit adiabatic processes.

23. **Double-Quantum Decoupling**

Imagine that we are required to decouple a spin I = 1, say a deuterium spin, from a spin S = 1/2, say a proton. Such would be the case, for example, in experiments on large biological molecules where isotopic substitution has been performed in order to simplify the spin system. If the deuterium quadrupole splitting is large (recall Figure 10), it may be impossible to cover the full I spectrum with a sufficiently large ω_1 field. However, if we irradiate at the unperturbed Zeeman resonance $\omega = \omega_0$, then the double-quantum transitions M = 1 <—> M = -1 should make decoupling possible, since the M = 0 state exerts no z field at the S spin. A rough estimate of the condition can be made as follows. If the quadrupole coupling ω_Q is much larger than the I-S coupling (e.g. ω_Q ~ 100 KHz for deuterium) then for normal one-quantum decoupling we would require

$$\omega_1 \gg \omega_Q \quad , \tag{63}$$

a challenging technical demand under current NMR technology. This requirement is to be contrasted with the much less demanding condition

$$\omega_1 \gg d \tag{64}$$

for the S = 1/2 I = 1/2 pair with dipolar coupling d, as in (54).

If we excite the double-quantum transition, however, then according to second order perturbation theory (matrix element squared divided by energy difference) the transitions between M = 1 and M = -1 occur with an amplitude

$$\omega_1^{DQ} \sim \frac{\omega_1^2}{\omega_Q} \quad . \tag{65}$$

The effective double-quantum amplitude is to be compared with the coupling d; hence we now require

$$\frac{\omega_1^2}{\omega_Q} >> d \quad , \tag{66a}$$

$$\text{i.e.,} \qquad \omega_1 >> \sqrt{d\omega_Q} \quad , \tag{66b}$$

which is much more easily implemented than (63) for the usual case where d $<< \omega_Q$.

To appreciate the sensitivity of the double-quantum decoupling to resonance offset $\Delta\omega$ and rf amplitude ω_1 we adopt (61) and (62), substituting ω_1^2/ω_Q for ω_1 and $2\Delta\omega$ for $\Delta\omega$. For double-quantum decoupling, the S linewidth is given by

$$\delta_s \sim \cos\theta = \frac{2(\Delta\omega)\omega_Q}{(\omega_1^4 + 4\Delta\omega^2\omega_Q^2)^{1/2}} \quad , \tag{67}$$

thus making the resonance condition for decoupling much more sensitive than in one-quantum decoupling, since $\Delta\omega$ is multiplied by ω_Q.

At resonance

$$\delta_s \sim \frac{d^2\omega_Q^2}{\omega_1^4} \quad , \tag{68}$$

so decoupling begins only when $\omega_1 \sim (d\omega_Q)^{1/2}$. The subsequent dependence on ω_1 is much more rapid, going as the inverse fourth power. All this behavior has been quantitatively verified, and examples are shown in **Figure 29.** Double-quantum decoupling has been used in our laboratory to obtain high resolution spectra of diluted protons displaying, for example, proton chemical shift anisotropy for the hydrogen bonds in solid heavy ice, and to observe the effects of the tetrahedral motion of the protons on the NMR lineshapes as ice is heated towards its melting point. Typical proton spectra of 99% deuterated ice with deuterium double-quantum decoupling are shown in **Figure 30.** As the ice is heated the effects of motional narrowing are observed. A few degrees below the melting temperature the line is that of an isotropic sample. The intermediate spectra indicate that the protons are jumping between the tetrahedrally disposed hydrogen bonds around the oxygens.

24. Comment on the Relationship between Spin Decoupling and Multiple-Quantum Excitation

Consider a system of N I spins (e.g. protons) coupled to an S spin (e.g. carbon-13). Several schemes involving composite pulses and iterative sequences have been devised to effect spin decoupling in such systems. These sequences, employing phase shifts and permutations, are reminiscent of some of the selective n-quantum schemes described in section 17. There must be some relationship between the two areas. Indeed, suppose we could

engineer a pure (N+1)-quantum selective scheme to excite the I spins. Since N spins cannot absorb or emit more than N quanta, such an excitation would be tantamount to implementing the unit propagator, i.e. decoupling. In this sense decoupling schemes employing π pulses and π phase shifts are two-quantum selective (good for decoupling one spin) and multiple pulse schemes involving $\pi/2$ pulses and $\pi/2$ phase shifts are four-quantum (not pure) selective and decouple groups of spins. Details on these ideas will be published shortly.

25. **Two Level System in a Quantized Field**

I have often been asked where are the quanta, the photons, in a multiple quantum experiment? When we say $\Delta M = 2$, are two quanta really involved or just one off-resonance quantum at double the frequency? What's the relationship to optical multiphoton excitation? To investigate these questions clearly, I'd like to study the very simplest case where photons actually appear. In order to do so, it is necessary to bring in the radiation field as a legitimate full-fledged partner into the treatment, and not just treat it semiclassically as a time dependent perturbation on the spins. That way, we can "see" the photons in the field and count them. At the same time this treatment will remind us of Feynman's analogy of any two level system to a spin-1/2. Later we shall encounter generalizations of this analogy, e.g., a three-level system to a spin-1, and so on. The treatment, which was developed together with R. Harris, also reminds us of the analogies, often unhappily neglected, between NMR and optical spectroscopy.

Before we treat two-quantum phenomena, let us review the simplest one-

quantum problem, a two-level system interacting with a single mode of a cavity, described by a time independent Hamiltonian

$$H = H_{mat} + H_{rad} + H_{int} \quad . \tag{69}$$

H_{mat} is the matter Hamiltonian, the matter being the system (atom or spin) irradiated and behavior observed. We assume it consists of two states, 1 and 2, with energies $\hbar\omega_1$ and $\hbar\omega_2$, such that

$$\omega_2 - \omega_1 = \omega_0 \tag{70}$$

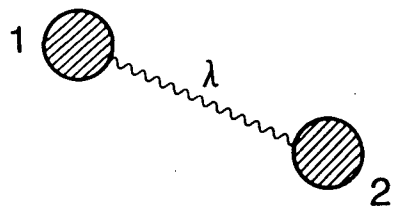

XBL-866-6324

Assume further that the particles occupying these states are fermions with coupling λ. Since at most one can occupy each state, the possible states are

$$|0,0\rangle,\ |0,1\rangle,\ |1,0\rangle,\ |1,1\rangle \quad , \tag{71}$$

where $|0,1\rangle$ is the vacuum for particle 1 and single occupancy for particle 2, etc. We now introduce Fermion operators c_1, $c_1^\dagger$, c_2, $c_2^\dagger$ such that

$$c_1^\dagger|0,k\rangle = |1,k\rangle \qquad k = 0,1$$

$$c_1|1,k\rangle = |0,k\rangle \qquad k = 0,1 \quad , \tag{72}$$

and similarly for c_2, $c_2^\dagger$ and $|j,0\rangle$, $|j,1\rangle$. All other operations yield zero. The Fermion operators satisfy the anticommutation rules

$$\{c_j,c_k\} = \{c_j^\dagger,c_k^\dagger\} = 0$$

$$\{c_j,c_k^\dagger\} = \delta_{jk} \qquad j,k = 1,2 \tag{73}$$

The matter Hamiltonian is given in terms of these operators by

$$H_{mat} = \hbar\omega_1 c_1^\dagger c_1 + \hbar\omega_2 c_2^\dagger c_2 \quad . \tag{74}$$

H_{rad} in (69) is the radiation Hamiltonian, which we write in terms of the photon creation and destruction operators for a single mode, a and $a^\dagger$, with frequency ω and eigenkets $|n\rangle$ (n = number of photons). We remember that for a harmonic oscillator, we have

$$\begin{aligned} a^\dagger|n\rangle &= \sqrt{n+1}\ |n+1\rangle \\ a|n+1\rangle &= \sqrt{n+1}|n\rangle \end{aligned} \quad . \tag{75}$$

The commutation rules are

$$[a,a] = [a^\dagger,a^\dagger] = 0$$

$$[a,a^\dagger] = 1 \tag{76}$$

and the Hamiltonian, ignoring the zero point energy, is

$$H_{rad} = \hbar\omega a^\dagger a \quad . \tag{77}$$

For H_{int} of (69), the interaction between the radiation and the matter, we assume the coupling depicted in **Figure 31.** A photon $\hbar\omega$ is absorbed, transforming particle 1 into 2, or one is emitted, transforming particle 2 into 1; i.e.,

$$H_{int} = \frac{\hbar\lambda}{2} (c_1 c_2^\dagger a + c_1^\dagger c_2 a^\dagger) \quad . \tag{78}$$

This coupling conserves energy for $\omega = \omega_0$ and incorporates the semiclassical rotating wave approximation (note that we have neglected events in which a photon is absorbed and transforms particle 2 into 1, for example). Equations (74), (77) and (78) now can be collected into the total Hamiltonian (69) as

$$H = \hbar\omega_1 c_1^\dagger c_1 + \hbar\omega_2 c_2^\dagger c_2 + \hbar\omega a^\dagger a + \frac{\hbar\lambda}{2} (c_1 c_2^\dagger a + c_1^\dagger c_2 a^\dagger) \quad . \tag{79}$$

26. **Fictitious Spin-1/2 Operators**

At this point we introduce the fictitious spin-1/2 operators

$$\begin{aligned} I_x &= \frac{1}{2}(c_1 c_2^\dagger + c_1^\dagger c_2) \\ I_y &= \frac{-i}{2} (c_1 c_2^\dagger - c_1^\dagger c_2) \\ I_z &= \frac{1}{2} (c_1^\dagger c_1 - c_2^\dagger c_2) \quad . \end{aligned} \tag{80}$$

Given the relationships (72) and (73), it can be verified that

$$[I_x, I_y] = iI_z \quad , \qquad \text{and cyclic permutations} \quad . \tag{81}$$

With the eigenstates $|\pm\rangle$ of I_z defined as

$$I_z|\pm\rangle = \pm\frac{1}{2}|\pm\rangle \tag{82}$$

and

$$I_\pm = I_x \pm iI_y \quad , \tag{83}$$

the Hamiltonian (79) can be written, aside from a commuting operator (remember that the number of particles is conserved), as

$$H = -\hbar\omega_0 I_z + \hbar\omega a^\dagger a + \frac{\hbar\lambda}{2}(a^\dagger I_- + aI_+) \quad . \tag{84}$$

This Hamiltonian is identical to that of a spin-1/2 interacting with the cavity mode. Now assume the cavity mode is at resonance ($\omega = \omega_0$), and transform to a picture defined by

$$R(t) = \exp(-it(-\omega_0 I_z + \omega a^\dagger a)) \quad , \tag{85}$$

the analog of the rotating frame in the full quantum problem. The Hamiltonian in this picture is given by

$$H = \frac{\hbar\lambda}{2}(a^\dagger I_- + aI_+) \quad . \tag{86}$$

27. Evolution of the Two Level System

Imagine the initial state $|\psi(0)\rangle$ being the excited state $|-\rangle$ for the fictitious spin with n photons in the cavity, as depicted in **Figure 32**:

$$|\psi(0)\rangle = |-,n\rangle \quad . \tag{87}$$

The evolution of $|\psi\rangle$ is given by

$$|\psi(t)\rangle = \exp(-itH/\hbar)\psi(0) \tag{88}$$

which is easily evaluated using the Hamiltonian of (86) together with (75)

and (83) to yield

$$|\psi(t)\rangle = |-,n\rangle\cos\sqrt{n+1}\,\frac{\lambda t}{2} - |+,n+1\rangle i\sin\sqrt{n+1}\,\frac{\lambda t}{2} \quad . \tag{89}$$

This expression describes a quantum Rabi oscillation or nutation that periodically exchanges a photon between the cavity and the spin. The analogy to the usual semiclassical problem of a spin I = 1/2 interacting with a resonance field of amplitude ω_1 is made by realizing that

$$-\lambda\sqrt{n+1} \quad \longleftrightarrow \quad \omega_1 \quad . \tag{90}$$

Note, however, that even when there are initially no photons to begin with in the cavity (n = 0), there is still evolution, corresponding to spontaneous emission from the excited spin or two level system. Note also that for a 2π pulse,

$$\omega_1 t = \sqrt{n+1}\,\lambda t = 2\pi \quad , \tag{91}$$

the ket $|\psi(0)\rangle$ does not come back to itself but instead to $\cos\pi$ times itself, i.e.,

$$|\psi(2\pi)\rangle = -|\psi(0)\rangle \quad . \tag{92}$$

This effect corresponds to the well known spinor behavior of a system with an even number of states or of a nonintegral fictitious spin.

28. **Evolution Off Resonance**

The expression (89), derived for resonance ($\omega = \omega_0$), can be generalized for arbitrary frequency of the mode ω in (84). This extension is best made by a transformation to a tilted picture in analogy to (58). The result, for the same initial condition (87), is

$$|\psi(t)\rangle = |-,n\rangle[\cos\lambda_e t/2 - i\cos\theta\sin\lambda_e t/2] - |+,n+1\rangle i\sin\theta\sin\lambda_e t/2 \quad , \tag{93}$$

where

$$\lambda_e = (\lambda^2(n+1) + (\omega_0 - \omega)^2)^{1/2} \tag{94}$$

$$\cos\theta = \sqrt{n+1}\ \lambda/\lambda_e \quad . \tag{95}$$

29. **Adiabatic Rapid Passage**

The treatment above provides an elegant picture of adiabatic rapid passage for a two-level system or fictitious spin-1/2. Consider **Figure 33,** which depicts the energy levels of the uncoupled matter and radiation Hamiltonians

$$H_0 = H_{mat} + H_{rad} \tag{96}$$

as the frequency (or field) is varied through resonance. The resonance between matter and radiation occurs at the level crossings, $\omega = \omega_0$. Adding the interaction Hamiltonian H_{int} causes a mixing of the states near resonance, which gives rise to an avoided crossing as in **Figure 34.** The repulsion between levels at resonance depends on the number of photons in the cavity as $(n+1)^{1/2}\lambda$, the semiclassical field intensity ω_1 from (90).

If we begin with the spin (or fictitious spin) in one state away from resonance, e.g. $|-,n\rangle$ on the left of Figure 34, and now shift the frequency <u>adiabatically</u> through resonance, then we recall from quantum mechanics that the system remains in an eigenstate. Thus it will go to $|+,n-1\rangle$ on the right hand side. Therefore sweeping through a resonance line rapidly

compared to T_1 but slowly enough so there are no frequency components at ω_0 should invert a resonance line whether we sweep from left to right or right to left. This effect is called population inversion by adiabatic rapid passage, an extremely useful way of making selective robust π pulses. The most efficient adiabatic sweeps are not linear (i.e., linear dependence of frequency on time), however, but rather are hyperbolic functions as shown by Baum and Tycko.

30. Three Level System in a Quantized Field

We adopt the notation of section 25 for three particles

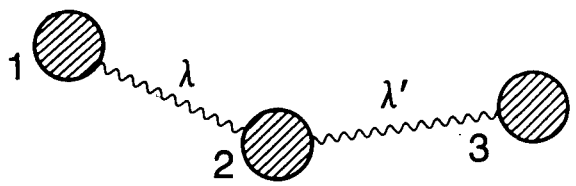

XBL-866-6325

interacting with the single mode of a cavity; we assume that only 1 and 2 or 2 and 3 can be directly interconnected by energy conserving (rotating wave) absorption or emission of a single photon. Thus the interaction is depicted in **Figure 35a**, with

$$\omega_{12} + \omega_{23} = 2\omega_0$$
$$\omega_{12} - \omega_{23} = 2\omega_Q \qquad (97)$$

The full Hamiltonian for this system,

$$H = \hbar\omega_1 c_1^\dagger c_1 + \hbar\omega_2 c_2^\dagger c_2 + \hbar\omega_3 c_3^\dagger c_3 + \hbar\omega a^\dagger a + \hbar\lambda(c_1 c_2^\dagger a + c_1^\dagger c_2 a^\dagger) + \hbar\lambda'(c_2 c_3^\dagger a + c_2^\dagger c_3 a^\dagger) \tag{98}$$

is entirely analagous to (79). I will not discuss the general case here, but will instead select simple conditions under which the double quantum behavior will emerge.

31. **Fictitious Spin-1 Operators**

First let us introduce the fictitious spin-1 operators

$$\begin{aligned} I_z &= c_1^\dagger c_1 - c_3^\dagger c_3 \\ I_+ &= c_1 c_2^\dagger + c_2 c_3^\dagger \\ I_- &= c_1^\dagger c_2 + c_2^\dagger c_3 \\ Q_z &= 2c_2^\dagger c_2 - c_3^\dagger c_3 - c_1^\dagger c_1 \\ Q_+ &= c_2 c_3^\dagger - c_1 c_2^\dagger \qquad Q_- = c_2^\dagger c_3 - c_1^\dagger c_2 \\ Q_{+2} &= c_1 c_3^\dagger \qquad Q_{-2} = c_1^\dagger c_3 \end{aligned} \tag{99}$$

Here the raising and lowering operators are used directly without going through any intermediate stages involving I_x, Q_x, Q_{xy}, etc. Inserting these

spin-1 operators in (98) and ignoring commuting unit operators (again, number of particles is conserved) we can rewrite H as

$$H = -\hbar\omega_0 I_z + \frac{\hbar\omega_Q}{3} Q_z + \hbar\omega a^\dagger a + \frac{\hbar}{2}[(\lambda - \lambda')Q_+ + (\lambda + \lambda')I_+]a + \frac{\hbar}{2}[(\lambda - \lambda')Q_- + (\lambda + \lambda')I_-]a^\dagger \quad . \tag{100}$$

We now specialize to the case where the two allowed one-quantum absorptions and emissions have the same matrix elements,

$$\lambda = \lambda' \quad , \tag{101}$$

finding that

$$H = -\hbar\omega_0 I_z + \frac{\hbar\omega_Q}{3} Q_z + \hbar\omega a^\dagger a + \hbar\lambda(I_+ a + I_- a^\dagger) \quad . \tag{102}$$

This Hamiltonian is just the interaction of a quadrupolar spin-1 with Zeeman frequency ω_0 and quadrupolar frequency ω_Q. Now assume the radiation is at resonance ($\omega = \omega_0$) and that it is weak compared to the quadrupolar splitting,

$$\lambda\sqrt{n+1} \ll \omega_Q \quad , \tag{103}$$

corresponding to the situation in **Figure 35b.** This condition embodies the weaker case where

$$\lambda \ll \omega_Q \quad . \tag{104}$$

32. Double-Quantum (Two-Photon) Hamiltonian

In the interaction picture defined by (85), the Hamiltonian (102) can be written

$$H = H_Q + H_1 = \frac{\hbar\omega_Q}{3} Q_z + \hbar\lambda(I_+ a + I_- a^\dagger) \quad . \qquad (105)$$

With condition (104) we now have a situation ideal for perturbation theory since the second operator term H_1 in (105) is much smaller than the first term H_Q. It is appropriate to retain only the "secular" part of the interaction term, i.e. that part diagonal with respect to the first term. We carry this out as follows. First, define an infinitesimal transformation

$$H' = e^{-iS} H e^{iS} \cong H - i[S,H] + \ldots \quad , \qquad (106)$$

where S is an infinitesimal Hermitian operator analogous to Vega's semiclassical tilt operator. Putting (106) into (105), we get

$$H' = H_Q + H_1 - i[S,H_Q] - i[S,H_1] + \ldots \quad . \qquad (107)$$

Now we demand that the first order infinitesimal term vanish, so that

$$H_1 - i[S,H_Q] = 0 \quad , \qquad (108)$$

which reduces (107) to

$$H' \cong H_Q + H_1' \qquad (109)$$

with the modified interaction Hamiltonian

$$H_1' = -i[S,H_1] \quad . \tag{110}$$

After some algebra the S which satisfies (108) is found to be

$$S = -i \frac{\lambda}{\omega_Q} (Q_+ a + Q_- a^\dagger) \quad . \tag{111}$$

Evaluating the commutator in (110) with (111), we have finally for the effective interaction Hamiltonian

$$H_1' = \frac{\hbar\lambda^2}{\omega_Q} (Q_{+2} a^2 + Q_{-2} a^{\dagger 2}) \quad . \tag{112}$$

According to the definitions of $Q_{\pm 2}$ and a, $a^\dagger$ given in (75) and (99), this form is a pure double-quantum Hamiltonian with the pleasant property of showing the two photons directly in the terms a^2 and $a^{\dagger 2}$. These terms represent the destruction and creation of only pairs of photons.

33. **Evolution of the System**

If the system begins in the upper state as shown in **Figure 36** with n photons in the cavity, i.e.,

$$|\psi(0)\rangle = |-,n\rangle \quad , \tag{113}$$

then under the influence of the Hamiltonian (112) the system evolves as

$$\begin{aligned} |\psi(t)\rangle = |-,n\rangle \cos\sqrt{(n+1)(n+2)}\ \frac{\lambda' t}{2} \\ - |+,n+2\rangle i \sin\sqrt{(n+1)(n+2)}\ \frac{\lambda' t}{2} \quad , \end{aligned} \tag{114}$$

where λ' is the effective two-photon amplitude

$$\lambda' = \frac{\lambda^2}{\omega_Q} \quad . \tag{115}$$

This result is to be compared with (89). Here two photons are being exchanged with the cavity; hence the process is a two-photon Rabi oscillation.

The correspondence to the semiclassical case is given by

$$\frac{\lambda^2}{\omega_Q}\sqrt{(n+1)(n+2)} \sim \frac{\lambda^2 n}{\omega_Q} \longleftrightarrow \frac{\omega_1^2}{\omega_Q} \quad . \tag{116}$$

When we begin with no photons in the cavity, (114) corresponds to two-photon spontaneous emission. This process, incidentally, is how metastable He(1s, 2s) decays to the ground state.

34. **Double-Quantum Adiabatic Rapid Passage**

The energy levels of the three-level system and cavity photons with no coupling between them appear in **Figure 37**. There are now three relevant crossings indicated in the circle, two corresponding to normal one-quantum resonances and the one we have just described due to a double-quantum resonance at ω_0. With the interaction between matter and radiation, all three crossings are avoided, as shown for the case $\lambda^2((n+1)(n+2))^{1/2} \ll \omega_Q^2$ in **Figure 38** - roughly $\lambda(n+1)^{1/2} \ll \omega_Q$ as stated in (103). The levels at the two one-quantum resonances repel by $\sim \lambda(n+1)^{1/2}$ whereas those at the double-quantum resonance experience the weaker repulsion $\sim\lambda^2((n+1)(n+2))^{1/2}/\omega_Q$. Thus the adiabatic condition for the double-quantum

resonance is considerably more stringent than that for the one-quantum resonances.

Several interesting features are exposed in the diagram of Figure 38. The resonances of a three level system can be inverted by adiabatically sweeping through either all the transitions or only through the double-quantum transition. Individual one-quantum transitions may be inverted by selectively sweeping through them adiabatically. If we sweep adiabatically to the right through the left resonance and then through the double-quantum resonance, the left line is inverted; if we sweep to the left first through the double-quantum resonance and then through the left one-quantum resonance, the left line does not invert. The intensities of each are also affected. This phenomenon was first observed in experiments on spin-1 nuclei in crystals, where lines would sometimes invert with adiabatic rapid passage in one direction but not in the other. It is of course possible to sweep so that passage through the one-quantum transitions is adiabatic, whereas passage through the double-quantum transition is not. If passage through the double-quantum transition is sudden enough compared with the level repulsion, then the system behaves as if the levels cross at ω_0 and there is no double-quantum inversion. Generalizations of these considerations to higher spin and to coupled spins is straightforward.

I mention in closing that all these arguments concerning adiabatic rapid passage can of course be made using traditional semiclassical NMR considerations.

35. Spin Temperature and Cross Polarization

I was asked to say some words about sensitivity enhancement by cross-

polarization, in particular to provide a simple statistical picture. Let me first review the thermodynamic picture of cross-polarization, using the spin temperature concepts introduced in the lectures by Goldman.

Consider the prototypical situation in **Figure 39,** which shows a system of N_S S spins with magnetogyric ratio γ_S in thermal spin contact with a system of N_I I spins with magnetogyric ratio γ_I. The S spins experience an effective magnetic field B_S (perhaps in their rotating frame) and the I spins experience an effective magnetic field B_I (perhaps in their rotating frame). We begin with the S spins unpolarized and the I spins polarized. The initial I spin magnetization in the high temperature approximation is given by Curie's Law as

$$M_I^{(i)} = \beta_I^{(i)} C_I B_I \quad , \tag{117}$$

where

$$\beta = \frac{1}{kT} \tag{118}$$

is the inverse spin temperature and

$$C_I = \frac{1}{3} \gamma_I^2 \, hI(I+1)N_I \tag{119}$$

is the I spin heat capacity. The energy and entropy are given by

$$E_I^{(i)} = - \beta_I^{(i)} C_I B_I^2 \tag{120}$$

and

$$S_I^{(i)} = \text{Const} - k\beta_I^{(i)2} C_I B_I^2 \quad . \tag{121}$$

In the above expressions, the superscript (i), for "initial", indicates the condition before cross-polarization to S.

We now wait a time greater than T_{IS} for cross-polarization (by cross-relaxation) between the I and S systems to bring them to thermal

equilibrium, i.e., to equal spin temperatures. Call this temperature $\beta^{(f)}$,

$$\beta^{(f)} = \beta_I^{(f)} = \beta_S^{(f)} \quad , \tag{122}$$

where superscript (f), for "final", indicates the condition after cross-polarization. The energy is now given by

$$E^{(f)} = E_I^{(f)} + E_S^{(f)} = -\beta^{(f)}[C_I B_I^{\,2} + C_S B_S^{\,2}] \quad . \tag{123}$$

Now we define a ratio of spin heat capacities

$$\varepsilon^2 = C_S/C_I \tag{124}$$

and a ratio of effective magnetic fields on S and I

$$\alpha = B_S/B_I \quad , \tag{125}$$

and realize that the cross-polarization takes place at constant energy since there are no time dependent fields. We then can equate (120) with (123) to obtain

$$\beta^{(f)} = \beta_I^{(i)}\left(\frac{1}{1 + \alpha^2\varepsilon^2}\right) \tag{126}$$

and an S magnetization (recall (117))

$$M_S^{(f)} = \left(\frac{\alpha}{1 + \alpha^2\varepsilon^2}\right)\beta_I^{(i)} C_S B_I \quad . \tag{127}$$

This quantity is $\alpha/(1+\alpha^2\varepsilon^2)$ times $M_S^{(0)}$, where $M_S^{(0)}$ is the normal value of M_S at thermal equilibrium in the laboratory (i.e. when $B_I = B_S$ and $\beta_I^{(i)} = \beta_S^{(i)}$)

$$M_S^{(f)} = \left(\frac{\alpha}{1 + \alpha^2\varepsilon^2} \right) M_S^{(0)} \quad . \tag{128}$$

36. Hartmann-Hahn Matching

So far we have said nothing about the time scale T_{IS} for cross-polarization. Equation (128) describes an enhancement of the S signal when I-S equilibrium is reached, but T_{IS} depends strongly on B_I and B_S and therefore on α in (125).

The most rapid cross-polarization occurs under the Hartmann-Hahn condition

$$\gamma_I B_I = \gamma_S B_S \tag{129}$$

for B_I and B_S in the I and S rotating frames, respectively. Under these circumstances the mutual flip-flop of a single S spin and a single I spin conserves energy in the double rotating frame, as depicted in **Figure 40.** If the S spins are rare compared to I, i.e.

$$\varepsilon << 1 \quad , \tag{130}$$

then, to a good approximation, equation (128) becomes

$$M_S^{(f)} = \frac{\gamma_I}{\gamma_S} M_S^{(0)} \quad . \tag{131}$$

The ratio γ_I/γ_S gives the Hartmann-Hahn enhancement, which is ~4 for protons and carbon-13.

37. Other Matching Conditions

It is possible to cross-polarize using conditions other than Hartmann-Hahn matching, under which the enhancement is larger than (131) but the time required is longer. For example, if $\alpha = 2$ in (125), so that

$$2\gamma_I B_I = \gamma_S B_S \quad , \tag{132}$$

then a mutual flip-flop of 2 I spins and one S spin conserves energy, as shown in **Figure 41.** The value of α which yields the maximum polarization from (127) is

$$\alpha = \frac{1}{\varepsilon} = (C_I/C_S)^{1/2} \quad , \tag{133}$$

in which case we obtain, from (128),

$$M_S^{(f)} = \frac{1}{2} \frac{\gamma_I}{\gamma_S} \left(\frac{N_I}{N_S}\right)^{1/2} M_S^{(0)} \quad . \tag{134}$$

This value is one half of the maximum possible S magnetization

$$M_S^{(max)} = \frac{\gamma_I}{\gamma_S} \left(\frac{N_I}{N_S}\right)^{1/2} M_S^{(0)} \tag{135}$$

attainable by isentropic transfer of all thermal equilibrium I magnetization to S, as we shall see in the next section.

This maximum can be realized by demagnetizing the I spins in their rotating frame at constant entropy and then remagnetizing the S spins in their rotating frame at constant entropy. There are a variety of alternative ways to effect cross-polarization, including dynamic nuclear polarization, thermal mixing in the laboratory frame, and coherent transfer by heteronuclear multiple-quantum coherence.

38. **Statistical (Microscopic) Picture**

Take a system of N_I I spins with N_I^+ "up" and N_I^- "down" coupled to N_S S spins with N_S^+ "up" and N_S^- "down". The I and S polarizations are defined by

$$P_I = N_I^+ - N_I^-$$
$$P_S = N_S^+ - N_S^- \quad . \tag{136}$$

We begin with I polarized to $P_I^{(i)}$ and S unpolarized ($P_S^{(i)} = 0$) and now ask the question: What is the S polarization achievable by the most efficient possible cross-polarization process from I to S?

Obviously the most efficient process is a reversible one, under which the entropy remains constant. The entropy depends on W, the number of microscopic configurations, as

$$S = k \ln W \quad . \tag{137}$$

Let us calculate W as a function of the polarization P for N spins of which N^+ are "up" and N^- are "down". W corresponds to the number of ways to place N^+ indistinguishable objects in N positions

$$W = \binom{N}{N^+} = \frac{N!}{N^+!\, N^-!} \tag{138}$$

For large N, N^+, N^- this expression can be approximated as

$$W \sim 2^N e^{-P^2/2N} \quad , \tag{139}$$

so, from (137), the entropy is given by

$$S \sim \text{Const} - \frac{P^2}{2N} \quad . \tag{140}$$

If the entropy remains constant and all the I polarization is transferred to S, then (140) yields

$$\frac{(P_I^{(i)})^2}{2N_I} = \frac{(P_S^{(f)})^2}{2N_S} \quad , \tag{141}$$

where I remind you again that the superscript (i) indicates "initial" (before the cross-polarization) and (f) indicates "final" (after the cross-polarization). The maximum final S polarization is

$$P_S^{(max)} = P_S^{(f)} = \left(\frac{N_S}{N_I}\right)^{1/2} P_S^{(0)} \quad . \tag{142}$$

<u>If $N_S < N_I$ the polarization decreases in going from I to S and if $N_S > N_I$ it increases</u>. Now we recall that the thermal equilibrium polarization is proportional both to γ (Boltzmann factor) and to N so that

$$P_I^{(i)} = \frac{\gamma_I N_I}{\gamma_S N_S} P_S^{(0)} \tag{143}$$

where $P_S^{(0)}$ is the normal thermal equilibrium value of the S polarization, corresponding to the same temperature as $P_I^{(i)}$. Inserting (143) into (142) gives

$$P_S^{(max)} = \frac{\gamma_I}{\gamma_S} \left(\frac{N_I}{N_S}\right)^{1/2} P_S^{(0)} \quad , \tag{144}$$

or for the magnetization,

$$M_S^{(max)} = \frac{\gamma_I}{\gamma_S} \left(\frac{N_I}{N_S}\right)^{1/2} M_S^{(0)} \quad , \tag{145}$$

in agreement with (135). The maximum enhancement factor $(\gamma_I/\gamma_S)(N_I/N_S)^{1/2}$

is roughly 50 for $I \equiv {}^{1}H$, $S \equiv {}^{13}C$, $(\gamma_I/\gamma_S \sim 4, (N_I/N_S)^{1/2} \sim 12)$.

39. Coherent Averaging Theory

A recurring theme throughout these lectures is the requirement for the preparation or evolution of a system under a specified Hamiltonian or under a Hamiltonian with particular symmetry or transformation properties. For example, in decoupling we attempt to make the effective coupling Hamiltonian zero. In multiple-quantum spectroscopy of solids we required a time reversed detection with $H \sim H_{xx} \sim H_{yy}$. It is clearly necessary on many occasions to implement a specific desired Hamiltonian, perhaps different from the natural unperturbed Hamiltonian of the system. In other words, whereas the system might naturally evolve under its propagator $\mathbf{L}(t)$,

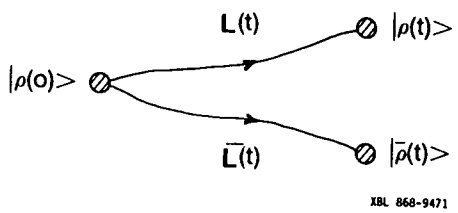

(146)

we apply a perturbation so that the system evolves under a different propagator $\bar{\mathbf{L}}(t)$, due to a Hamiltonian $\bar{H}$, arriving perhaps at a different state at time t. The perturbation needed may be a sequence of pulses, a mechanical rotation, or perhaps an incoherent perturbation such as heating the sample to induce chemical exchange or Brownian rotation.

The theory that best acounts for the design of specific Hamiltonians (and therefore propagators) under coherent perturbation is Coherent Averaging Theory. Suppose the Hamiltonian is time dependent (owing to, for example, an applied perturbation), as depicted in **Figure 42.** A question which arises is: can we find a time independent Hamiltonian $\bar{H}$ which can

induce evolution of the system through $\bar{L}(t)$ to the same state as H(t) would induce at time t? The answer is yes - that $\bar{H}$ is the Magnus Hamiltonian, given by

$$\bar{H} = \bar{H}^{(0)} + \bar{H}^{(1)} + \bar{H}^{(2)} + \ldots \quad , \tag{147}$$

where

$$\bar{H}^{(0)} = \frac{1}{t} \int_0^t H(t')dt' \tag{148}$$

is the average Hamiltonian. The next two terms in this series are

$$\bar{H}^{(1)} = \frac{-i}{2t} \int_0^t \int_0^{t'} [H(t'),H(t'')]dt''dt' \quad , \tag{149}$$

and

$$\bar{H}^{(2)} = -\frac{1}{6t} \int_0^t \int_0^{t'} \int_0^{t''} \{[H(t'),[H(t''),H(t''')]] + [H(t'''),[H(t''),H(t')]]\}dt'''dt''dt' \tag{150}$$

If (147) converges rapidly, so that $\bar{H}^{(k)}$ are small for $k \neq 0$, then the average Hamiltonian $H^{(0)}$ provides a good description of the system and the other $\bar{H}^{(k)}$ are correction terms. By applying a perturbation we have therefore taken a system which would have evolved under some Hamiltonian H and caused it to evolve effectively under $\bar{H}^{(0)}$ as in (146). The trick is to implement the desired $\bar{H}^{(0)}$ by appropriate perturbations that can be realized experimentally, such as spin decoupling and time reversal. Note that, in general, $\bar{H}$ and $\bar{H}^{(0)}$ depend on t, but if H(t) is periodic then the same $\bar{H}$ and $\bar{H}^{(0)}$ hold at all integer multiples of t_c. If H(t) is not periodic, the

approach is still useful, since one can implement an $\bar{H}$ which produces a particular desired final state $|\bar{\rho}(t)\rangle$ at time t.

Expressions (148) to (150) were used to calculate the terms for spin decoupling in (58) to (60) and the time reversal Hamiltonian of Figure 24. They can also be used to derive the double-quantum terms of (65) and (112). This approach has been useful in a variety of problems in different areas, some of which are listed below:

Truncation of couplings by high field

Spin Locking

Magic angle spinning, hopping, second order broadening

Spin decoupling

Multiple pulse line narrowing in solids

Composite pulses

Scalar recoupling (SHRIMP, etc.)

Bloch-Siegert shift

Soft pulses and double-quantum excitation

Cross-polarization

Time reversal, spin and photon echoes

Selective multiple-quantum excitation

Iterative schemes (MLEV, etc.)

Optically detected electron spin coherence

Self-decoupling and deceptively simple spectra

Spin temperature in the toggling frame

Imaging of solids by linear nutation sequences

Geometrical phase in adiabatic quantum processes

Born-Oppenheimer Approximation

A particularly useful simplification occurs when the time dependent Hamiltonian H(t) commutes with itself at all times, i.e. $[H(t),H(t')] = 0$. In this case all $\bar{H}^{(k)} = 0$ for $k \neq 0$, as we can see from (149) and (150) for $k = 1,2$, and the average Hamiltonian $\bar{H}^{(0)}$ is exact. This happens for Carr-Purcell trains and for magic angle spinning involving chemical shift interactions, dipolar couplings of N spins in a one-dimensional array (e.g. a pair of spins), heteronuclear dipolar couplings, or first order quadrupolar coupling of isolated spins. In this way it is possible to narrow the spectrum by magic angle spinning, even for the broad quadrupolar spectra of deuterium in solids. An example showing the resolution of isotropic deuterium chemical shifts in solids appears in **Figure 43.** More detailed discussions of magic angle spinning and its many applications in solids are presented in the lectures by Griffin.

40. Zero Field NMR

One of the motivations for doing multiple-quantum NMR described in my early lectures was to simplify complex spectra. There the complexity of the spectra arose from homogeneous effects, such as the large number of dipolar couplings. But spectra may be intractably complex and broad owing to inhomogeneous broadening as well, which arises from orientational distributions that produce superpositions of inherently simple spectra. This broadening occurs in disordered systems such as polycrystalline solids, amorphous materials, or partially ordered polymers or biological compounds. Because of the anisotropy of the dipolar and quadrupolar interactions,

molecules or small groups of spins exhibit different spectra for different orientations; the complete spectrum therefore reflects subspectra from all the different orientations, superposed to form a broad, often featureless "powder pattern" from which little information can be obtained.

An example of the proton NMR spectrum of a polycrystalline organic solid, containing four hydrogens per molecule,

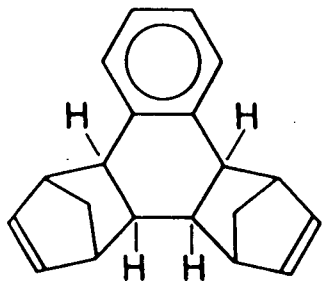

XBL 868-9470

is shown in **Figure 44**. The situation is similar to that encountered in crystallography by x-ray or neutron diffraction. Although oriented crystals provide diffraction patterns from which structural information can be extracted, a polycrystalline sample yields a considerably less useful powder pattern. The solution to this problem is to perform the NMR in zero field, using principles well known in other forms of magnetic resonance, for example Nuclear Quadrupole Resonance (NQR) or Optically Detected Electron Paramagnetic Resonance (EPR). In the absence of a magnetic field defining an axis in space, all orientations are equivalent and orientationally disordered materials should provide sharp "crystal-like" spectra. The only problem is to overcome the low sensitivity inherent in the low frequencies of zero field NMR. To take advantage of the high resolution of zero field and the high sensitivity of high field, we employ adaptations of well-known

field cycling methods.

A diagram of the simplest field cycle and the corresponding apparatus needed is given in **Figure 45.** Removal of the sample to an intermediate field, followed by a sudden transition to zero field, causes the magnetization carried from the high field to oscillate at frequencies characteristic of the local magnetic dipolar or electric quadrupolar interactions. Reapplication of the high field permits sensitive detection as a function of the time spent in zero field. Fourier transformation of this time domain signal will produce a zero field frequency domain spectrum with high resolution and full high field sensitivity. As an example, the zero field NMR spectrum of a polycrystalline sample of the four-proton spin system of Figure 44 is shown in **Figure 46.** The relative positions of the hydrogens and the conformation of the central cyclohexane ring can be determined from such a spectrum.

41. Zero Field NQR of Deuterium

Frequency domain methods have long been used to observe quadrupolar nuclei ($I \geq 1$), where direct detection of the quadrupolar resonance is possible at high frequency. These methods are of limited applicability, however, when the frequencies are low (< 100 kHz), as for example with deuterium. Moreover, direct detection requires the use of radiofrequency irradiation in zero field. Clearly, Fourier transform experiments of the type described in the previous section can avoid many of these problems. As an example, the high field 55.6 MHz deuterium NMR spectrum of perdeuterated polycrystalline diethylterephthalate is shown in **Figure 47a.** Only the most prominent singularities of the methyl, methylene and aromatic lineshapes can

be resolved, since the deuterium signal is distributed over a wide bandwidth (although in favorable cases it can be "dePaked" as explained in the lectures by Bloom). In contrast, the zero field deuterium spectrum in **Figure 47b** displays four distinct groups of peaks with sharply resolved fine structure. From such a spectrum resonances from different sites in the molecule can be assigned. In this case, five inequivalent sites are established: methyl, two inequivalent methylenes and two inequivalent aromatics. The high resolution of the zero field experiment permits the measurement of very similar quadrupolar coupling constants and small asymmetry parameters. **Figure 48** shows a further example with perdeuterated solid dimethoxybenzene. The two doublets around 135 kHz arise from the inequivalence of deuteron sites in the aromatic ring created by the frozen solid state conformation of the molecule. Many nuclei with low quadrupolar frequencies are directly accessible by such zero field NQR studies, and among those studied in our laboratory, in addition to deuterium, are lithium-7, nitrogen-14, and aluminum-27.

42. **Two-Dimensional Zero Field NMR**

Connections between zero field NMR and NQR transitions (which relate to connections between molecular sites) can be determined by extending the experiment to incorporate two time periods in zero field. The basic idea is to obtain the signal as a function of two independent time variables, t_1 and t_2, and then to Fourier transform against both to obtain a two-dimensional zero field frequency spectrum. An illustration of this experiment is provided in **Figure 49a**, where the field cycle shown employs a pulsed field mixing period between t_1 and t_2. Magnetization able to oscillate at two

possible frequencies in the two time periods, for example the ν_+ and ν_- quadrupolar frequencies of a given site, will produce an off-diagonal peak, or "cross-peak", at the intersection of these two frequencies if the mixing sequence transfers coherence between the transitions. An experimental illustration of the connectivities in a spin I = 1 system appears in **Figure 49b**, which shows the two-dimensional zero field spectrum of the methylene region of a sample of selectively deuterated diethylterephthalate. This result shows that among the four lines in the CD_2 region of the spectrum, lines 1 and 3 belong to one deuteron and lines 2 and 4 to the other inequivalent deuteron. With this kind of experiment one can hope to identify sites by their quadrupole couplings and then determine intersite distances through their dipolar couplings in a two-dimensional spectrum.

A different class of two-dimensional experiments reserves zero field evolution for the period t_1 and high field evolution for the period t_2 in order to correlate high field and zero field NMR transitions. An example, shown in **Figure 50** for two water protons in a polycrystalline hydrate, displays the Pake doublet powder pattern in the high field dimension and a three line zero field spectrum in the other dimension . In principle, one can contemplate obtaining high resolution chemical shifts in the high field dimension and sharp dipolar couplings between sites in the zero field dimension.

43. Zero Field Pulses

The discussion so far has focussed on the sudden removal of an applied field to induce zero field evolution as in Figure 45. This approach, however, suffers from two principal disadvantages. The first derives from

the requirement that the intermediate field be larger than the local spin interactions so that the Zeeman interaction dominates. For nuclei with small magnetogyric ratios and large quadrupolar coupling constants, this condition requires that a field of a few hundred to a few thousand Gauss be applied for some tens of milliseconds - perhaps a difficult experimental task. The other disadvantage comes from the lack of selectivity in the sudden transition that excites evolution of different isotopes and spins (e.g. protons, deuterium, carbon-13) in zero field. The experiment can be made selective and more flexible, however, by a simple modification of the field cycle to use pulsed dc magnetic fields to excite different nuclear spins in zero field, as illustrated in **Figure 51.** The sample is first removed completely to zero field through adiabatic demagnetization in the laboratory frame. Application of a pulsed dc field at this point then changes the state of the system and induces evolution in zero field for a time t_1. This evolution may be terminated with a second dc pulse. The effect is analogous to pulsed NMR in high field, but here the resonant frequency, and therefore the frequency of the pulses, is zero. Finally, the sample is adiabatically remagnetized back to high field for normal high field NMR detection. Different isotopes and spins can be addressed separately by making the zero field pulses selective, perhaps by using composite pulses that produce 2π rotations for all isotopes except the one of interest.

An additional advantage of pulsed field cycles of the sort shown in Figure 50 is that they permit level crossings between protons and quadrupolar spins during the adiabatic demagnetization and remagnetization. This possibility allows the zero field evolution of a quadrupolar spin, say

deuterium, to be detected by the effect on the more sensitive proton spins. Indirect detection has long been used in traditional field cycling NQR experiments, but in the usual procedure the protons are made to absorb low frequency zero field irradiation directly, by which is produced a low frequency signal that obscures the NQR lines. The time domain experiment alleviates such problems by using selective dc pulsed fields. An example of a nitrogen-14 zero field spectrum obtained by selective pulses in zero field and indirect detection through the protons is shown for polycrystalline ammonium sulfate in **Figure 52.** Such experiments on deuterium and nitrogen-14 are likely to be useful in the study of biological systems, which are often inherently amorphous or disordered.

44. Calculation of the Zero Field Spectrum

It is instructive to perform a specific calculation of the zero field signal for a simple case. Consider a molecule or group of spins in a polycrystalline or otherwise disordered sample. The laboratory based coordinate system is denoted x,y,z as usual, with any high field B_o along z, and molecular based axes are labeled xm, ym, zm. We denote by $R(\Omega)$ the operator, or by $\mathbf{R}(\Omega)$ the superoperator, that effects the transformation between laboratory and molecular frames. The transformation angles Ω are characterized by a probability distribution $P(\Omega)$ over the sample. $\Omega \equiv(\alpha,\beta)$ where α,β are the two Euler angles - the third γ is not required, and accordingly is set to zero, owing to cylindrical symmetry about z in high field.

In the molecular frame the internal Hamiltonian (dipolar, quadrupolar, etc.) is homogeneous in the sense that it is independent of Ω or position in

the sample. For the simple field cycle of Figure 45 the initial state of the spin system is given by

$$|\rho(0)\rangle \sim |I_z\rangle \quad , \tag{151}$$

and I_z is detected in high field at the end of the cycle. Thus we can use precisely the formalism of section 8. The zero field time domain signal (again we write t instead of t_1) is given by

$$F_\Omega(t) = \langle I_z \, |\mathbf{L}_\Omega(t)| \, I_z\rangle \quad . \tag{152}$$

The subscript Ω reminds us that this signal is for a particular orientation of the molecule or spin system in the laboratory. $\mathbf{L}_\Omega(t)$ is the zero field propagator in the laboratory frame. We then write

$$F_\Omega(t) = \langle I_z|\mathbf{R}(\Omega)\, \mathbf{L}_m(t)\, \mathbf{R}^\dagger(\Omega)\, |I_z\rangle \quad , \tag{153}$$

where

$$\mathbf{L}_m(t) = \mathbf{R}^\dagger(\Omega)\, \mathbf{L}_\Omega(t)\, \mathbf{R}(\Omega) \tag{154}$$

is the homogeneous propagator in the molecular frame. $|I_z\rangle$ can easily be expressed in terms of operators in the molecular frame through the Wigner rotation matrices

$$\begin{aligned}\mathbf{R}(\Omega)I_z\mathbf{R}^\dagger(\Omega) &= D^{(1)}_{00}(\Omega)I_{zm} - D^{(1)}_{10}(\Omega)\frac{1}{\sqrt{2}}I_{+m} + D^{(1)}_{-10}\frac{1}{\sqrt{2}}I_{+m} \\ &= I_{zm}\cos\beta - I_{xm}\sin\beta\cos\alpha + I_{ym}\sin\beta\sin\alpha\end{aligned} \quad . \tag{155}$$

Inserting (155) into (153) we obtain

$$\begin{aligned}F_\Omega(t) = \langle &(I_{zm}\cos\beta - I_{xm}\sin\beta\cos\alpha + I_{ym}\sin\beta\sin\alpha)|\mathbf{L}_m(t)| \\ &(I_{zm}\cos\beta - I_{xm}\sin\beta\cos\alpha + I_{ym}\sin\beta\sin\alpha)\rangle\end{aligned} \quad . \tag{156}$$

45. Average Over Orientational Distribution

Expression (156) must now be averaged over the distribution $P(\Omega)$ to give the signal for the sample

$$F(t) = \int F_{\Omega}(t)\ P(\Omega)d\Omega \tag{157}$$

For an isotropic three dimensional distribution, as in a random powder, all Ω are equally probable, i.e.

$$P(\Omega) = \text{const} \quad , \tag{158}$$

and only three terms in (156) survive the integration of (157). The result is

$$F(t) = \frac{1}{3}(\langle I_{xm}|\mathbf{L}_m(t)|I_{xm}\rangle + \langle I_{ym}|\mathbf{L}_m(t)|\ I_y\ \rangle + \langle I_{zm}|\mathbf{L}_m(t)\ |\ I_{zm}\rangle) \tag{159}$$

Expanding (159) in an eigenbasis of $\mathbf{L}_m(t)$ in the manner of section 8, we obtain the final expression

$$F(t) = \frac{1}{3}\sum_{j,k}(|I_{xmjk}|^2 + |I_{ymjk}|^2 + |I_{zmjk}|^2)\cos\omega_{jk}t \quad , \tag{160}$$

where I_{xmjk} is the (j,k)th matrix element of I_{xm}. This expression implies that the signal will be linearly polarized along z, and that the Fourier transform spectrum is symmetric around zero frequency. This behavior is expected, of course, because of the axial symmetry around z manifested by (158).

46. Dipolar Coupled Spin-1/2 Pair or Quadrupolar Spin-1

We can now evaluate (160) explicitly for the most basic cases of zero field NMR and NQR. Consider two spins I = 1/2 with an axially symmetric

dipolar coupling. With the molecular z axis along the symmetry axis established by the internuclear vector the molecular frame Hamiltonian in frequency units is

$$H_{Dm} = \omega_D \, (3I_{zm1}I_{zm2} - \underset{\sim}{I}_1 \cdot \underset{\sim}{I}_2) \quad , \tag{161}$$

where the dipolar frequency ω_D is

$$\omega_D = \gamma^2 / r^3 \quad . \tag{162}$$

The well-known eigenstates of (161) are depicted in **Figure 53a**: a triplet 1,2,3 (with a degenerate pair 1,2) and a singlet S. The only non-zero matrix elements in (160) are within the triplet manifold. The frequencies are

$$\omega_{12} = 0 \tag{163}$$

$$\omega_{13} = \omega_{23} = \frac{3}{2} \omega_D \quad .$$

Plugging all this into (160) and recalling that we are working with a normalized signal $\langle I_z | I_z \rangle = 1$, as in section 8, we obtain

$$F(t) = \frac{1}{3} \, (1 + 2\cos \frac{3}{2} \omega_D t) \quad , \tag{164}$$

which predicts a spectrum of lines with equal intensities at $0, \pm 3\omega_D/2$, as shown in the lower part of Figure 53(a). Such a spectrum is indeed observed experimentally for a pair of protons, as we saw previously in Figure 50. **Figure 53b** reminds us that the situation is entirely analogous to a single spin I = 1 (cf.the three level system of section 14) if $\eta = 0$. Remember however, that here we are in the molecular frame for all Ω. The triplet manifold is analogous to that of the dipolar coupled pair and there is no singlet state.

For both the dipolar coupled pair and the single spin I=1, where the

asymmetry parameter η is non-zero, the zero field transitions are split as shown in **Figure 53 c and d.** The molecular frame Hamiltonian for the dipolar case is

$$H_{Dm} = \omega_D[3I_{zm1}I_{zm2} - \underset{\sim}{I}_1 \cdot \underset{\sim}{I}_2 + \eta(I_{xm1}I_{xm2} - I_{ym1}I_{ym2})] \quad , \qquad (165)$$

which splits the ω_{12} transition,

$$\omega_{12} = \eta\omega_D \quad . \qquad (166)$$

For the quadrupolar case, the Hamiltonian is

$$H_{Qm} = A[3I_{zm}^2 - \underset{\sim}{I}^2 + \eta(I_{xm}^2 - I_{ym}^2)] \quad , \qquad (167)$$

with the quadrupole coupling constant

$$A = \frac{e^2qQ}{4} \qquad (168)$$

Thus the effects of small asymmetry are clearly visible as sharp splittings in the spectrum, although similar effects may be difficult to discern in high field powder patterns. This agreeable feature of zero field NMR was mentioned in section 41 and was quite clear in the experimental spectra of Figures 47 and 48. Consequently, zero field NMR spectra may provide a useful measure of small amplitude motions and subtle deviations from local symmetry in disordered systems. Examples of these effects, for example in biaxial smectic phases, have appeared in the literature and might prove useful for biological applications in the future.

47. **Effects of Motion**

As an example of the effect of introducing a small non-zero asymmetry parameter through motion, consider an axially symmetric dipolar or

quadrupolar coupling tensor where the symmetry axis jumps randomly through an angle of 2θ. When the jump rate κ increases from zero, the zero field spectrum should change from the static (axially symmetric) case to the time averaged case, in analogy to high field NMR studies of chemical exchange and motion.

Examples of spectra simulated for a quadrupolar spin and different relative jump rates (κ/A) are shown in **Figure 54** for $2\theta = 20^{\circ}$ and in **Figure 55** for $2\theta = 90^{\circ}$. The first case, $2\theta = 20^{\circ}$, displays the onset of a small motionally induced asymmetry parameter ($\eta \neq 0$). In the second case $2\theta = 90^{\circ}$, the jumps are equivalent to four-fold jumps around an axis (due to the symmetry of the Hamiltonian under 180° rotations) leading to a time averaged axially symmetric coupling.

48. Bibliography

The work presented in these lectures has been described in detail in the literature. I have not referred to specific papers by us or others during the lectures since I wished to convey only the overall flavor of these rapidly developing areas. As an entry into the literature, I present below a very brief bibliography of selected papers from our group at Berkeley during the last few years. Many of these papers have been deposited in the Fermi School Library and they contain extensive and detailed references to our work and to the work of other laboratories in the field. The papers range from popular review type articles (e.g. in Science) to formal presentations (e.g. in Physical Review). For multiple quantum spectroscopy, I mention that there are also extensive reviews by G. Bodenhausen (Progr. Mag. Reson., 14, 137-173, 1981); G. Drobny (Ann. Rev. Phys. Chem., 36, 451-489 (1985)); D. Weitekamp (Adv. in Magn. Res., 11, 111-274, (1983); and M. Munowitz (Adv. Chem. Phys., 66, 1 (1986). A detailed source of information on solid state and multiple quantum NMR is also the book by M. Mehring (High Resolution NMR in Solids, 1985, 2nd ed.). Some unpublished and very useful pedagogical material appears in theses from our laboratory of which most of the following are in the Fermi School Library:

J. Baum - NMR Studies of Spin Clustering;

H. Cho - Iterative Maps and Bistable Excitation on SO(3);

G. Drobny -NMR Studies of Liquid Crystals and Molecules Dissolved in Liquid Crystals;

R. Eckman - Hydrogen and Deuterium NMR of Solids by Magic Angle Spinning;

J. Garbow - Heteronuclear Dipolar Couplings, Total Spin Coherence, and Bilinear Rotations in NMR Spectroscopy;

M. Gochin - SHARP and Two-Dimensional NMR of Oriented Molecules;

J. Millar - Proton and Deuterium NMR and NQR Spectra in Zero Field;

J. Murdoch - Computer Studies of Multiple-Quantum Spin Dynamics;

L. Sterna - Effect of Nuclear Spin on Chemical Reactions and Molecular Rotation

J. Tang - NMR Study of Correlations in Molecular Motion;

A. Thayer - Zero Field NMR of Solids and Liquid Crystals;

R. Tycko - Broadband Excitation and Fixed Point Theory;

W. Warren - Selectivity in Multiple-Quantum NMR;

D. Weitekamp - Time Domain Multiple-Quantum NMR;

D. Wemmer - Double Resonance and Motion in Solid State NMR;

D. Zax - Fourier Transform Zero Field NMR.

Selected Papers from Berkeley Laboratory

Multiple-Quantum NMR Spectroscopy, Science, 233, 525-531 (1986). (M. Munowitz).

Multiple-Quantum Dynamics in NMR: A Directed Walk in Liouville Space, J. Chem. Phys. submitted (M. Munowitz and M. Mehring)

Multiple-Quantum NMR Studies of Clustering in Hydrogenated Amorphous Silicon, Phys. Rev. Lett., 56, 1377-1380 (1986). (J. Baum, K.K. Gleason, A.N. Garroway, and J. Reimer).

Theory of Selective Excitation of Multiple-Quantum Transitions, J. Chem. Phys., 73, 2084-2099 (1980). (W.S. Warren and D.P. Weitekamp).

Computer Simulations of Multiple-Quantum NMR Experiments, J. Magn. Reson., 60, 205-256 (1984). (W.S. Warren and J.B.

Murdoch).

Multiple-Quantum NMR and Relaxation of an Oriented CH_3 Group, J. Chem. Phys., 72, 3290-3297 (1980). (J. Tang).

Double-Quantum Cross Polarization NMR in Solids, Phys. Rev. A., 22, 638-661 (1980). (S. Vega and T.W. Shattuck).

Bilinear Rotation Decoupling of Homonuclear Scalar Interactions, Chem. Phys. Lett., 93, 504-509 (1982). (J.R. Garbow and D.P. Weitekamp).

Determination of Dipole Coupling Constants Using Heteronuclear Multiple-Quantum NMR, J. Chem. Phys., 77, 2870-2883 (1982). (D.P. Weitekamp and J.R. Garbow).

Multiple-Quantum NMR Study of Molecular Structure and Ordering in a Liquid Crystal, Mol. Phys., 53, 333-362 (1984). (S.W. Sinton, D. Zax and J.B. Murdoch).

Determination of Dipole-Dipole Couplings in Oriented n-Hexane by Two-Dimensional NMR, J. Am. Chem. Soc., in press. (M. Gochin, K. V. Schenker and H. Zimmermann).

Symmetric Phase Alternating Composite Pulses, J. Magn. Reson., in press. (A.J. Shaka).

Iterative Maps for Bistable Excitation of Two Level Systems, Phys. Rev. Lett., 56, 1905-1908 (1986). (H.M. Cho, R. Tycko, and J. Guckenheimer).

Fixed Point Theory of Iterative Excitation Schemes in NMR, J. Chem. Phys., 83, 2775-2802 (1985). (R. Tycko and J. Guckenheimer).

High Resolution NMR with a Surface Coil, J. Am. Chem. Soc., 107, 7193-7194 (1985). (M. Gochin).

Broadband and Adiabatic Inversion of a Two-Level System by Phase Modulated Pulses, Phys. Rev. A. 32, 3435-3447 (1985). (J. Baum and R. Tycko).

Spatially Selective NMR with Broadband RF Pulses, Chem. Phys. 105, 7-14 (1986). (J. Baum and R. Tycko).

Nutation Sequences for Magnetic Resonance Imaging in Solids, Phys. Rev. Lett. 16, 1923-1926 (1985). (H.M. Cho, C.J. Lee, D.N. Shykind and D.P. Weitekamp).

NMR Imaging in Solids by Multiple-Quantum Resonance, J. Magn. Reson. 60, 337-341 (1984). (A.N. Garroway, J. Baum and M. Munowitz).

Deuterium NMR in Solids with a Cylindrical Magic Angle Sample Spinner, J. Magn. Reson. 41, 440-446 (1980). (R. Eckman and M. Alla).

Dipolar Relaxation by Rotation in Spin Space, J. Magn. Reson., 45, 94-101 (1981). (S. Emid and J. Smidt).

Viscosity and Temperature Dependence of the Magnetic Isotope Effect, J. Chem. Phys., 73, 5493-5499 (1980). (L. Sterna, D. Ronis, and S. Wolfe).

Indirect Phase Detection of NMR Spinor Transitions, Phys. Rev. Lett., 57, 242 (1986). (D. Suter and M. Mehring).

Zero Field NMR, Accts. Chem. Res., in press (A.M. Thayer).

Theory of Chemical Exchange in Zero Field NMR: Two-Site Flips, Chem. Phys., in press. (P. Jonsen, M. Luzar, and M. Mehring).

NMR Study of Molecular Reorientation under Fivefold Symmetry - Solid Permethylferrocene, J. Am. Chem. Soc., 103, 28-36 (1981). (D.E. Wemmer and D.J. Ruben).

Two-Dimensional Zero Field NMR, Chem. Phys. Lett., in press. (A.M. Thayer and J. M. Millar).

Zero Field NMR and NQR Spectrometer, Rev. Sci. Instrum., 57 (3), 393-403 (1986). (A. Bielecki, D.B. Zax, and K.W. Zilm)

A New Probe for High-Temperature Nuclear Magnetic Resonance Spectroscopy

with PPM Resolution, Rev. Sci. Instrum., 57 (1), 39-42 (1986). (J.F. Stebbins, E. Schneider, J.B. Murdoch, and I.S.E. Carmichael).

Zero Field NMR of a Nematic Liquid Crystal, J. Phys. Chem., 90, 1577-1581 (1986) (A.M. Thayer, J.M. Millar, M. Luzar, and T.P. Jarvie).

Zero Field NMR and NQR, J. Chem. Phys., 83, 4877-4905 (1985). (D.B. Zax, A. Bielecki, K. Zilm, and D.P. Weitekamp).

Time-Resolved Optical Nuclear Polarization, Chem. Phys. Lett., 93, 392-395 (1982). (R. Tycko and D. Stehlik).

Acknowledgements

I am grateful to M. Gochin, M. Munowitz, and A. Thayer for critical comments and extensive help with the manuscript and figures, and to A. Bielecki, H. Cho, C. Lee, E. Hahn, R. Harris, and M. Mehring for many interesting and helpful discussions. The coworkers in my research group have been a constant source of inspiration and stimulation and it is their creativity and contributions over the years which have made these lectures possible. The work in our laboratory is supported through the Lawrence Berkeley Laboratory by the Director, Office of Energy Research, Office of Basic Energy Sciences, Materials Sciences Division of the U.S. Department of Energy under Contract No. DE-AC03-76SF00098.

Figure Captions

1. Experimental (EXP) one-quantum proton NMR spectrum of benzene oriented in a liquid crystal, compared with simulated spectra of symmetric six-carbon structures. The isotropic spectrum, consisting of one line (bottom), is compatible with all these structures. (Courtesy of Z. Luz).

2. Proton NMR spectra of oriented molecules with various numbers of spins. The spectral complexity increases exponentially with the size of the spin system. (Courtesy of Z. Luz).

3. Proton NMR spectrum of n-hexane-d_6 in isotropic solution. All protons have roughly the same chemical shift, and give one line at this level of resolution. The line at right is from a TMS standard. (Adapted from Chem. Phys., in press (1986), with permission).

4. Proton NMR spin echo spectrum of oriented n-hexane-d_6 (deuterated methyls) with deuterium spin decoupling, to be compared with the isotropic spectrum in Figure 3. Even for this system of eight protons, there are about three thousand transitions, and the spectrum is intractable. (Adapted from Chem. Phys., in press (1986), with permission).

5. Energy level diagram of a system of N coupled spins-1/2 in high magnetic field. The groups of energy levels are characterized by the

magnetic Zeeman quantum number M. The splittings in each group are due to chemical shifts and couplings between the spins. The solid vertical lines indicate allowed ($\Delta M = \pm 1$) one-quantum transitions and the dashed vertical lines depict some "forbidden" multiple-quantum ($\Delta M = \pm n$, $n = 0, 1, \ldots, N$) transitions. (Adapted from J. Chem. Phys., 73, 2084, (1980), with permission).

6. Multiple-quantum NMR spectra of oriented benzene, showing the progressive simplification as the number of quanta increases from 1 to 6. The spectra were averaged over a range of preparation and mixing times. We can see one six-quantum transition, two five-quantum transitions, and seven four-quantum transitions, as anticipated in the text. (Courtesy of G. Drobny).

7. Contour plot of the two-dimensional multiple-quantum spectrum of oriented benzene and expansion of the four-quantum region. These plots show how coherence is transferred between the multiple-quantum evolution period (vertical axis) and the one-quantum detection period (horizontal axis). The preparation and mixing times were nine milliseconds. (Courtesy of G. Drobny).

8. Timing diagram for basic multiple-quantum sequence. The multiple-quantum coherences are prepared from an initial high temperature equilibrium state $\rho(0) \sim I_z$ by the propagator $\mathbf{U}(\tau)$; they evolve under the propagator $\mathbf{L}(t_1)$, and after mixing by $\mathbf{V}(\tau')$ they are detected indirectly as z magnetization. This scheme is analagous to detecting x

and y components in t_2 by adding or omitting pulses from **V**. By using different **V**'s, quadrature phases can be detected in t_1.

9. Effect of time-reversal detection. In a), the propagators **U** and **V** are not conjugate (for example **U** = **V** in the three pulse multiple-quantum experiment ($x\text{-}\tau\text{-}\bar{x}\text{-}t_1\text{-}x\text{-}t_2$)), and the uncorrelated phases of nearby transitions can reduce the integrated intensity. In b), with time reversal detection, $\mathbf{U} = \mathbf{V}^{\dagger}$ and the lines are all in phase, thus restoring the full intensity.

10. Deuterium energy levels in the laboratory frame showing the splitting of the one-quantum transitions by the electric quadrupole interaction.

11. Double-quantum free induction decay of deuterium in solid benzene-d_1 doped (10%) into benzene at $-40^{\circ}C$, with proton decoupling. In contrast, the normal one-quantum deuterium free induction signal decays in tens of microseconds. (Courtesy of S. Vega).

12. Fourier transform of the signal in Figure 11, showing the chemical shift anisotropy of deuterium in benzene. The left edge of the spectrum corresponds to the benzene plane normal aligned with the magnetic field; the right peak corresponds to the perpendicular direction. (Courtesy of S. Vega).

13. (a) Symmetry of one-quantum, dipole operators (analagous to p orbitals). The transform like vectors - a phase shift of $\pi/2$

interchanges p_x and p_y, and a phase shift of π changes their signs. (b)Symmetry of double-quantum, quadrupole operators (analogous to p_z, d_{xy} and $d_{x^2-y^2}$ orbitals) involved in the ficitious spin-1/2 double-quantum transition ± 1 in Figure 10. The p_z orbital corresponds to z-magnetization, and the two in plane orbitals, corresponding to double quantum coherence, transform like second rank tensors - a phase shift of $\pi/4$ interchanges d_{xy} and $d_{x^2-y^2}$ and a phase shift of $\pi/2$ changes their signs. (Courtesy of J. Murdoch).

14. Double-quantum spin locking of deuterium in solid benzene-d_1. A "soft" $\pi/2$ pulse was applied at the ± 1 transition to create double-quantum coherence. The rf phase was then shifted by $\pi/4$ to spin lock the coherence for a prolonged period; the coherence was detected by a strong pulse which transformed it into observable one-quantum magnetization. (Courtesy of S. Vega).

15. (a) Three lowest wavefunctions $\psi_n(x)$ and probabilities $|\psi_n(x)|^2$ for a one-dimensional harmonic oscillator.

(b) Coherent superposition of ψ_0 and ψ_1 oscillating between $\psi_0+\psi_1$ and $\psi_0-\psi_1$. The probability density oscillates between left and right in analogy to the dipolar fictitious spin-1/2 discussed in the text.

(c) Coherent superposition of ψ_0 and ψ_2 displaying quadrupole-like oscillations.

16. One-quantum NMR spectrum of the nematic liquid crystal p-pentyl-p'

cyanobiphenyl-d_{11} (5CB) at 26.0°C. The total frequency bandwidth is 50 kHz. (Adapted from Mol. Phys., 53, 333, (1984) with permission).

17. Six-quantum spectrum of 5CB, to be compared with Figure 16. This spectrum could be analyzed to yield the order tensor as well as the structure and dynamics of the biphenyl group. The lower plots are simulations (stick spectrum and slightly broadened spectrum) based on this structure. The total frequency bandwidth is 44.2 kHz. Several spectra with different preparation and mixing times were used to obtain more uniform intensities for the lines. (adapted from Mol. Phys., 53, 333 (1984), with permission).

18. Five-quantum spectrum of 5CB showing the onset of complexity as we progress (or regress) from six quanta (Figure 17) towards one quantum (Figure 16). The simulation in the lower plots was produced from the structural and dynamical parameters derived from the six-quantum spectrum. The total frequency bandwidth is 62.5 kHz. Here too, spectra from a range of preparation and mixing times were averaged together. (Adapted from Mol. Phys., 53, 333 (1984), with permission.)

19. (a) Double-quantum filtered two-dimensional correlated spectrum of 81% randomly deuterated n-hexane, 23 mole % in EK 11650, taken with the pulse sequence described in the text with deuterium decoupling. (128 x 1024)-point data sets were collected at 360 MHz, with a spectral width of 16,667 Hz in both dimensions. The square patterns, which reveal dipole couplings in individual isotopomers, are shown for four of the

sixteen proton pairs.

(b) Part of a double-quantum versus single-quantum spectrum obtained using the pulse sequence described in the text. ν_1 is the double-quantum axis and ν_2 is the single-quantum axis. Vertical lines parallel to the ν_2 axis indicate the six possible double-quantum frequencies of molecules with two protons. M, E_1 and E_2 correspond to the methyl and the two inequivalent ethylene positions in hexane. All the dipole couplings in oriented hexane have been determined in this way. (Adapted from J. Am. Chem. Soc., in press (1986), with permission.)

20. Multiple-quantum NMR spectra (ensemble averaged over a range of τ values) of oriented benzene with normal non-selective broadband excitation and with four-quantum selective excitation. Selective n-quantum excitation enhances the n-quantum intensity, which, under non-selective excitation, may be low owing to the statistically low probability of absorbing many quanta. (Adapted from J. Chem. Phys., 74, 2808 (1981), with permission.)

21. Symmetry of two-quantum selectivity by π phase shifting. The first resonant process involves one-quantum each from the upper and lower sidebands. (Adapted from Adv. Mag. Res., 11, 111 (1983), with permission.)

22. Symmetry of three-quantum selectivity by $2\pi/3$ phase shifts. The sidebands are now a symmetrically disposed about the resonance, and the

first resonant process involves two quanta from the lower sideband and one from the upper sideband. (Adapted from Adv. Mag. Res., 11, 111 (1983), with permission.)

23. Timing diagram for the three pulse multiple-quantum scheme. If $t_1 = 0$ in a solid and τ is longer than the solid FID time, the signal is zero; hence the integrated multiple-quantum intensity will be zero as well. This illustration presents another view of the problem outlined in Figure 9. (Adapted from Phys. Rev., in press (1986), with permission.)

24. By replacing the pair of pulses with the lower pulse train and employing phase shifting, time reversal detection can be used to recover the full multiple-quantum intensity in a solid.

25. Multiple-quantum spectra of solid hexamethylbenzene obtained using the lower pulse sequence in Figure 24, with overall preparation and mixing times τ ranging from 66 to 792 microseconds. (The lowest trace, 792 microseconds, is expanded vertically.) As τ increases, more and more spins are correlated and more and more quanta are involved. In excess of one hundred quanta have been observed in this way. (Adapted fromJ. Chem. Phys., 83, 2015 (1985), with permission).

26. (a) Multiple-quantum spectra of the liquid crystal 5CB (containing 21 protons) showing a Gaussian distribution of intensities.

(b) Number of correlated spins $N(\tau)$ ($\equiv$ maximum number of quanta) as a function of the preparation and mixing times τ in 5CB. $N(\tau)$ is

extracted from an analysis of the Gaussian intensity distribution of (a) as a function of τ. The plateau at 21 indicates that these molecules contain isolated clusters of 21 proton spins. (J. Am. Chem. Soc. in press (1986), with permission).

27. Schematic of $N(\tau)$, the number of correlated spins or maximum number of quanta as a function of preparation time τ for various distributions of spins. This type of behavior has been observed in a variety of systems, including molecular crystals, molecules in zeolites, liquid crystals, adsorbed species on surfaces, and hydrogenated amorphous semiconductors.

28. High resolution surface coil experiment on two capillary tubes A + B placed on axis at 2 and 4 mm from the coil. Tube A contained 3 microliters of a carbon-13 enriched alanine solution and B contained 2 microliters carbon-13 enriched ethanol. (a) Carbon-13 spectrum illustrating the inhomogeneous field. (b) High resolution SHARP spectrum, non-selective, implemented as described in text. (c) High resolution SHARP spectrum, pulse times set for selectivity at A. (d) SHARP spectrum, pulse times set for selectivity at B. (Adapted from J. Am. Chem. Soc., 107, 7193 (1985), with permission.)

29. (a) Proton linewidth in solid DMSO-d_6 at -75°C under deuterium double-quantum coupling as the deuterium spins are irradiated at various frequencies $\Delta\nu$ from resonance. δ/δ_0 corresponds to δ_s in the text. Note the sensitivity of the decoupling to the I resonance condition, a

characteristic of the double-quantum decoupling process. The solid lines are from theoretical calculations.

(b) Proton linewidth in solid DMSO-d_6 at -75°C as the deuterium spins are irradiated at resonance with various values of ω_1 to induce double-quantum decoupling. The solid line shows the asymptotic $1/\omega_1^4$ behavior expected from theory. The dashed line shows the expected behavior if double-quantum transitions did not occur. (Adapted from Phys. Rev. B. 18, 112 (1978), with permission.)

30. (a) NMR spectra of residual protons in heavy ice (99% deuterium) at -90°C with and without deuterium decoupling. The chemical shift anisotropy of the protons in the hydrogen bonds is ~34 ppm.
(b) As the temperature is raised, the spectra exhibit motional narrowing, with lineshapes characteristic of tetrahedral jumps. This behavior is consistent with the protons hopping between the four hydrogen bonds around the oxygens. (Courtesy of D. Wemmer).

31. Two coupling events between a spin-1/2 or fictitious spin-1/2 and photons in the cavity. A photon is absorbed and the spin is excited, or a photon is emitted and the spin returns to the ground state. This corresponds to the rotating wave approximation.

32. Initial state. The spin is in the excited state and there are n photons in the field.

33. Energy level diagram for a spin-1/2 or fictitious spin-1/2 (two level

system) and a quantized radiation field with photon states $|n\rangle$.

34. Coupling between the spin-1/2 and the radiation causes a level anticrossing at the resonance. From this picture it it easy to visualize how adiabatic rapid passage interchanges the ± states.

35. (a) Coupling events between a spin-1 and photons in a cavity.
(b) Resonant-two photon process in a three-level spin-1 system.

36. Initial state. The spin is in the excited state and there are n photons in the cavity.

37. Energy level diagram for a spin-1 or fictitious spin-1 (three-level system) and a quantized radiation field with photon states $|n\rangle$.

38. Coupling between the spin-1 and the radiation causes level anticrossings. There are two one-photon anticrossings and one two-photon anticrossing. It is possible by adiabatic rapid passage to interchange 0 and -, 0 and + or the ± states. The latter is a two-photon (double-quantum NMR) adiabatic rapid passage.

39. Coupling of two spin systems I and S by cross-relaxation T_{IS}.

40. The Hartmann-Hahn condition. If the magnetic fields B_I and B_S in the rotating frames are such that $\gamma_I B_I = \gamma_S B_S$, then an energy conserving I-S flip-flop can occur, thus inducing cross-polarization from I to S.

41. If the fields B_I and B_S are such that $2\gamma_I B_I = \gamma_S B_S$, then two I spins can flip up and one S spin can flip down. This process is slower than the one in Figure 40, but it ultimately transfers more polarization from I to S. The process can be generalized to $n\gamma_I B_I = \gamma_S B_S$.

42. For a time-dependent Hamiltonian, the evolution can be often characterized by an effective time-independent average Hamiltonian $\bar{H}$. In general, if H(t) is not periodic, then $\bar{H}$ depends on t. If H(t) is periodic, then the same $\bar{H}$ is relevant for multiples of the period.

43. Magic-angle spinning of deuterium in a solid mixture of deuterated hexamethylbenzene and deuterated ferrocene, demonstrating narrowing of the powder line even though the spinning frequency is considerably lower than the ~100 kHz quadrupolar broadened powder linewidth. The two resonances at the bottom (expansion of the centerband in the middle trace) correspond to the isotropic chemical shifts of the two deuterated species. (Adapted from Chem. Phys., 42, 423 (1979), with permission.)

44. High field NMR spectrum of polycrystalline 1,2,3,4-tetrachloronaphthalene bis(hexachlorocyclopentadiene) adduct, a four proton system. As in many dipolar powder patterns, little structure is resolved even though only a small number of spins are strongly coupled together. (Adapted from J. Chem. Phys., 83, 4877 (1985), with permission.)

45. Zero field NMR cycle. The applied field is decreased adiabatically by mechanically shuttling the sample out of the bore of a superconducting magnet. The magnetization, preserved in this process, is maintained by an intermediate field, B_1, which is larger than the local internal fields. A second coil produces a pulsed field B_2 that rapidly cancels all other fields and initiates evolution of the spin system in zero field. The local interactions now determine the axis system in zero field and are identical for all crystallites. Reapplication of the intermediate field terminates the zero field evolution, and the sample is returned to high field, where the magnitude of the signal is measured. The period t_1 is increased incrementally in successive field cycles to produce a time domain signal which produces the zero field NMR spectrum upon Fourier transformation. (Adapted from Accts. Chem. Res., in press (1986), with permission.)

46. Zero field NMR spectrum of the same solid sample shown in Figure 44. The sharp peak at zero frequency is truncated for purposes of display. The evolving zero field magnetization was sampled at 5μs increments to give an effective zero field bandwidth of 100 kHz. From the spectrum the configuration of the four-spin central ring could be determined. (Adapted from J. Chem. Phys., 83, 4877 (1985), with permission.)

47. (a) Deuterium high field NMR spectrum of polycrystalline perdeuterated diethylterephthalate, CD_3CD_2-OOC-C_6D_4-COO-CD_2CD_3. Only the singularities of the methylene and aromatic sites are distinguishable

in this broad powder pattern. Three separate quadrupolar sites can be discernedfrom the overlapping powder lineshapes.

(b) Zero field deuterium NQR spectrum of the same sample. Four distinct frequency regions with resolved peaks are evident corresponding to, in order of decreasing frequency, the aromatic, methylene, methyl sites and the ν_0 lines. Quadrupolar coupling constants and small asymmetry parameters were established for five inequivalent sites in the molecule. (Adapted from J. Magn. Reson., in press (1986), with permission.)

48. Fourier transform zero field deuterium NQR spectrum of polycrystalline perdeuterated 1,4-dimethoxybenzene. The upper plot shows the full spectrum. The lower plot shows expanded views of the three resonance regions assignable to aromatic deuterons, aliphatic deuterons and ν_0 lines. There are two pairs of lines indicating different quadrupole couplings and asymmetry parameters for the aromatic deuterons. The differences are due to the solid state molecular conformation, which renders pairs of the aromatic positions inequivalent. (Adapted from J. Chem. Phys., 80, 2232 (1984), with permission.)

49. Two dimensional zero field cycle and spectrum of selectively deuterated (CD_2) solid diethylterephthalate. The zero field spectrum is obtained as a function of two independent time variables, t_1 and t_2, which are separated by application of an intermediate pulsed field. This mixing transfers coherence between the zero field transitions. As seen in the experimental spectrum, off-diagonal peaks indicate connectivities

between the zero field quadrupolar transitions. In this case, transitions can be assigned to inequivalent deuterium sites in each CD_2 group. (Adapted from Chem. Phys. Lett., in press (1986) with permission.)

50. Two-dimensional zero field - high field dipolar correlation spectrum of polycrystalline $Ba(ClO_3)_2 \cdot H_2O$. For each of 64 values of t_1, the zero field interval, the high field free induction decay after a solid echo sequence is accumulated and stored. A double real Fourier transform in t_1 and t_2 is applied to the signal $S(t_1,t_2)$. At the left and top are the projections of the zero field and high field spectra, and in the center, the correlations between the two frequency domains. Signals which appear at zero frequency in ω_1 correlate most strongly with signals from orientations of the two-spin system which are near the edges of the high field powder pattern. Zero field signals which appear at ~ ±42 kHz correlate to orientations which appear near the peaks (at ~ ±21 kHz) of the high field powder pattern. (Adapted from J. Chem. Phys., 83, 4877 (1985), with permission.)

51. Pulsed field cycling with adiabatic demagnetization and remagnetization. (a) Demagnetized sample (A) differs from one which has resided in zero field for an extended period (B). Both have no magnetization, but A will spontaneously polarize when returned to a field, while B requires a time on the order of the spin lattice relaxaion time, T_1, to polarize. It is this zero field order of A which is exploited after demagnetizing to zero field by applying dc

pulses (for example $\pi/2$ zero field pulses) to initiate evolution for the time t_1. The evolution is terminated by a second pulse and the sample is returned to high field for sampling of the magnetization. This field cycle provides flexibility in employing large fields for brief periods of time, as well as in selective excitation of different spins (e.g. carbon-13 versus protons), by varying the magnitude, direction, and duration of the pulses, and level crossings in heteronuclear spin systems. (Adapted from J. Chem. Phys., 83, 934 (1985), with permission.)

52. Pulsed zero field nitrogen-14 NQR spectrum of solid $(NH_4)_2SO_4$ using the cycle in Figure 51 with selective 2π pulses for the protons. The nitrogen-14 was detected indirectly by level crossing with the protons. Peaks corresponding to two inequivalent nitrogen sites in the unit cell are labeled A and B. Residual proton signal appears below 40 kHz, but has been reduced sufficiently to allow for resolution of the low frequency nitrogen-14 NQR lines. (Adapted from J. Chem. Phys., 83, 934 (1985) with permission.)

53. Energy levels and schematic spectra for two spins-1/2 and for a spin-1 in zero field for $\eta = 0$ and for $\eta \neq 0$. Small deviations from local symmetry, or subtle motional effects, lead to small values of η which are easily observable in zero field.

54. Simulated zero field spectra for jumps of the symmetry axis of a deuterium spin with $\eta = 0$ between orientations differing by $2\theta = 20^{\circ}$.

Only the positive frequency half of the spectra are shown. κ/A, the ratio of the exchange rate to the quadrupolar frequency, varies from the rigid regime (bottom) to the rapid motional limit (top). The ratio of the residual line broadening ($1/T_2$) to the quadrupolar frequency is 0.02. The onset of line splitting due to the motionally induced asymmetry ($\eta \neq 0$) can be seen at large κ/A. The behavior would be similar for the zero field NMR of two coupled spins-1/2. (Adapted from Chem. Phys., in press (1986), with permission.)

55. Same as Figure 54 but $2\theta = 90^{\circ}$. This motion is equivalent to four-fold jumps around an axis, and therefore leads to an axially symmetric motionally averaged spectrum. (Adapted from Chem. Phys., in press (1986), with permission.)

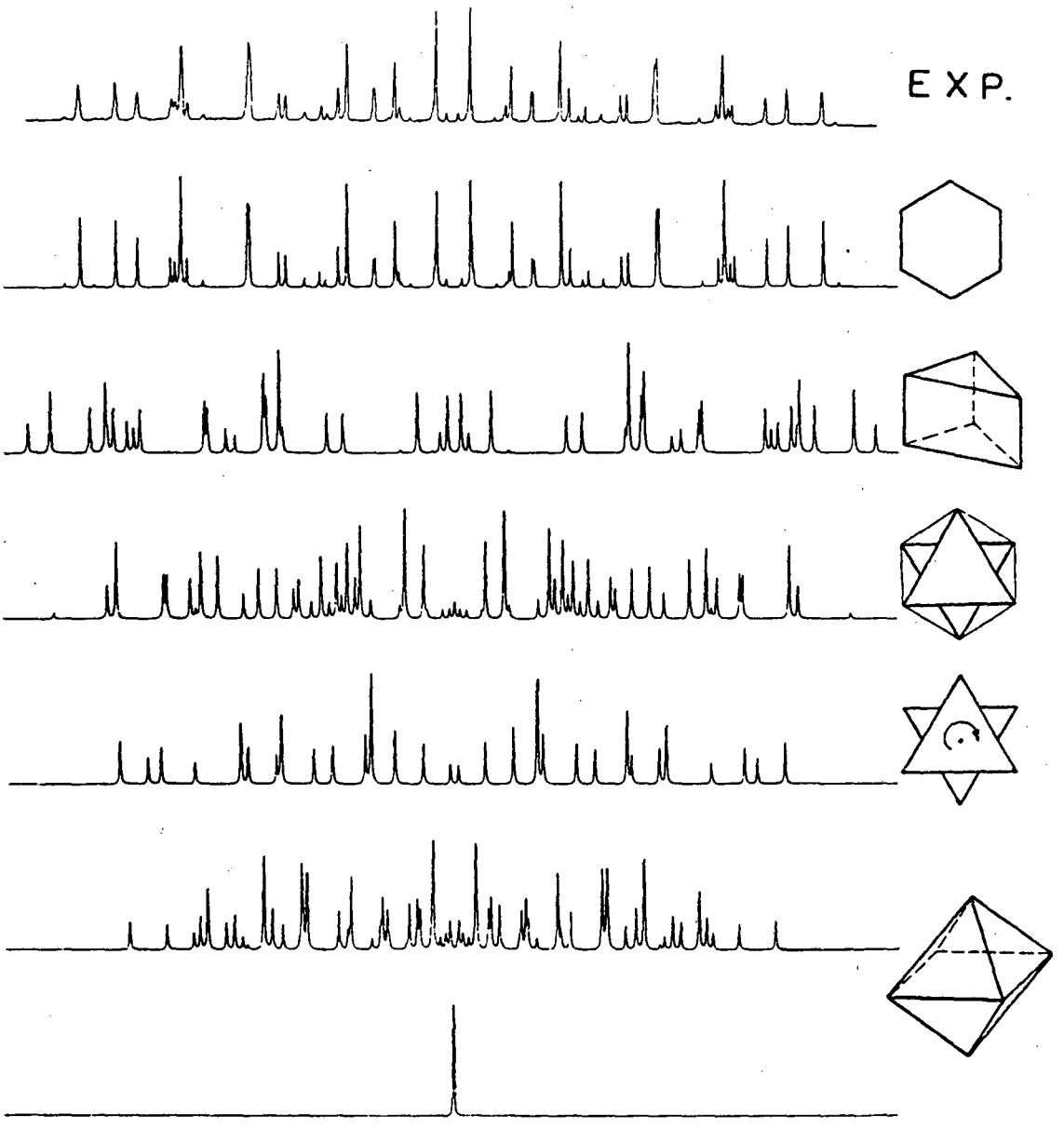

XBL 831-7507

Pines, Fermi Lectures, Figure 1

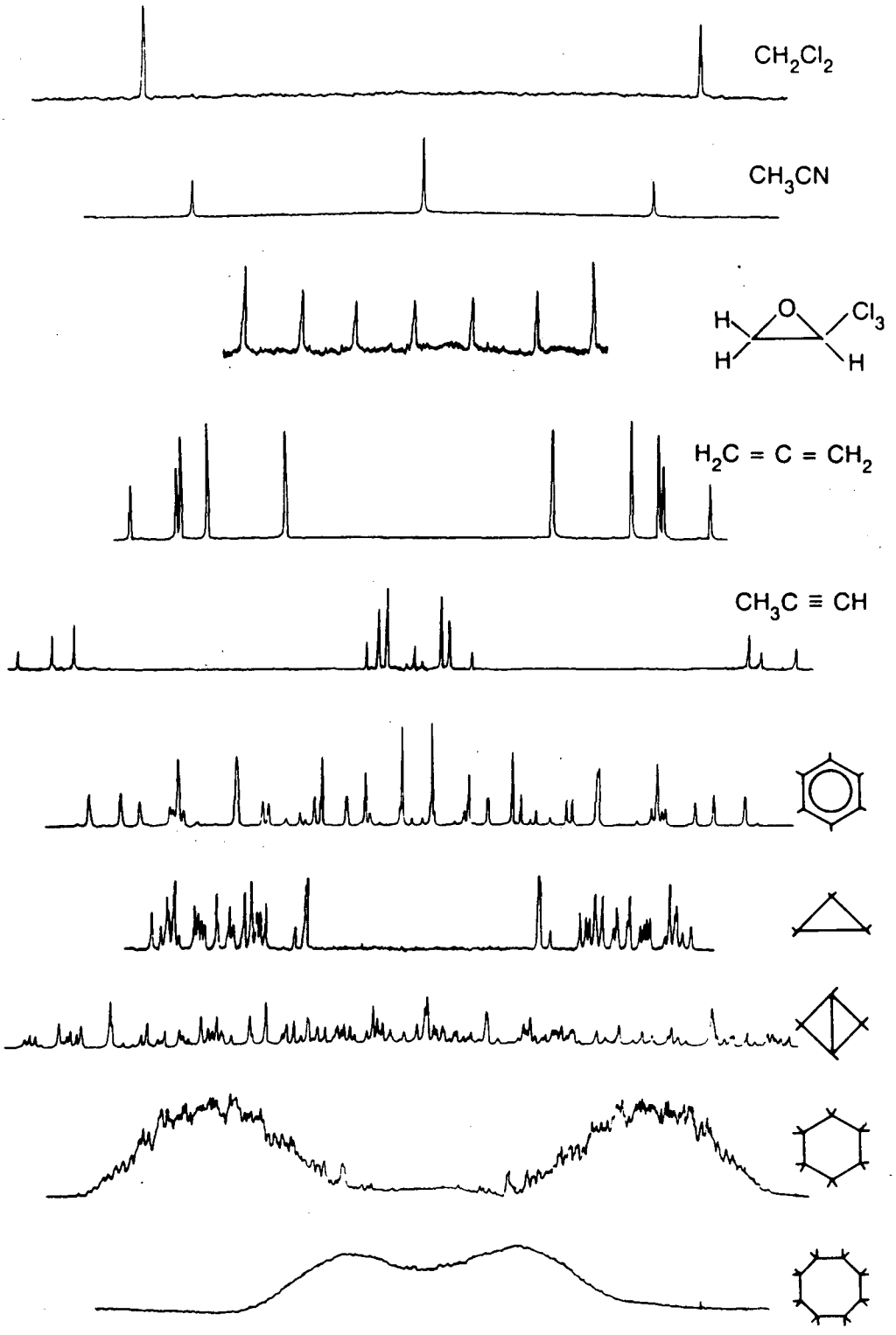

XBL 7910-12344A

Pines, Fermi Lectures, Figure 2

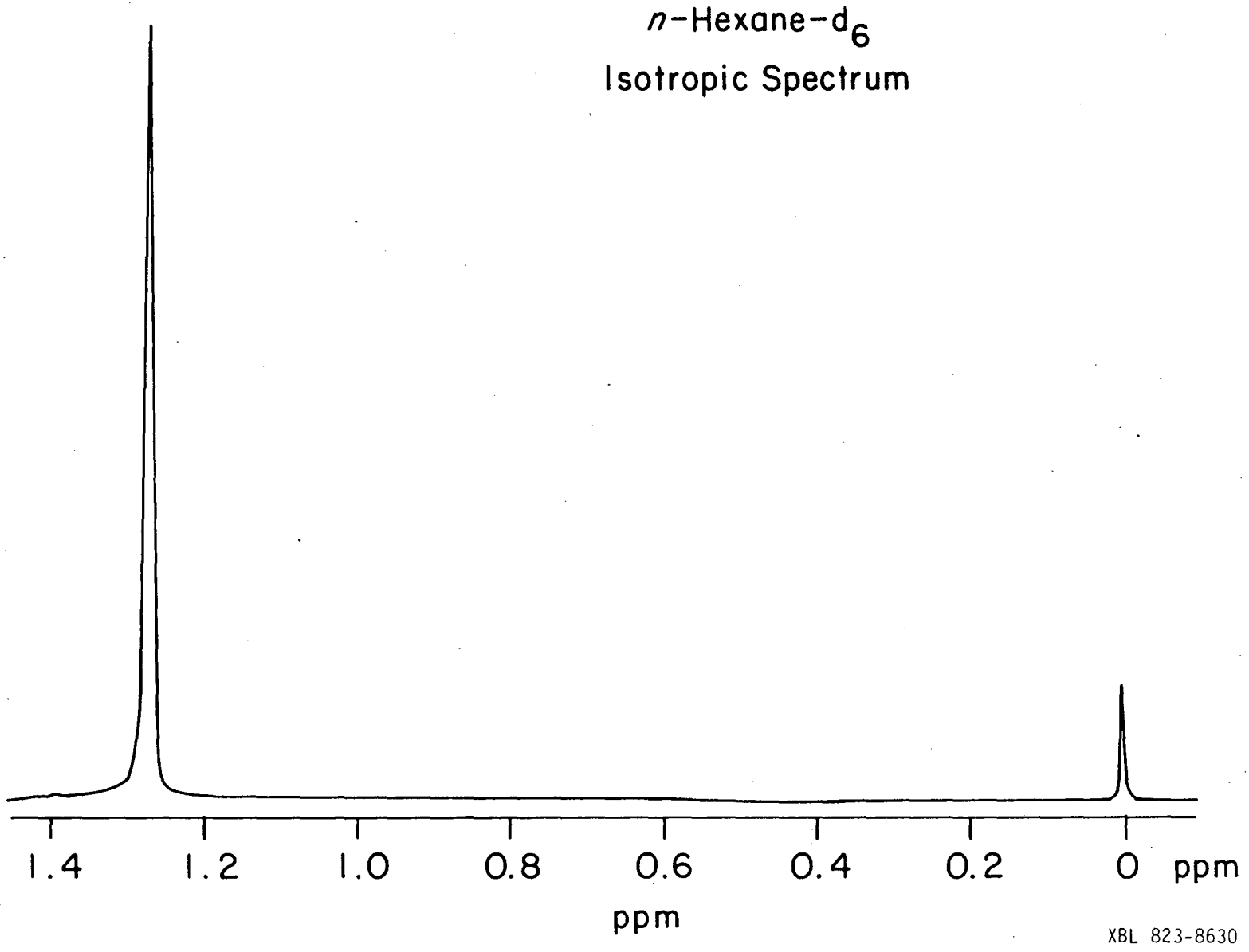

Pines, Fermi Lectures, Figure 3

Oriented *n*-Hexane-d_6
Single Quantum Spectrum

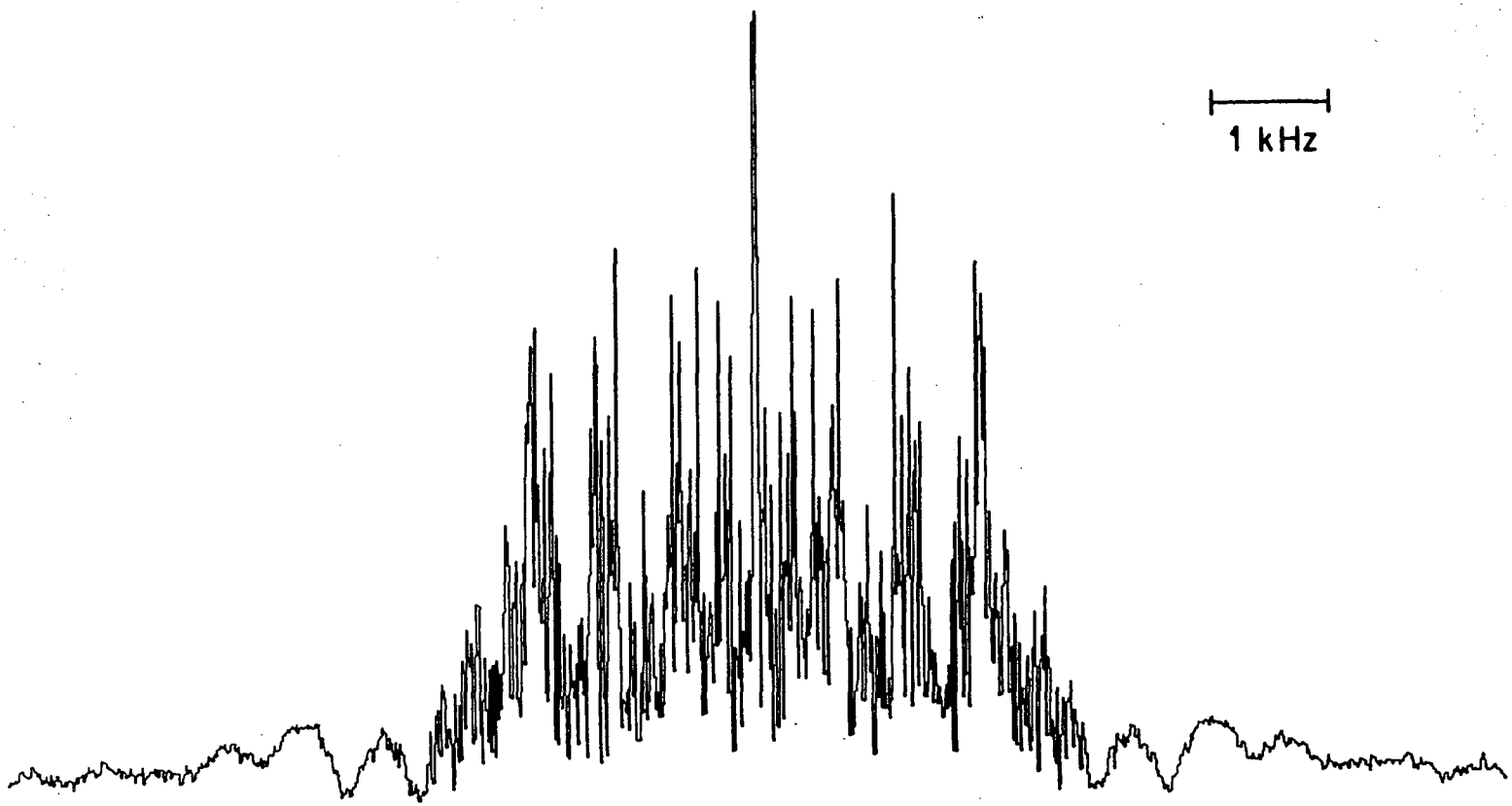

XBL 823-8634

Pines, Fermi Lectures, Figure 4

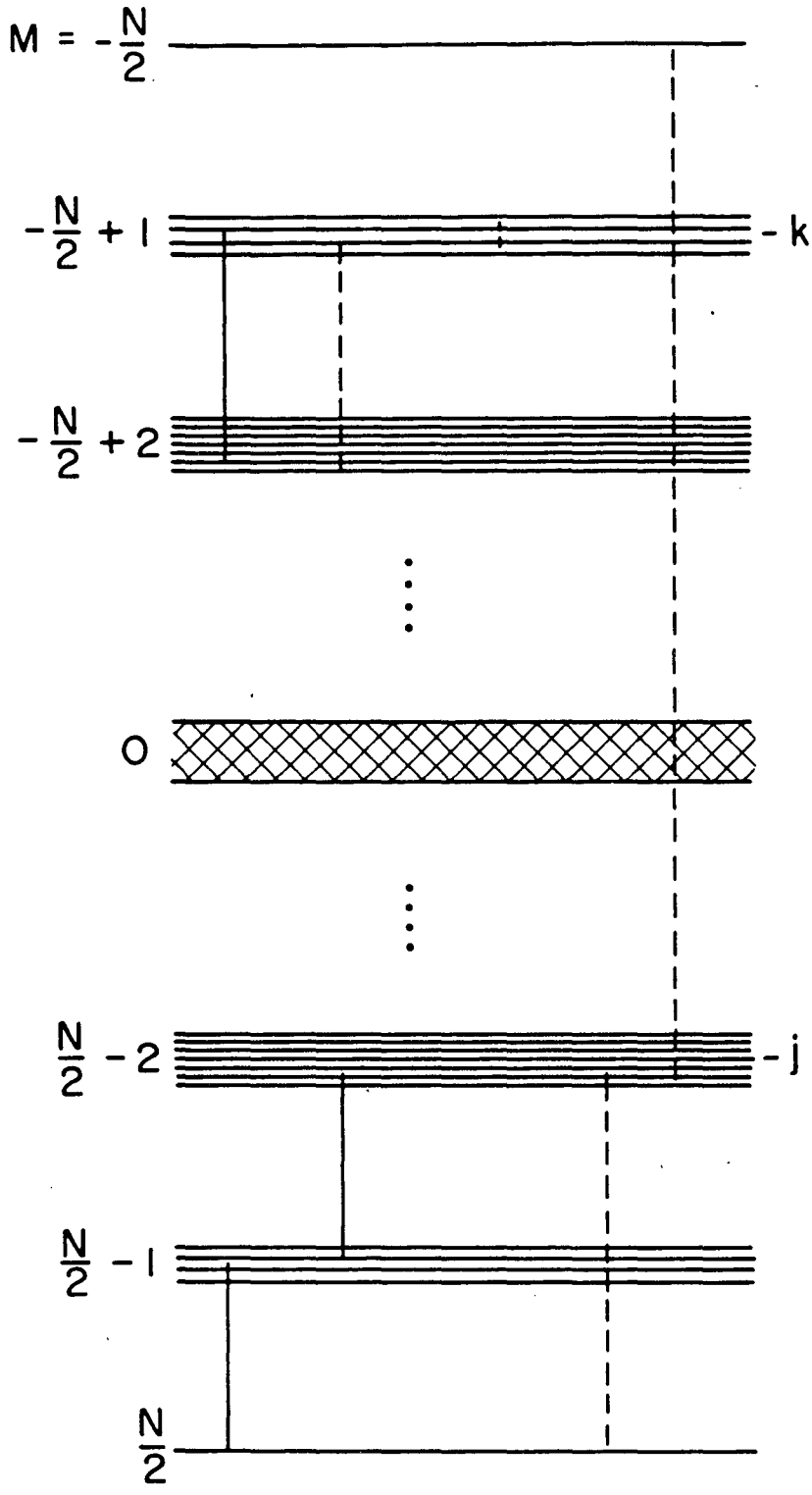

Pines, Fermi Lectures, Figure 5

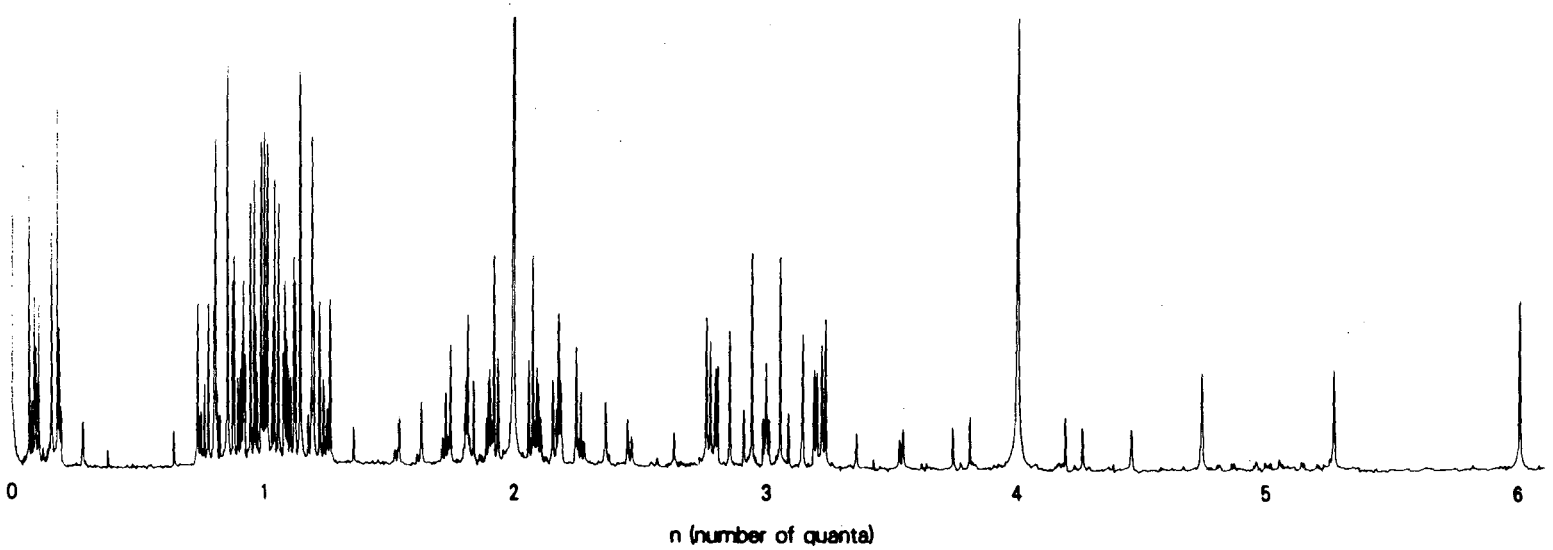

XBL 8610-3766A

Pines, Fermi Lectures, Figure 6

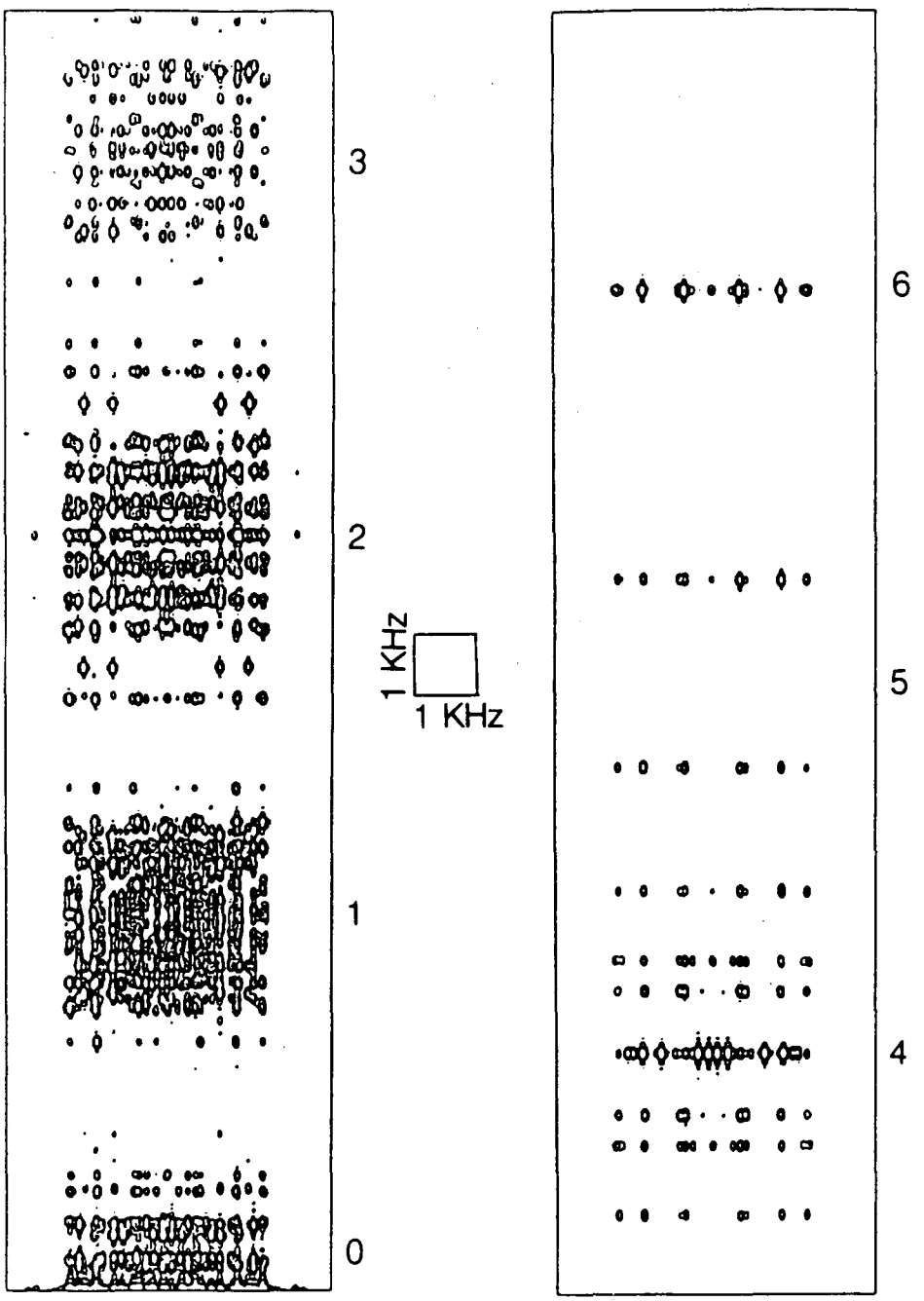

Pines, Fermi Lectures, Figure 7a

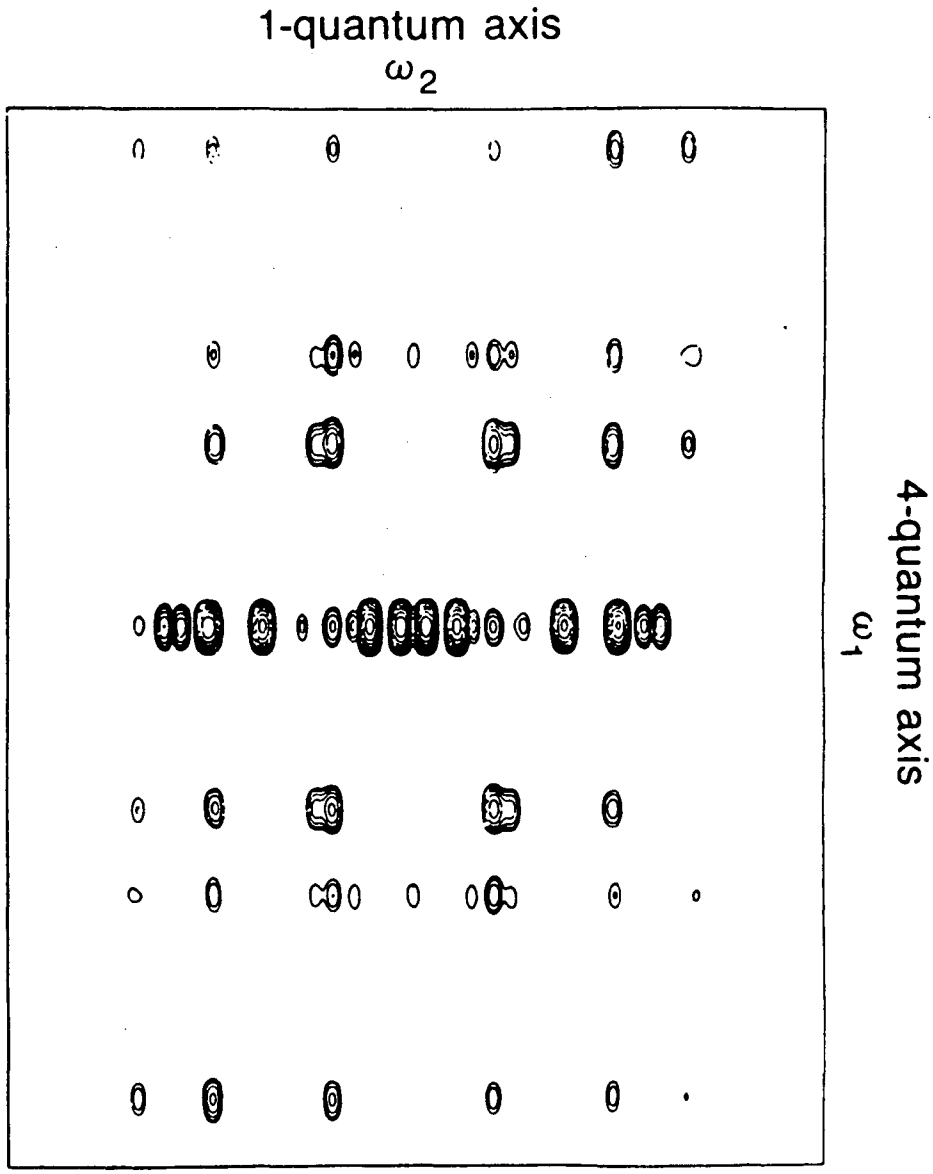

XBL 859-3993

Pines, Fermi Lectures, Figure 7b

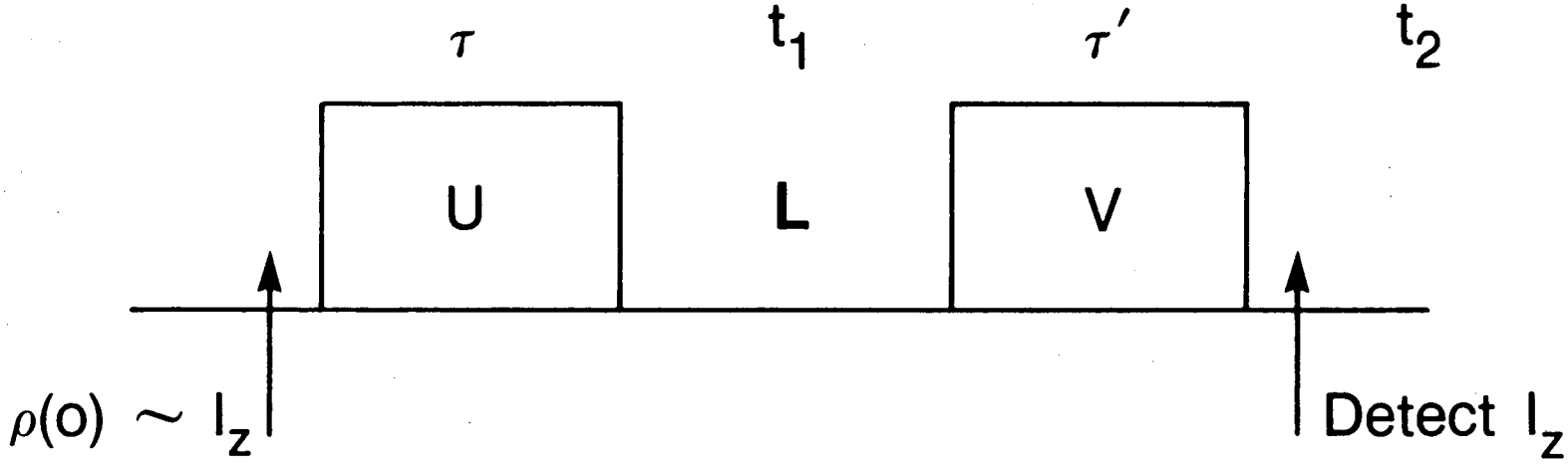

XBL 868-9467

Pines, Fermi Lectures, Figure 8

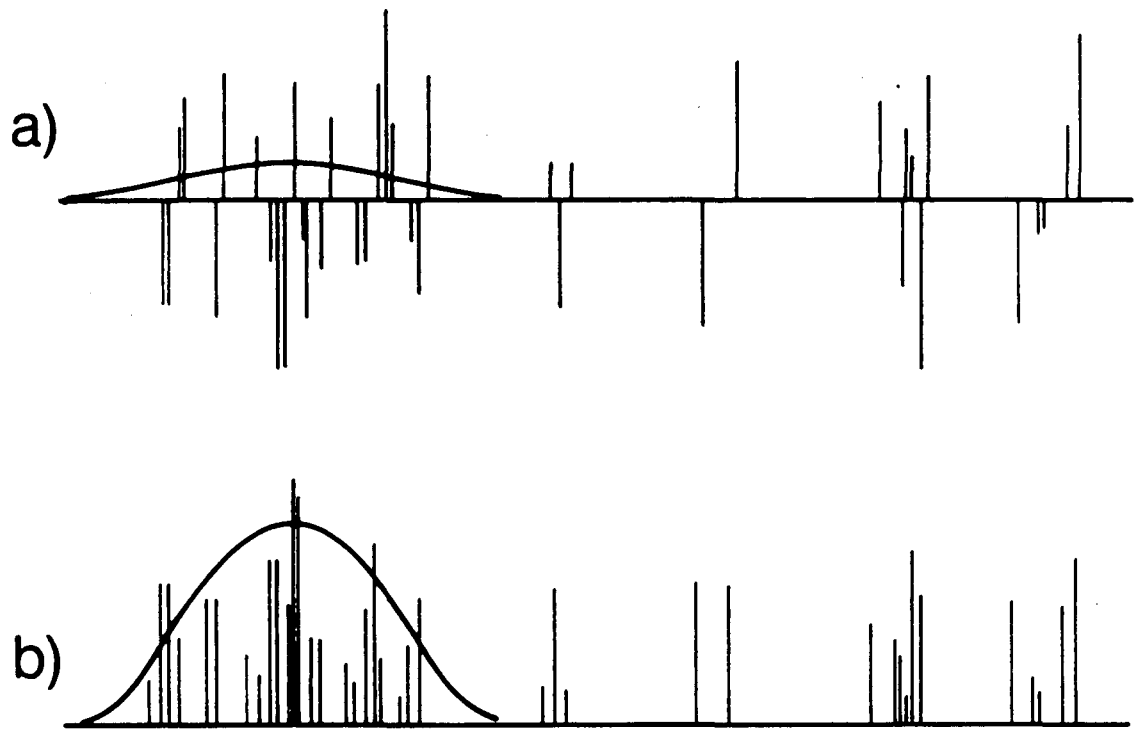

XBL 868-9468

Pines, Fermi Lectures, Figure 9

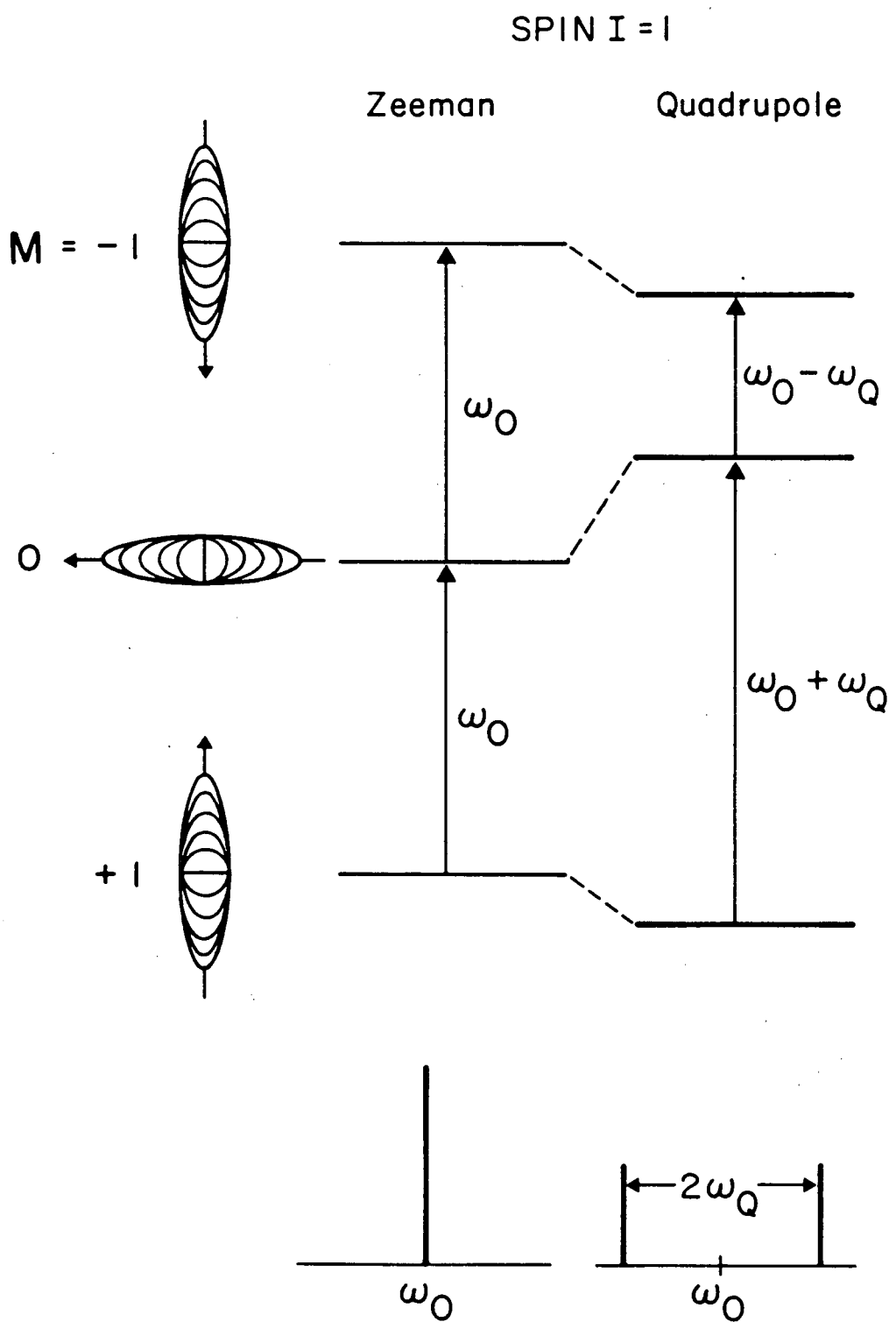

XBL 7710-6863A

Pines, Fermi Lectures, Figure 10

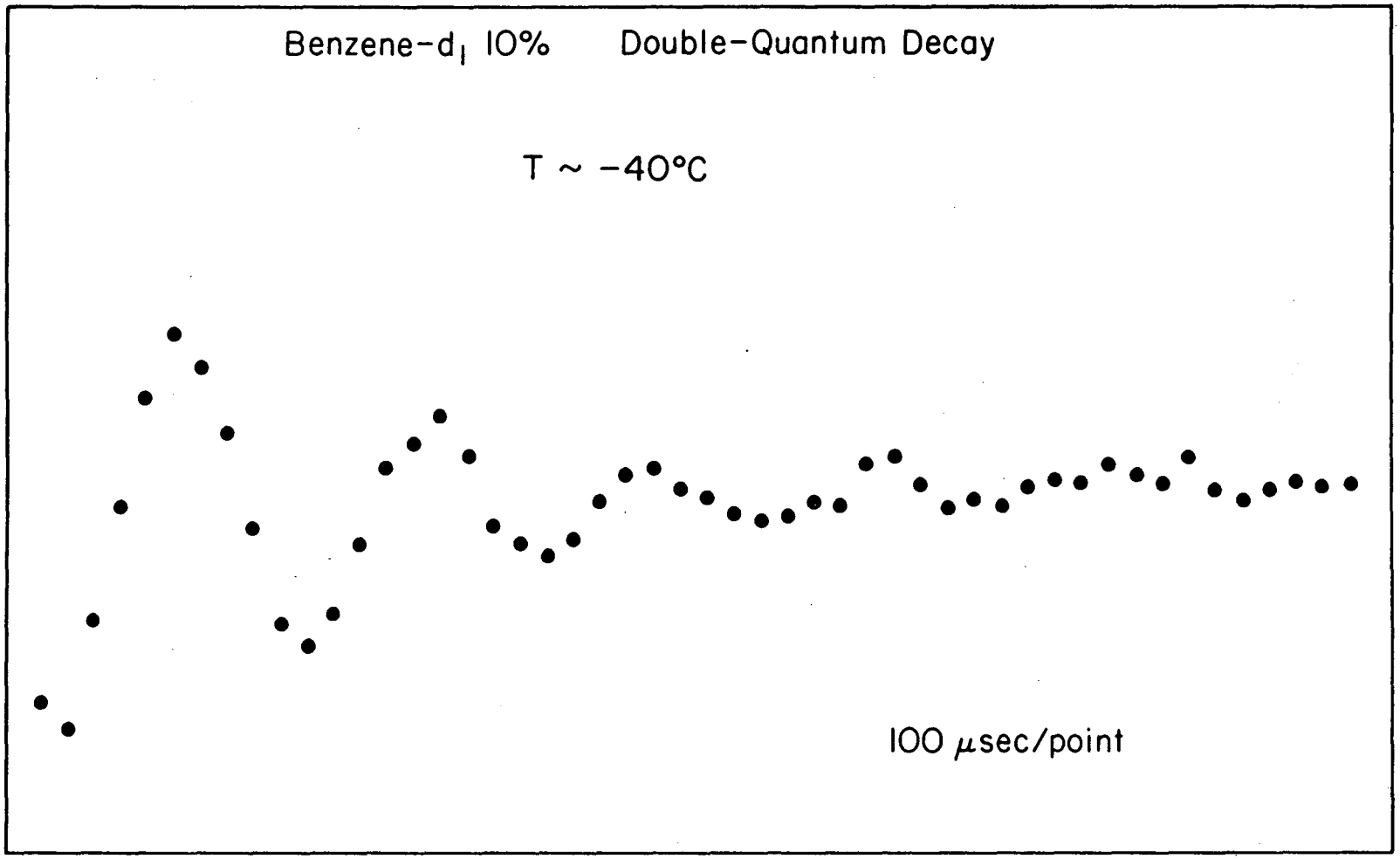

XBL 764-1090

Pines, Fermi Lectures, Figure 11

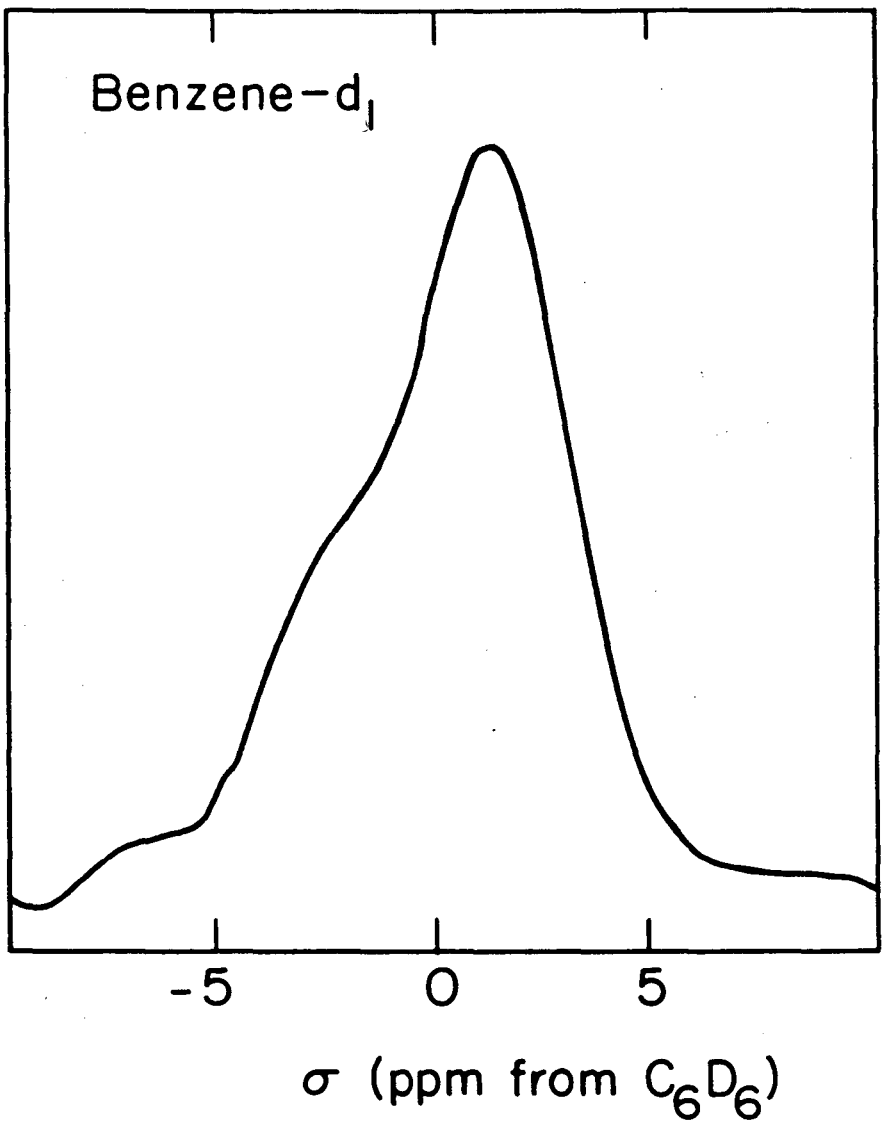

XBL 7710-10025 A

Pines, Fermi Lectures, Figure 12

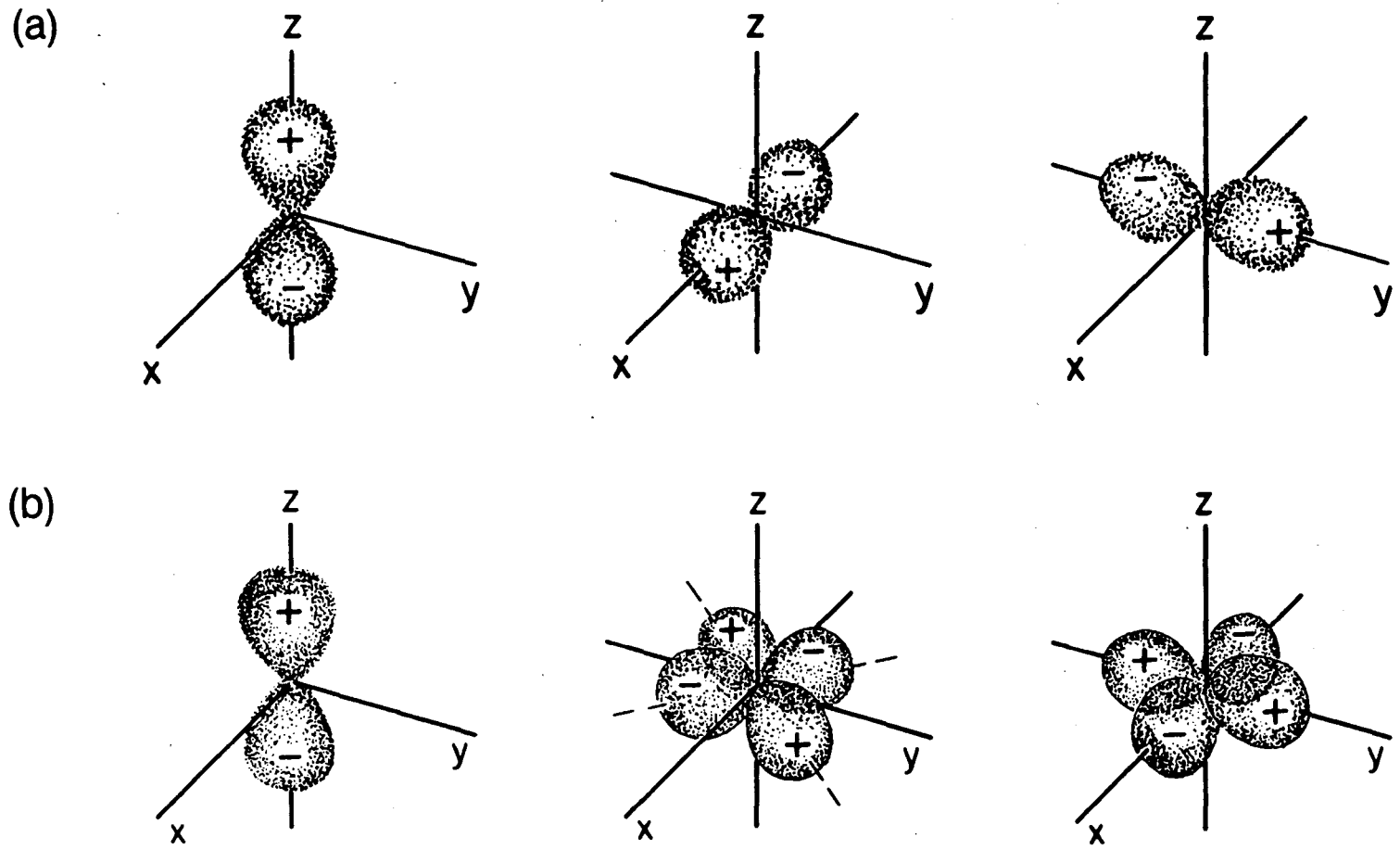

XBL 869-3398

Pines, Fermi Lectures, Figure 13

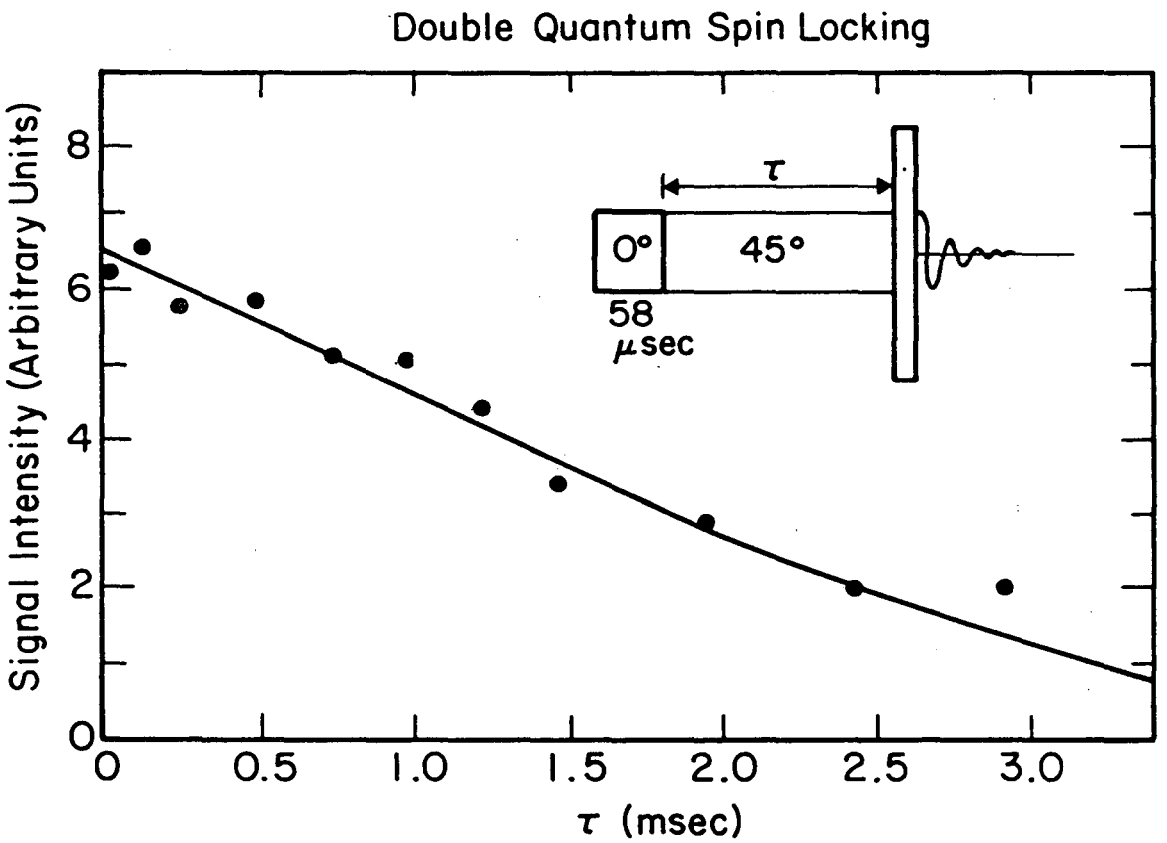

XBL 7710-6865

Pines, Fermi Lectures, Figure 14

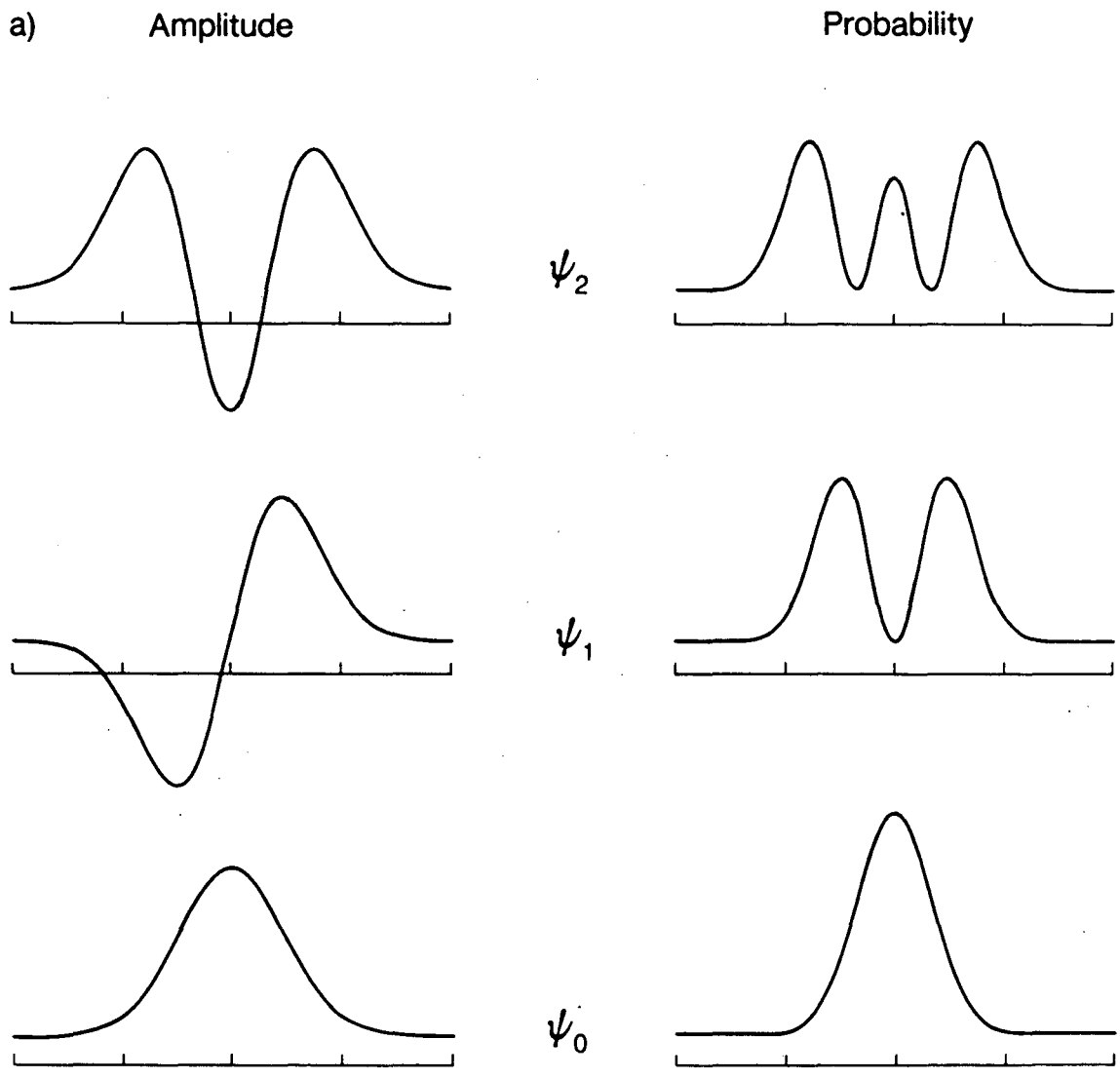

Pines, Fermi Lectures, Figure 15a

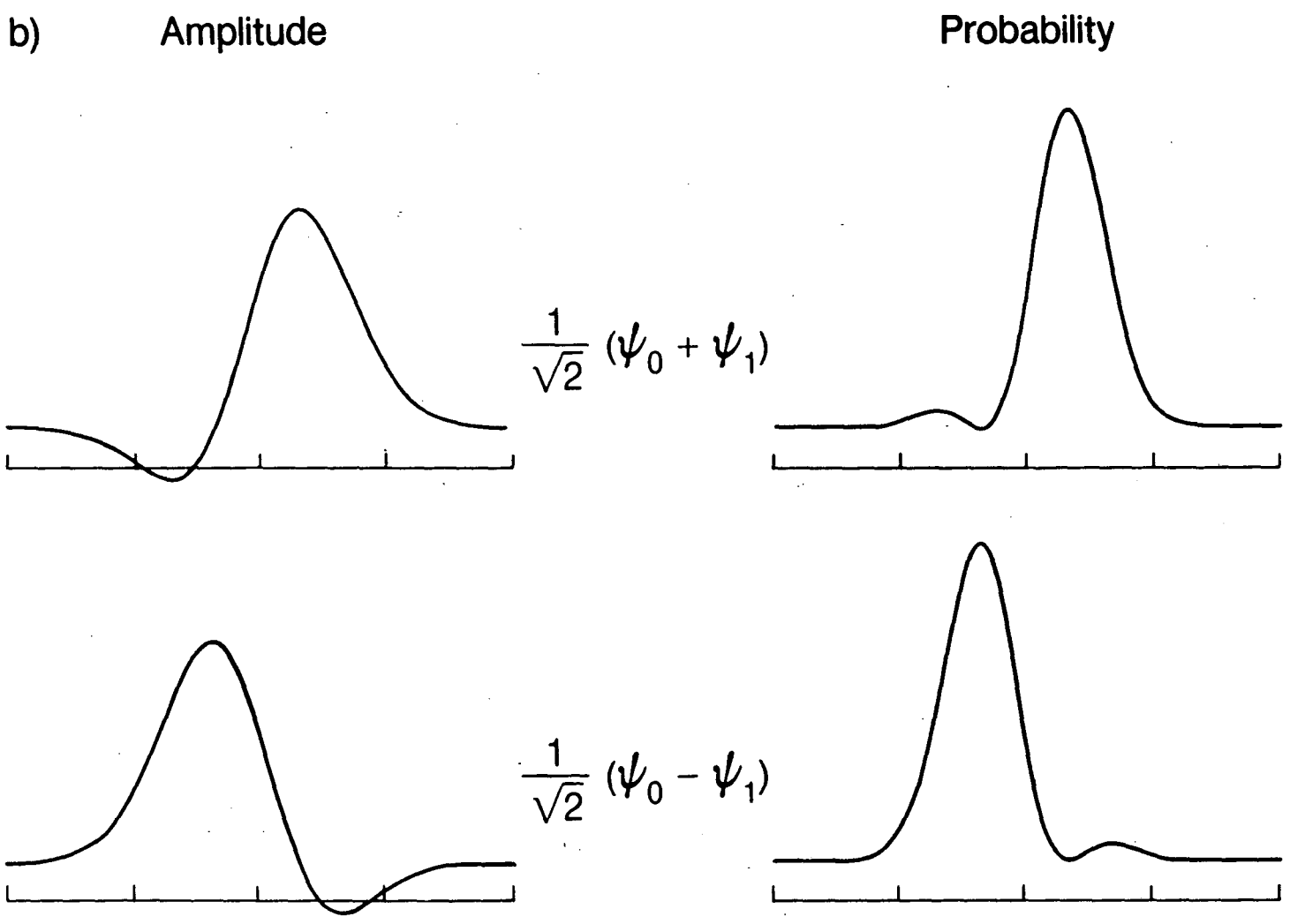

XBL 869-9901

Pines, Fermi Lectures, Figure 15b

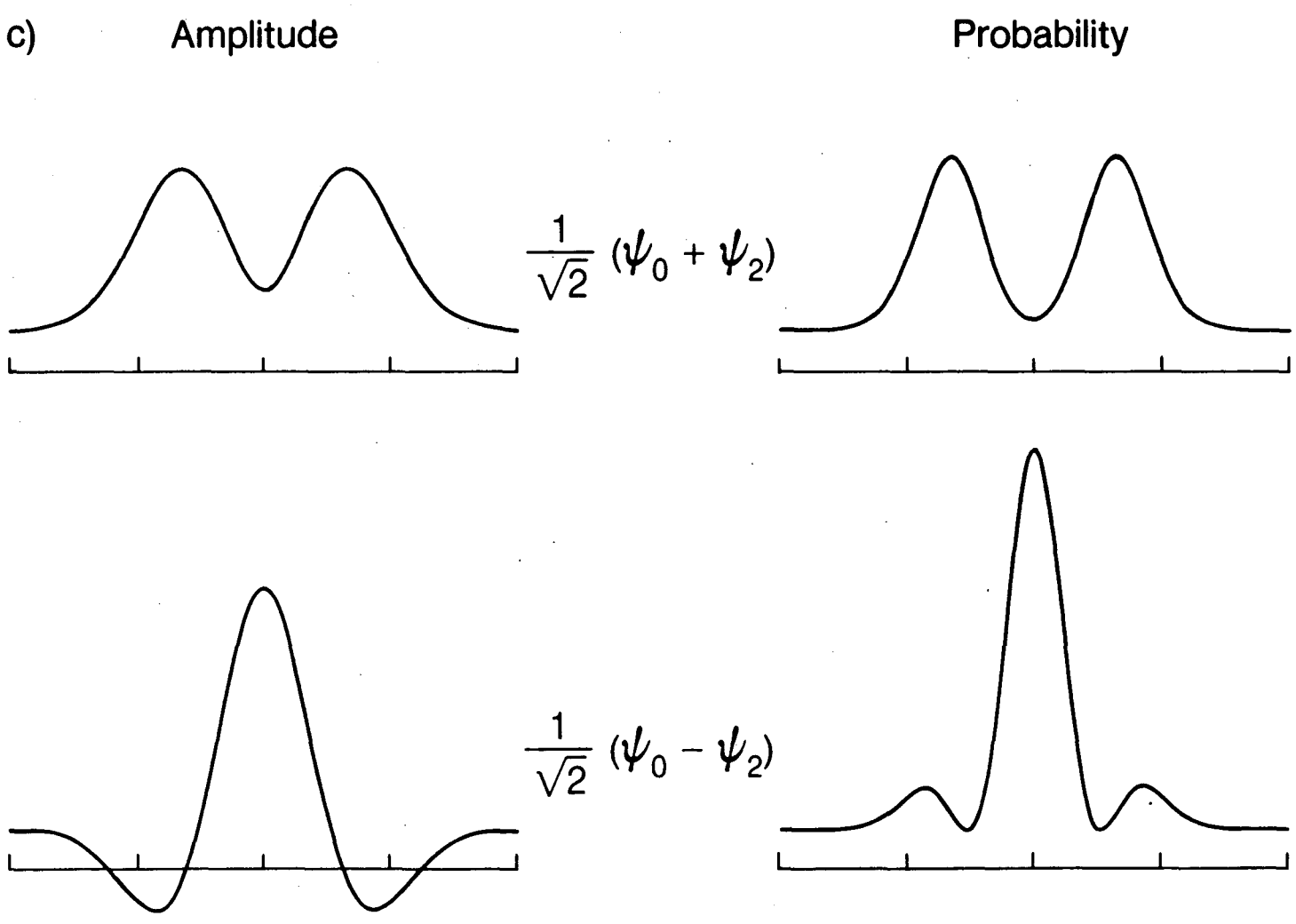

XBL 869-9902

Pines, Fermi Lectures, Figure 15c

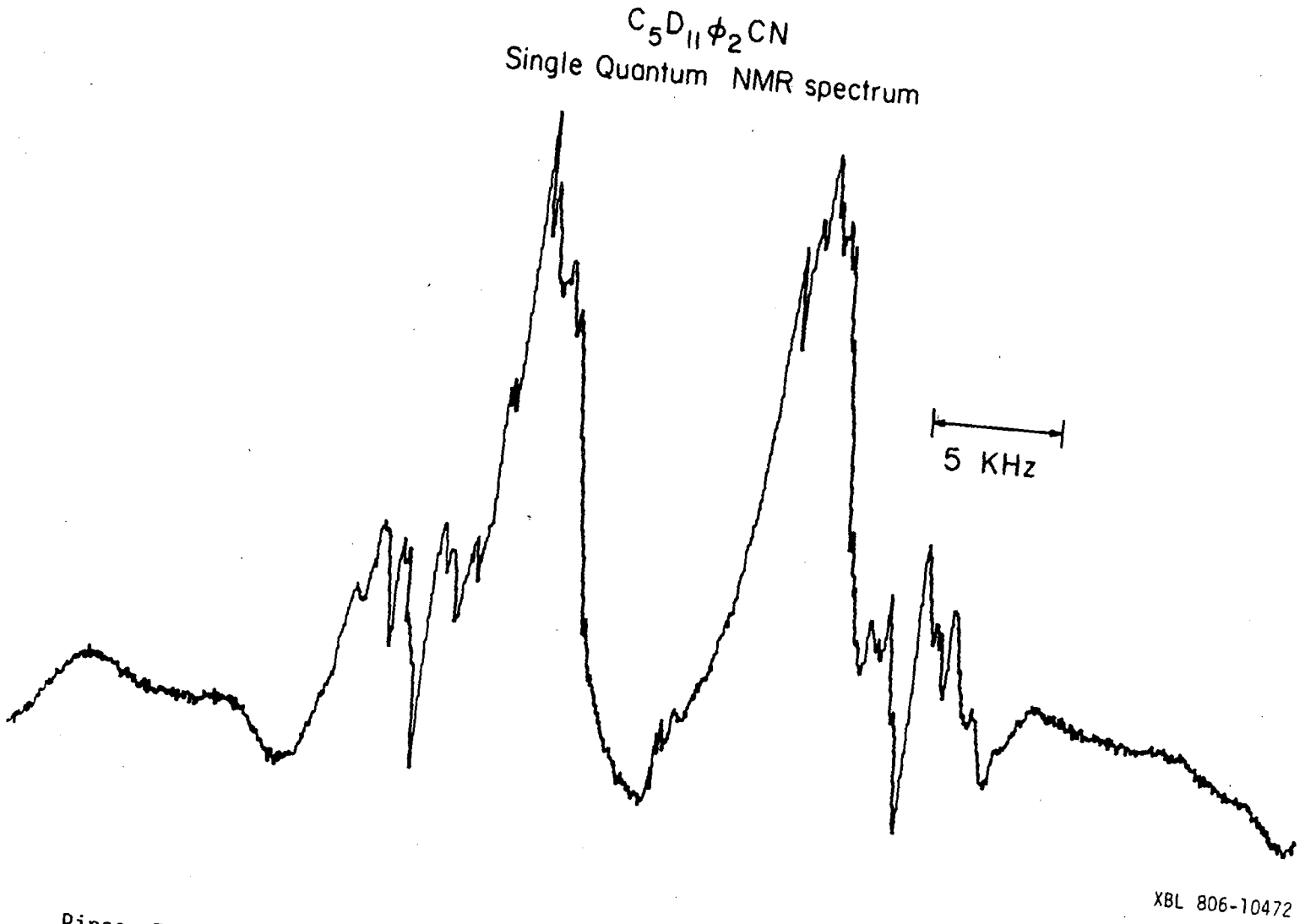

Pines, Fermi Lectures, Figure 16

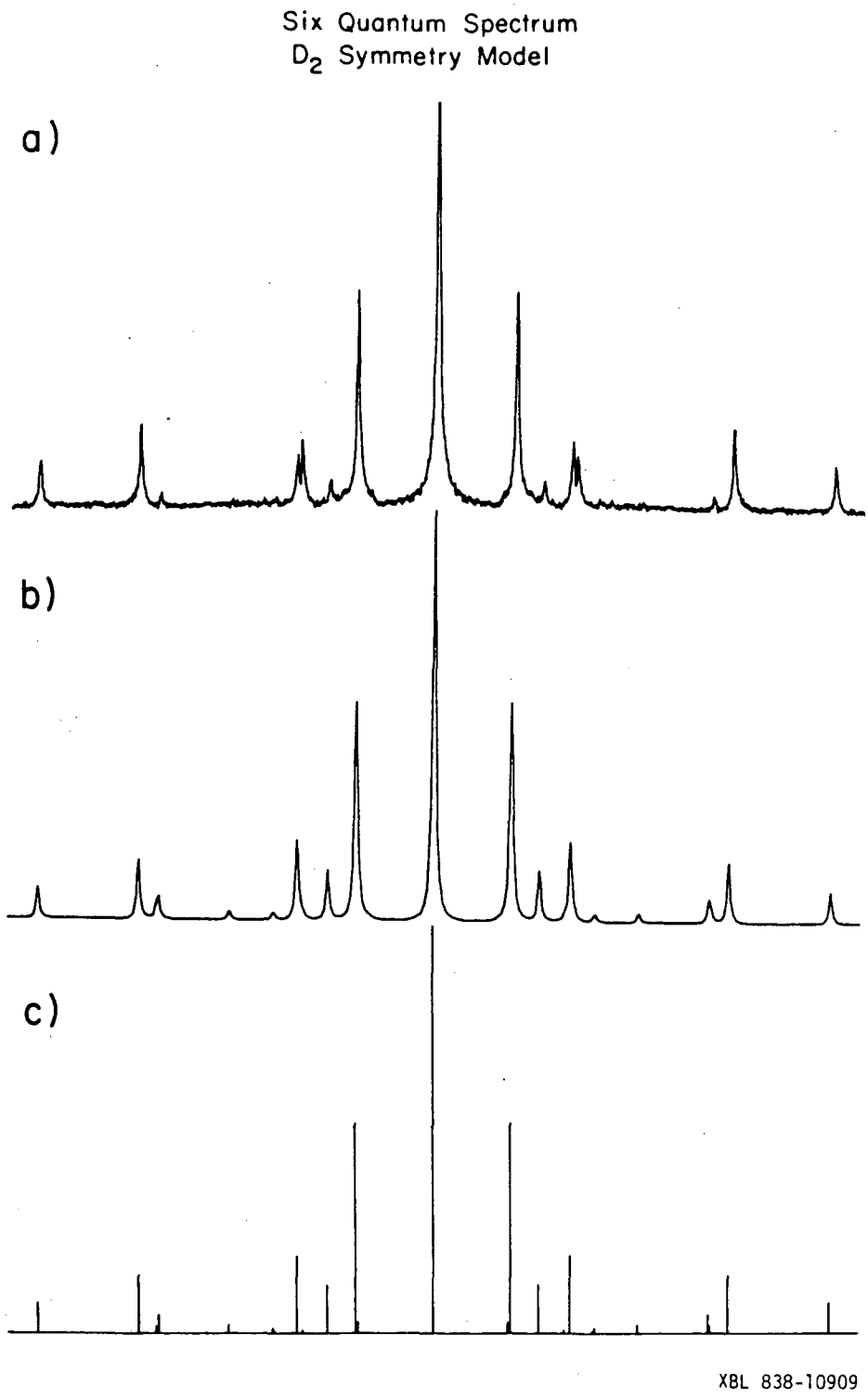

Pines, Fermi Lectures, Figure 17

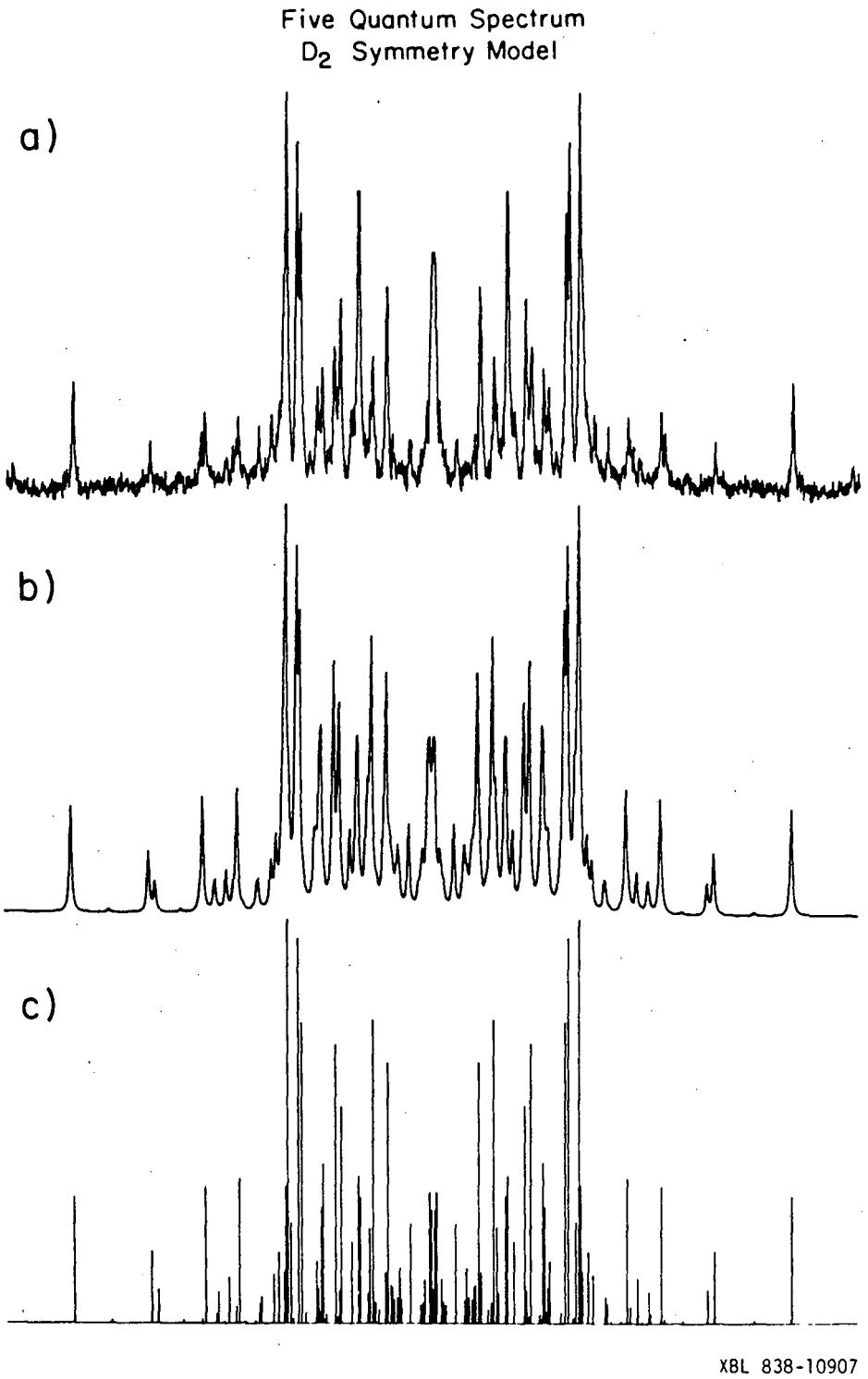

Pines, Fermi Lectures, Figure 18

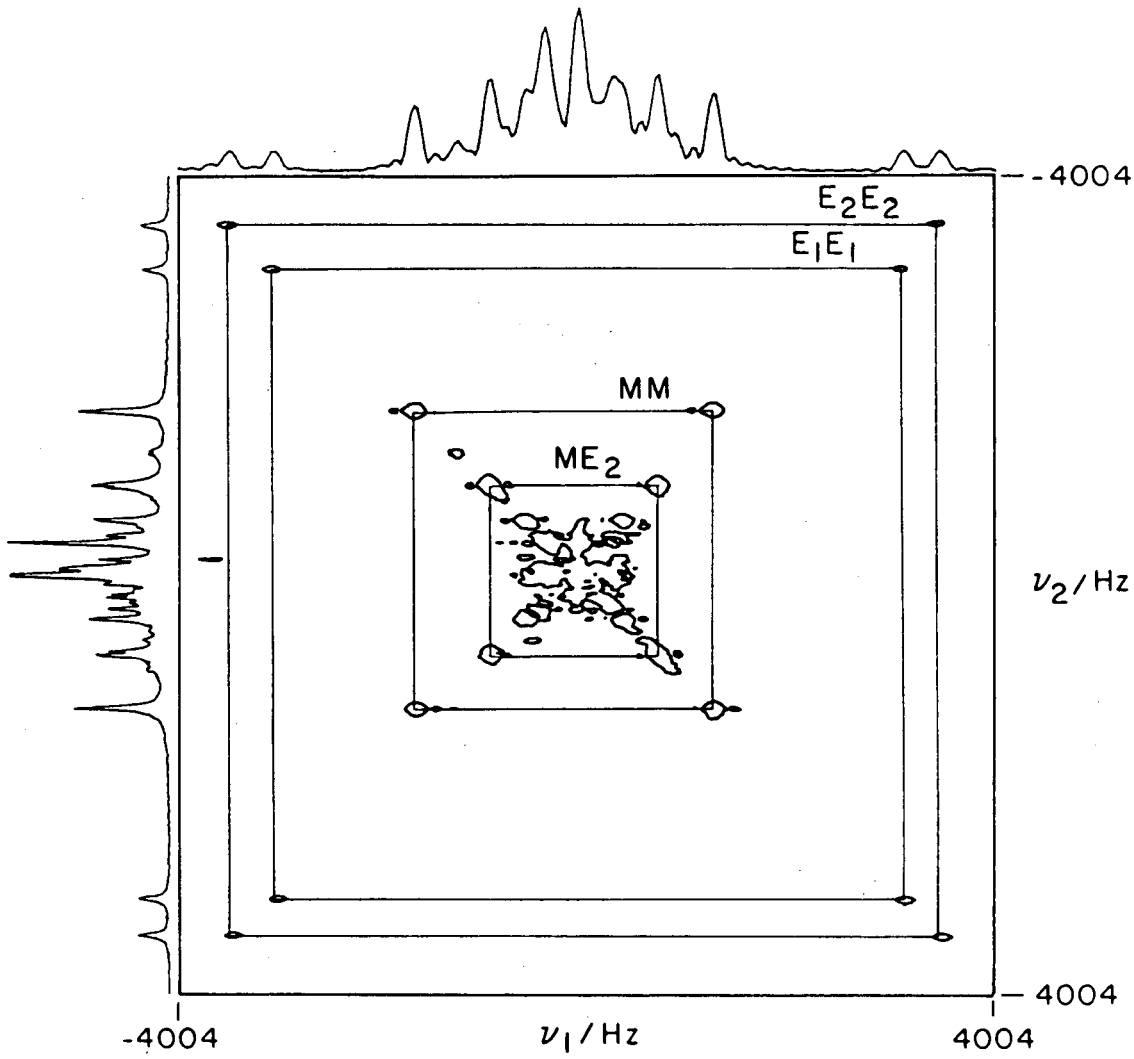

Pines, Fermi Lectures, Figure 19a

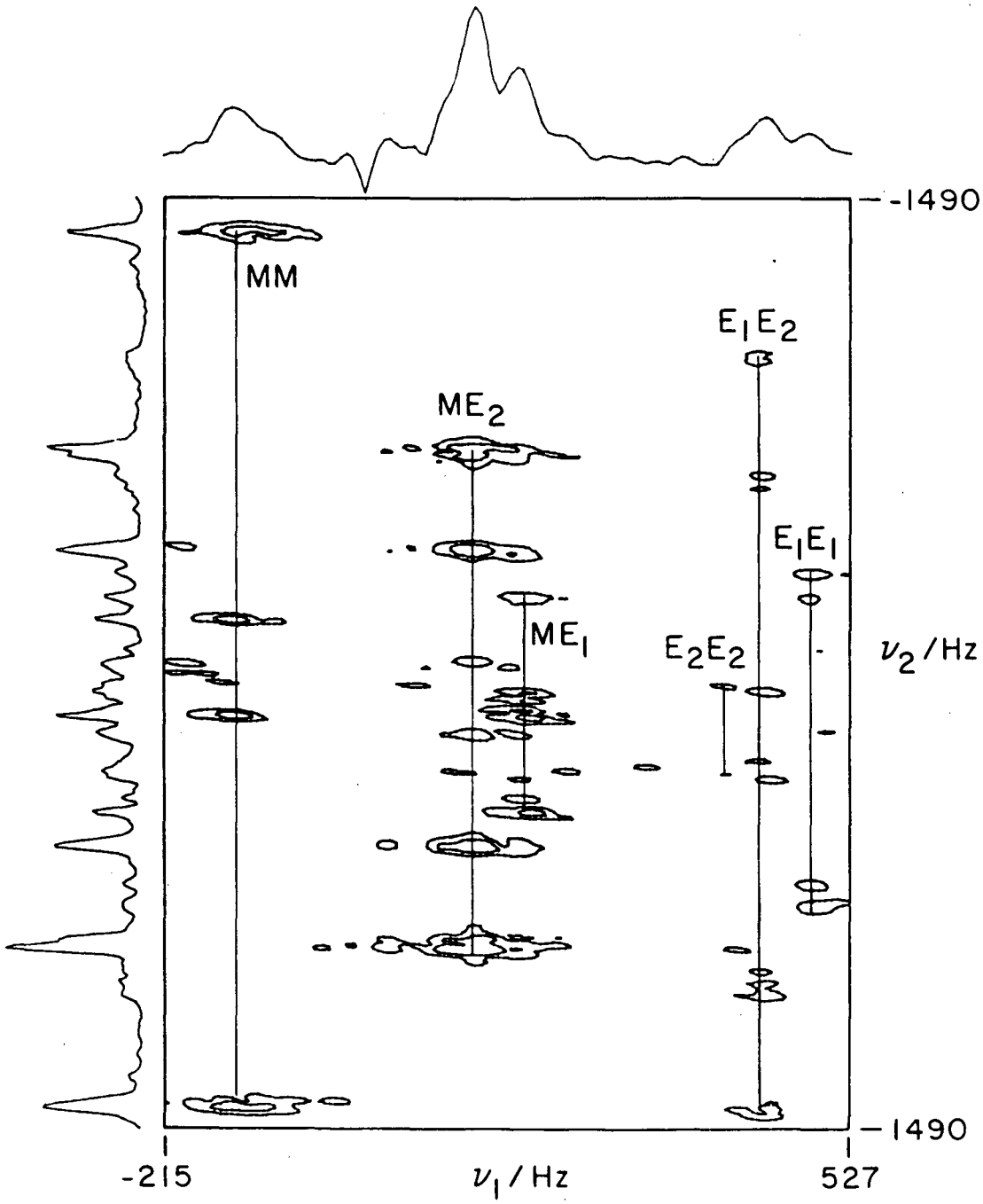

Pines, Fermi Lectures, Figure 19b

Oriented Benzene

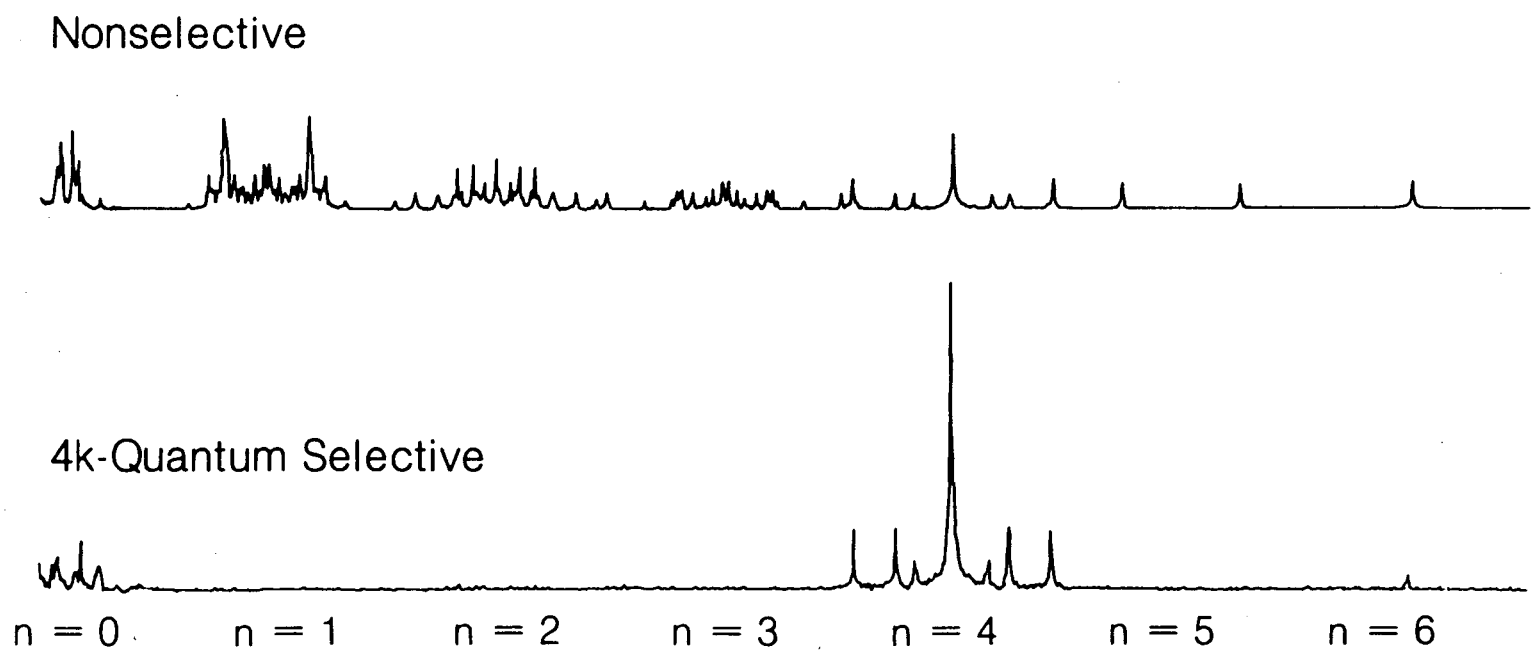

XBL 8311-4454-A

Pines, Fermi Lectures, Figure 20

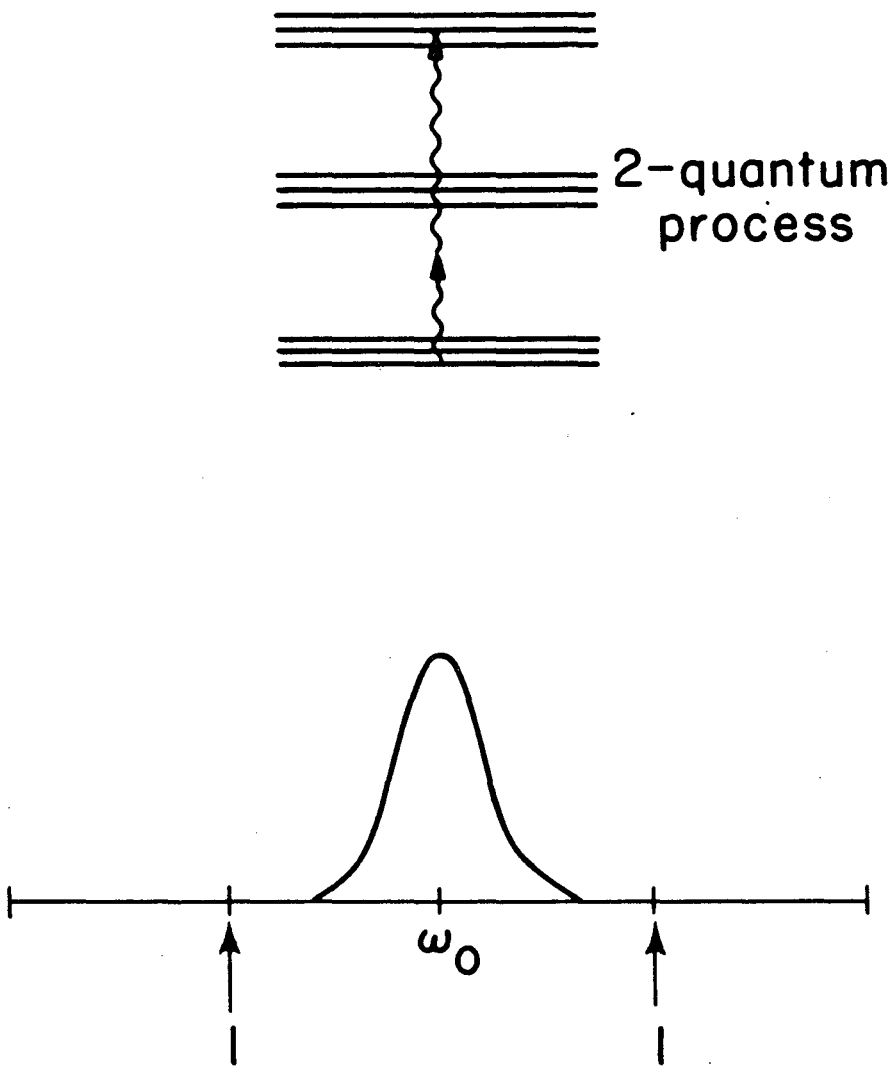

XBL 7710-6860

Pines, Fermi Lectures, Figure 21

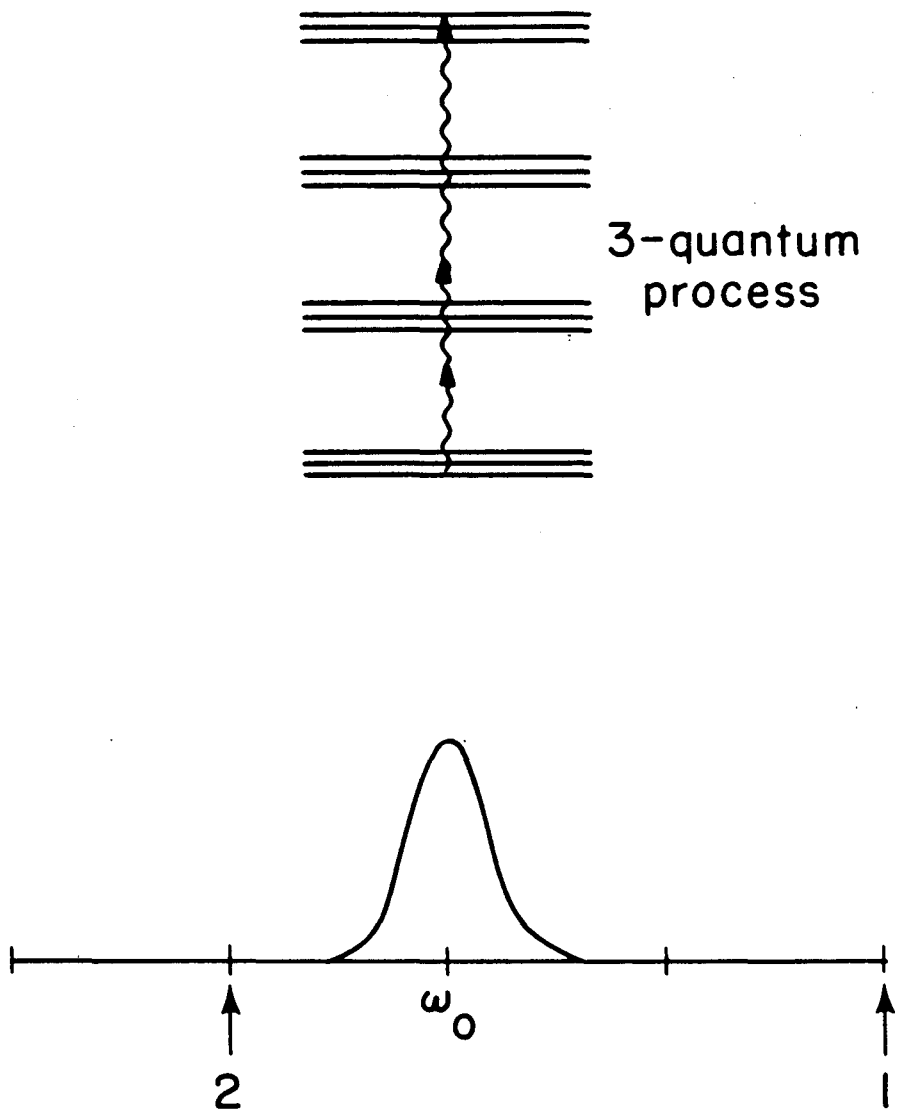

XBL 7710-10018

Pines, Fermi Lectures, Figure 22

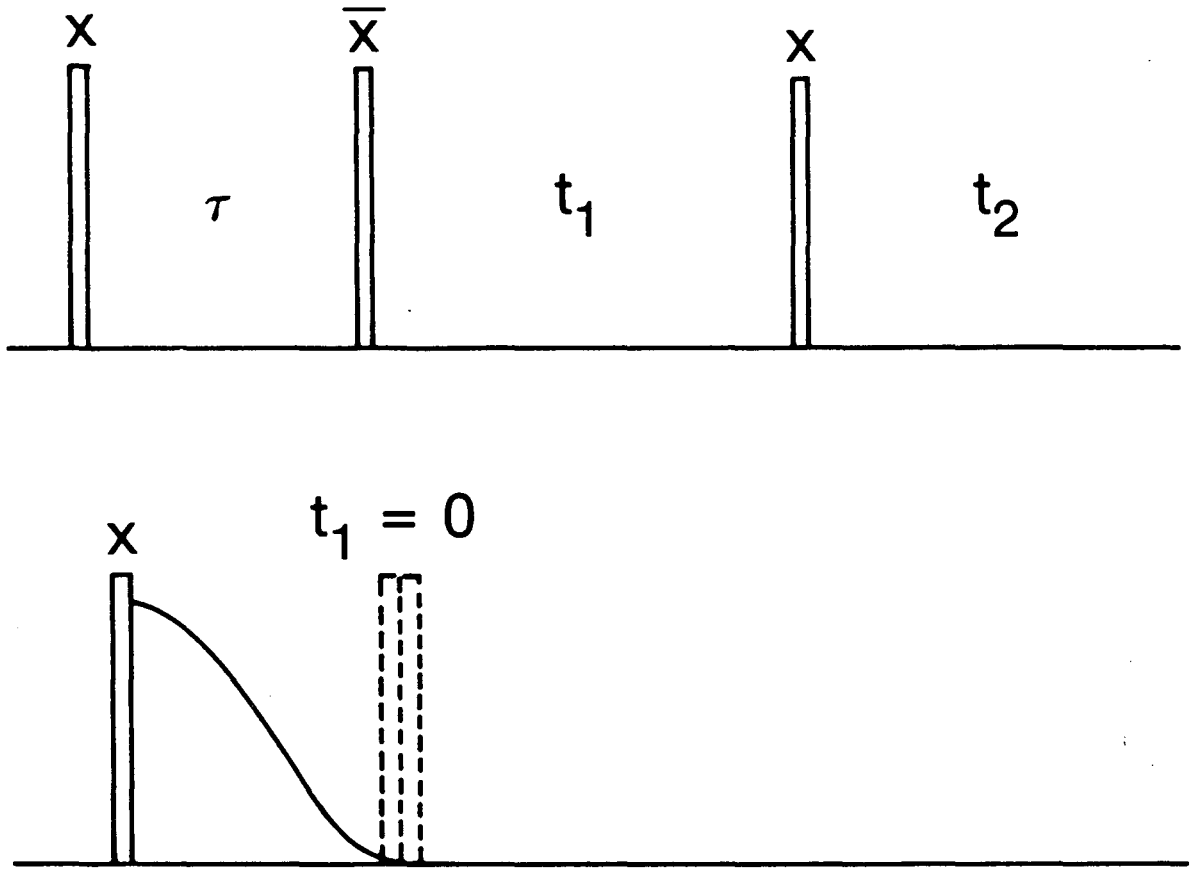

XBL 868-9465

Pines, Fermi Lectures, Figure 23

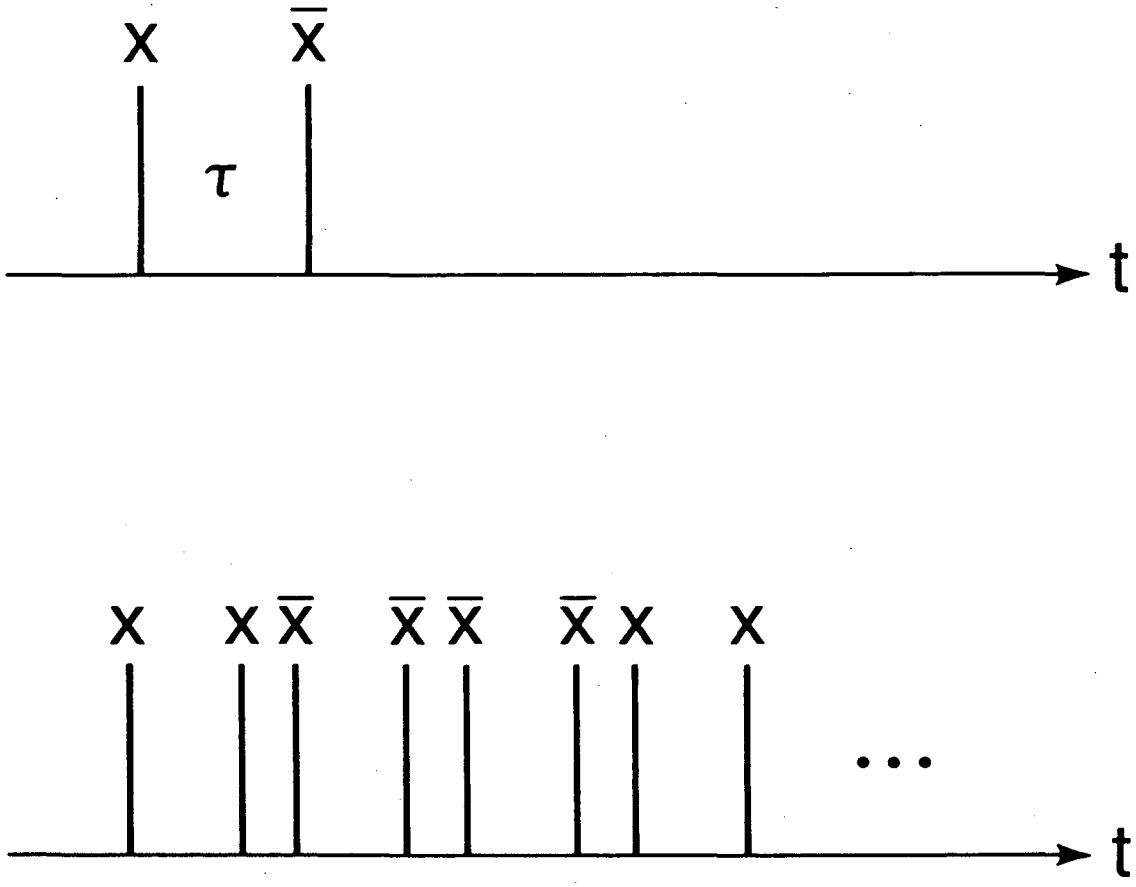

XBL-866-6345

Pines, Fermi Lectures, Figure 24

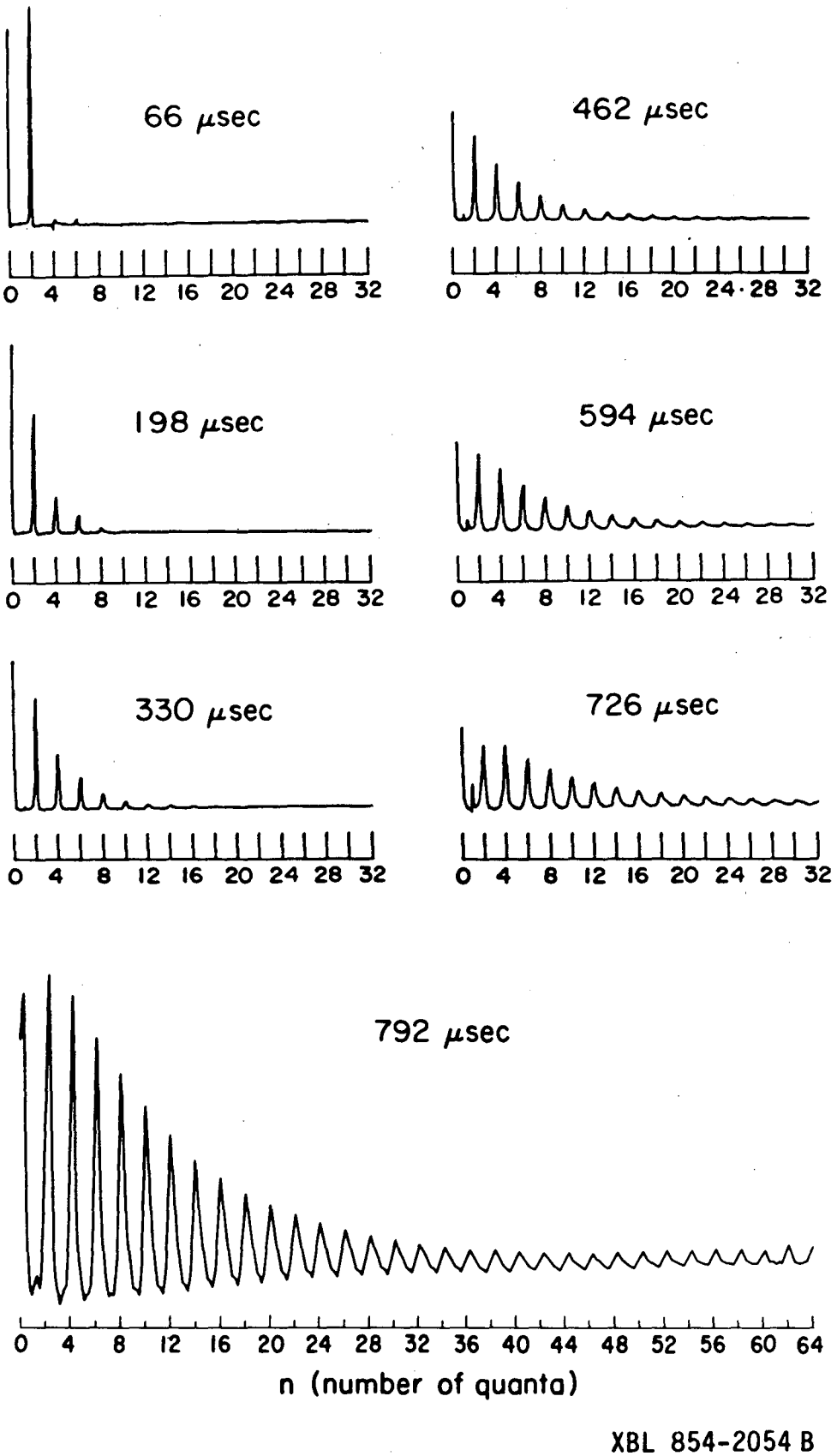

Pines, fermi Lectures, Figure 25

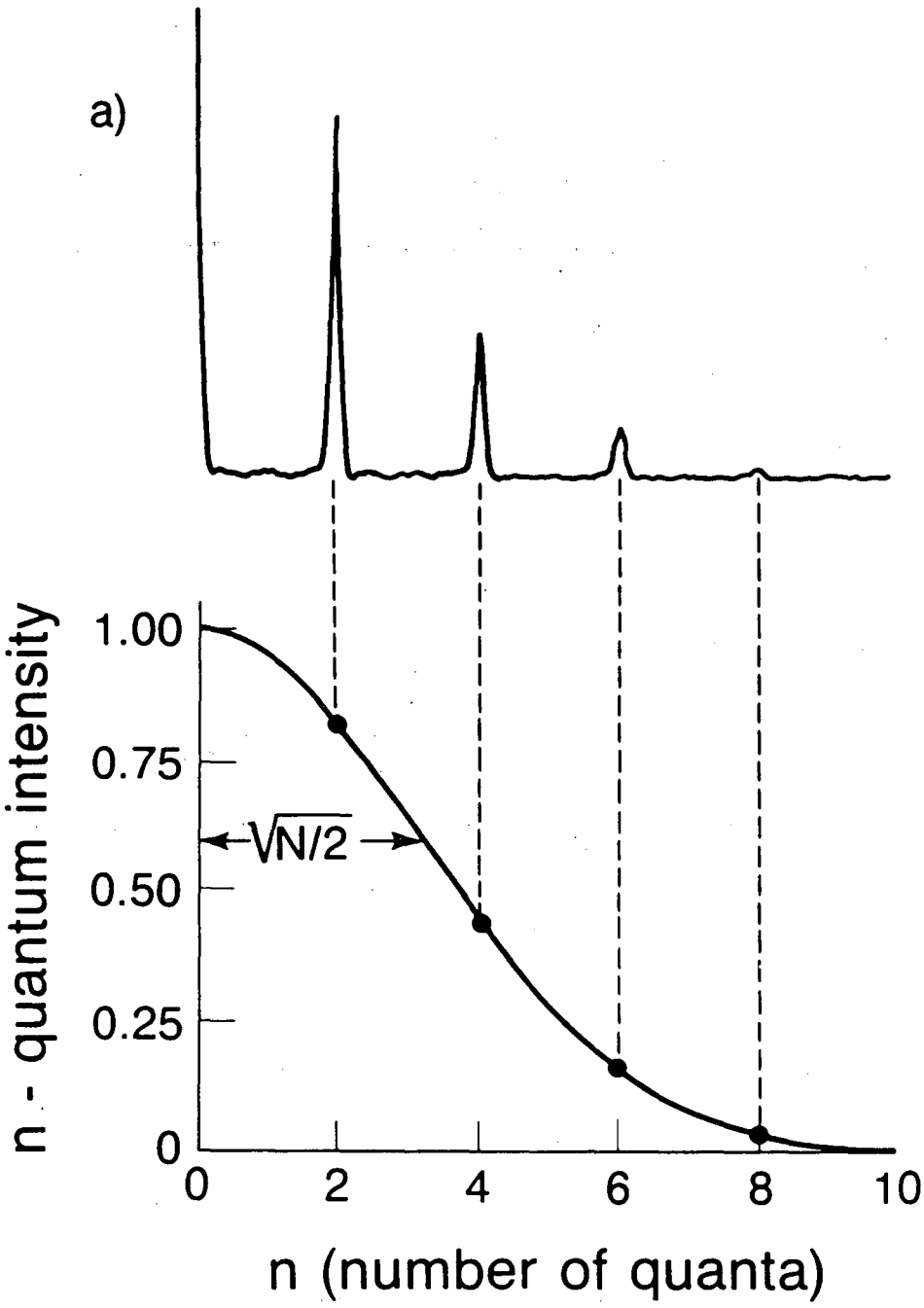

XBL 8511-12714A

Pines, Fermi Lectures, Figure 26a

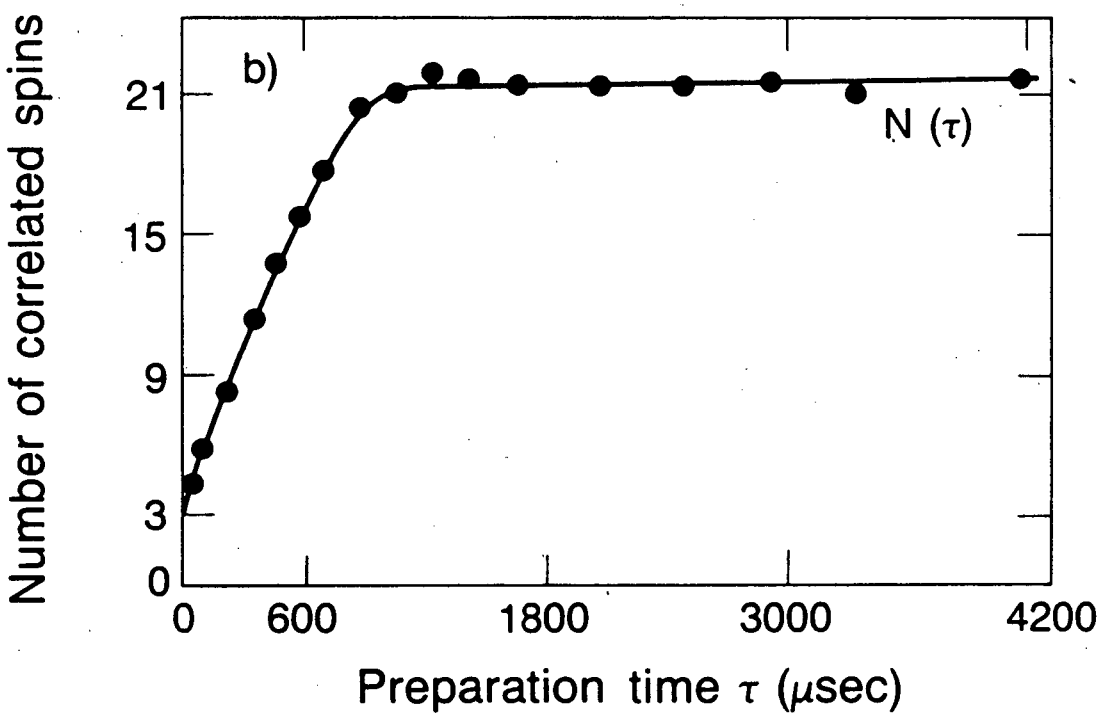

XBL 8512-12777 A

Pines, Fermi Lectures, Figure 26b

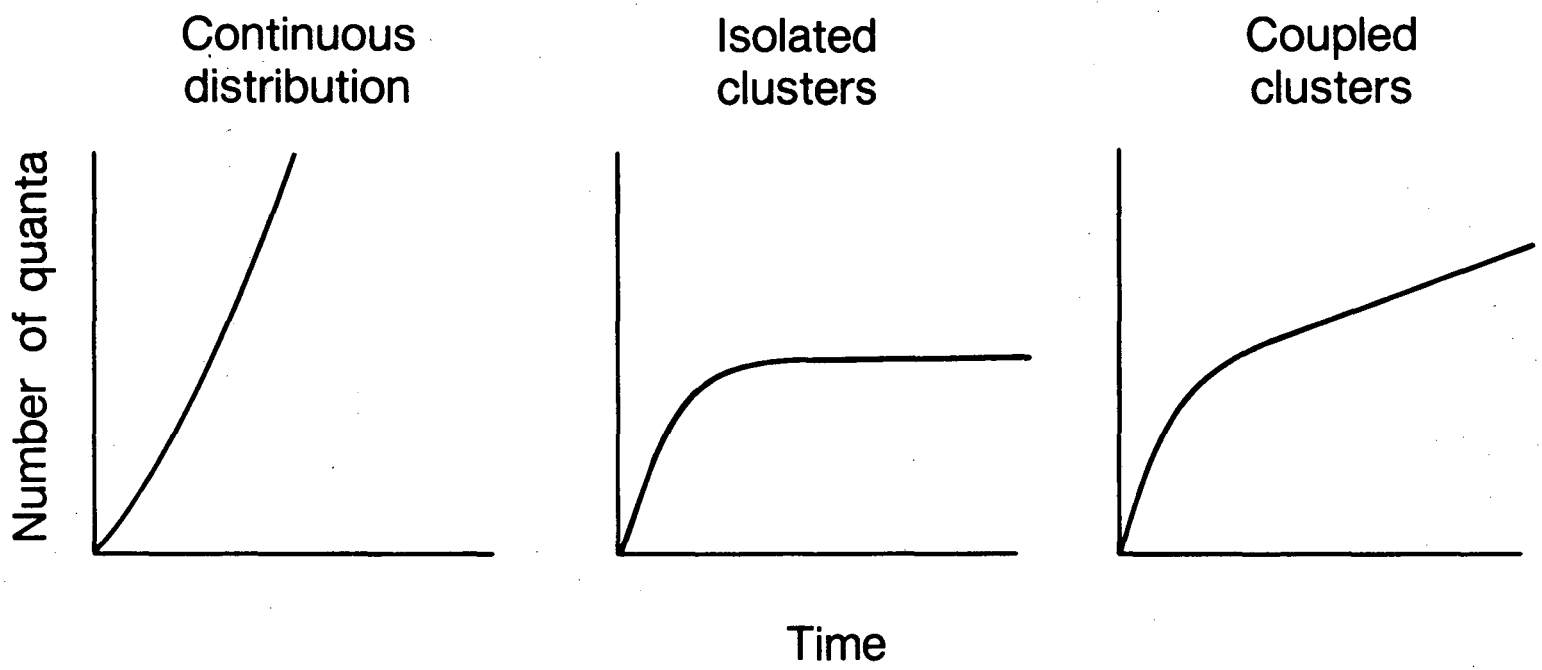

XBL 869-9631

Pines, Fermi Lectures, Figure 27

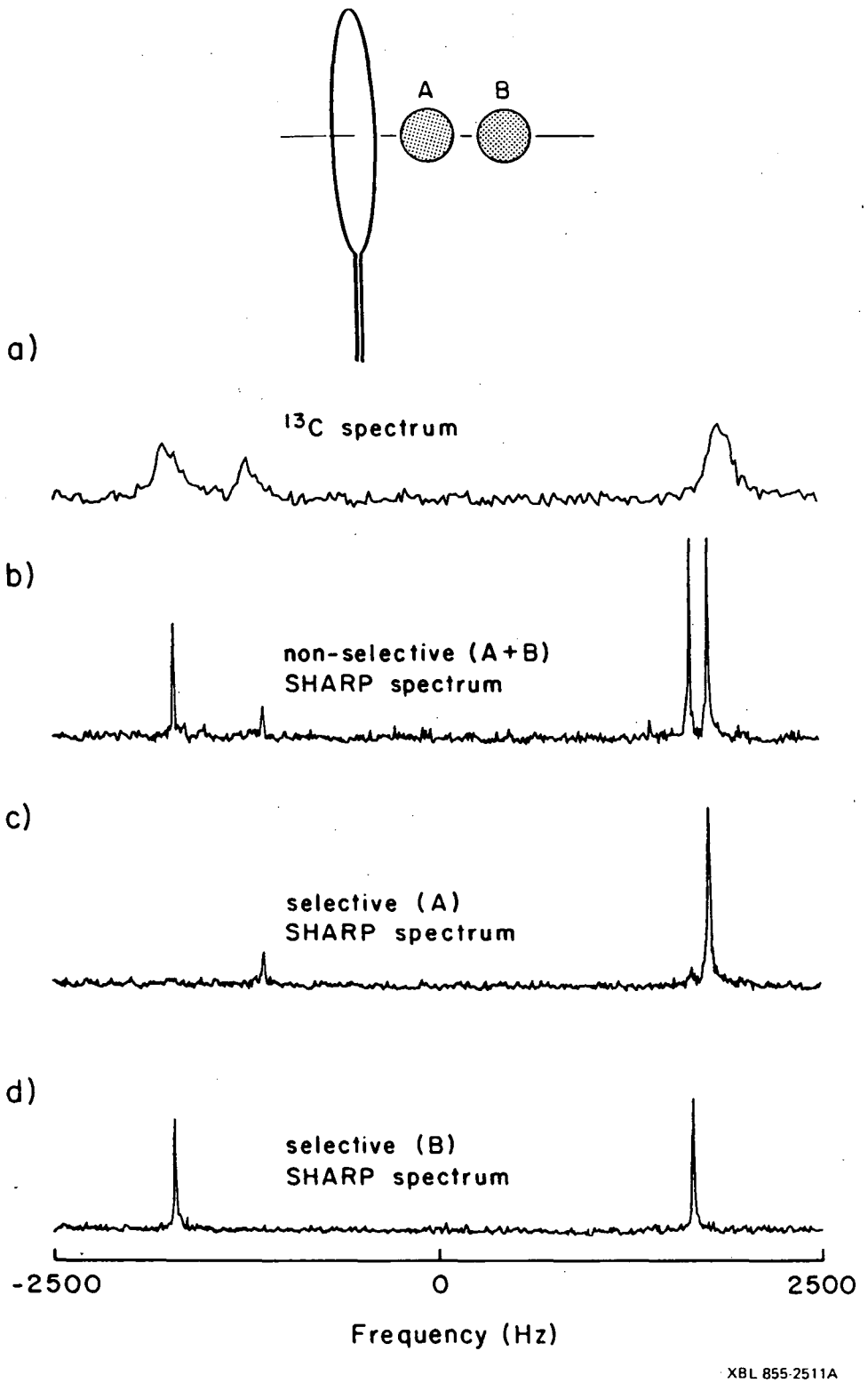

Pines, Fermi Lectures, Figure 28

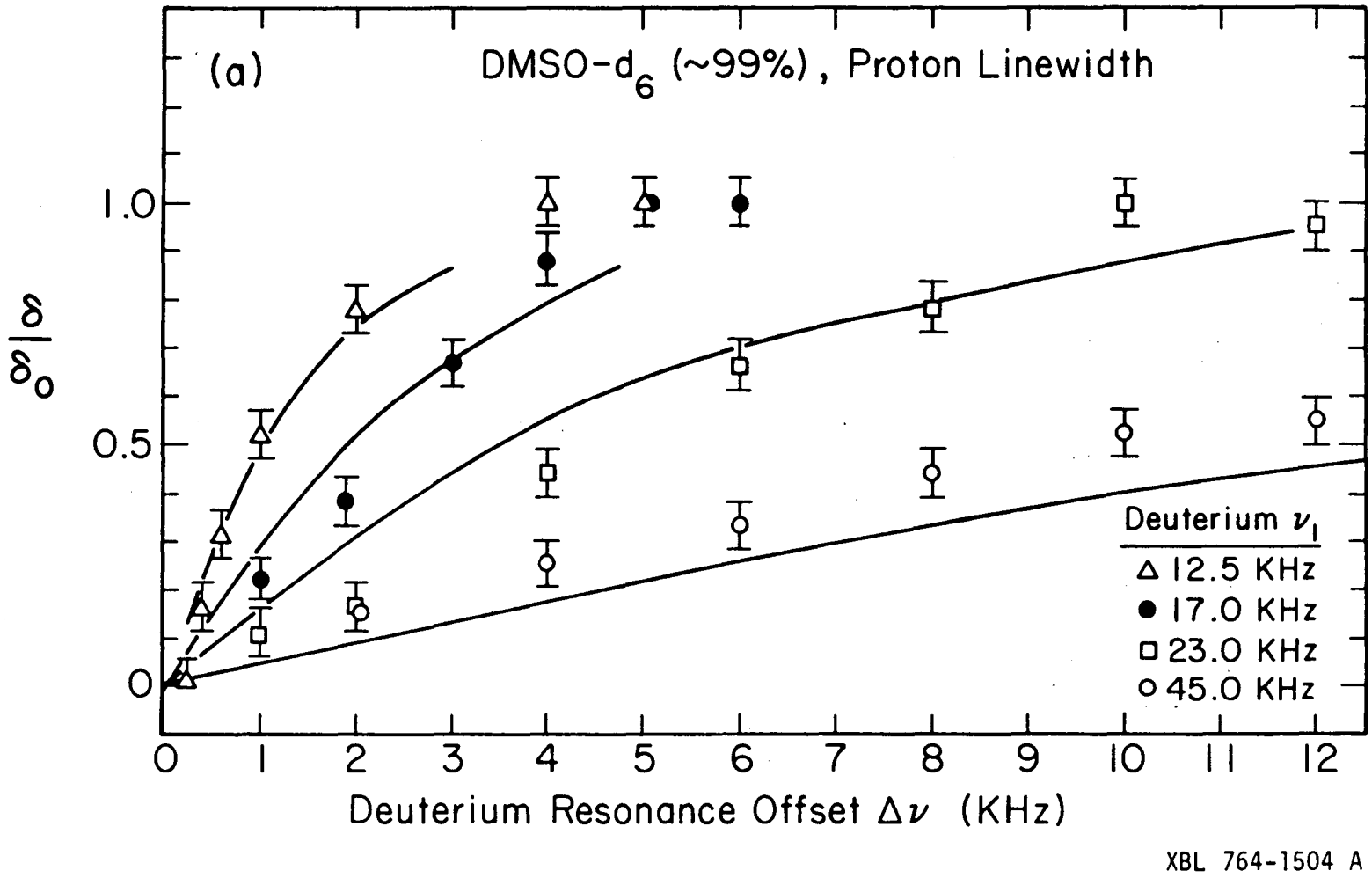

XBL 764-1504 A

Pines, Fermi Lectures, Figure 29a

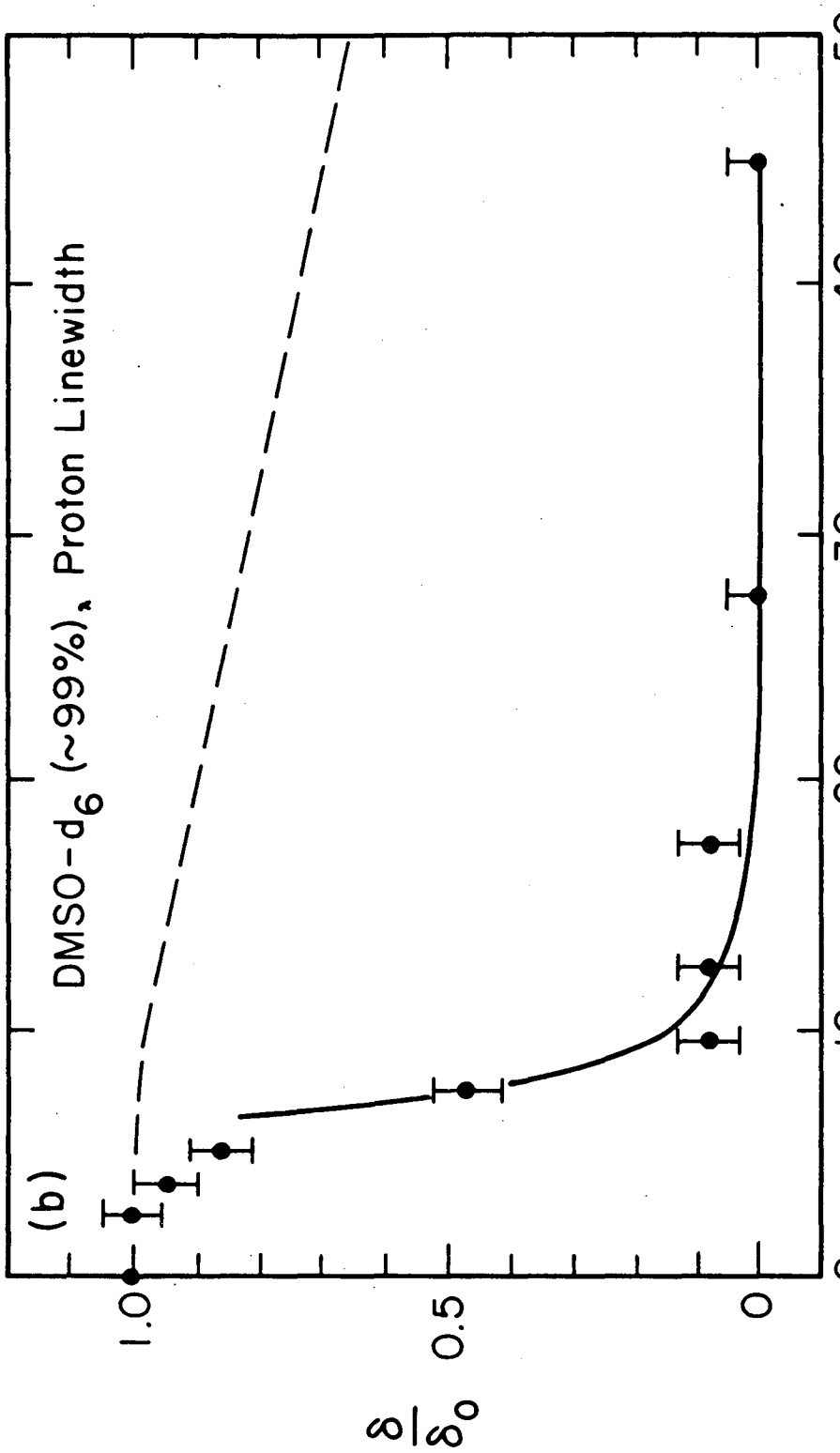

XBL 764-1523A

Pines, Fermi Lectures, Figure 29b

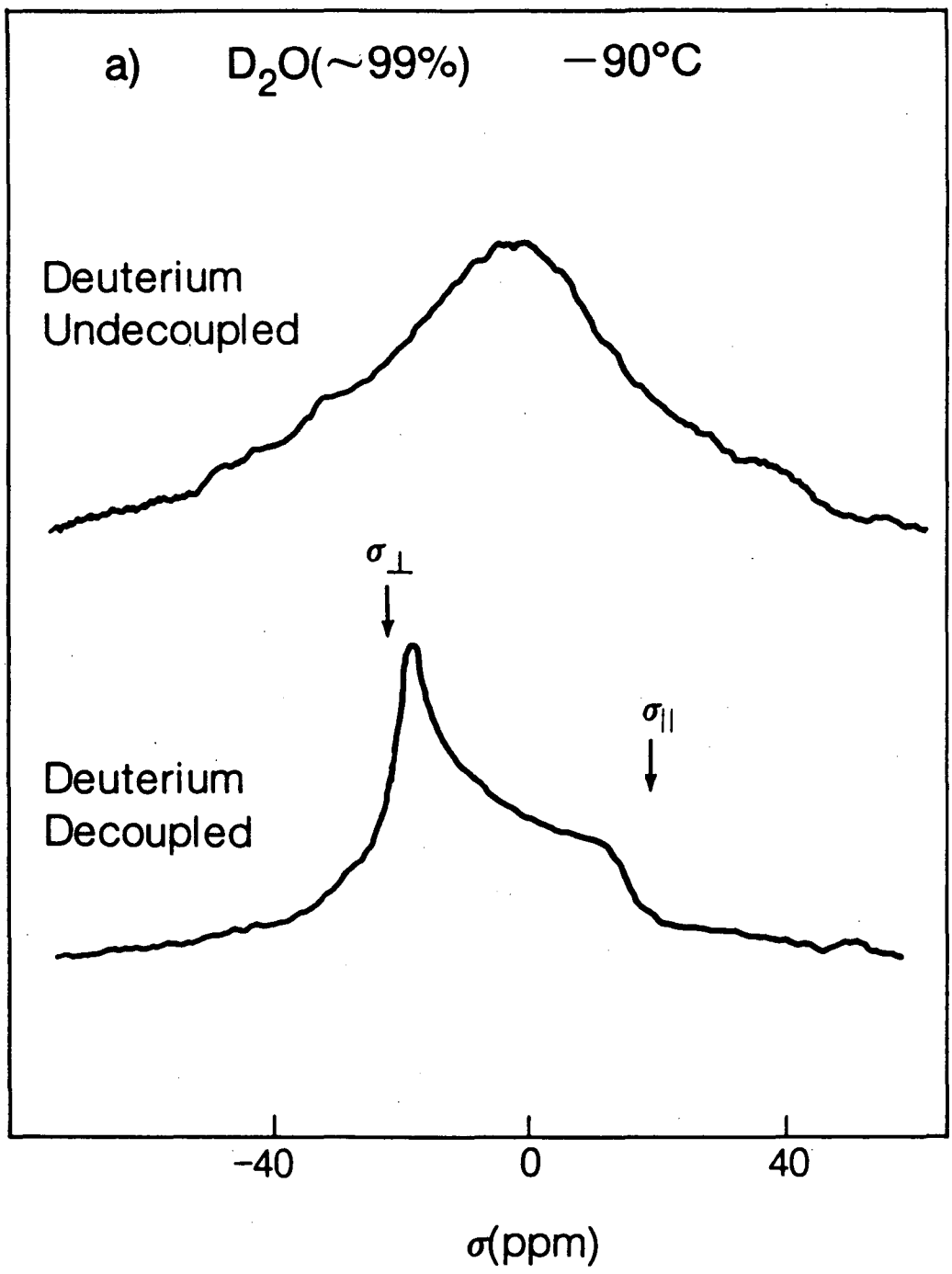

XBL 8312-6850A

Pines, Fermi Lectures, Figure 30a

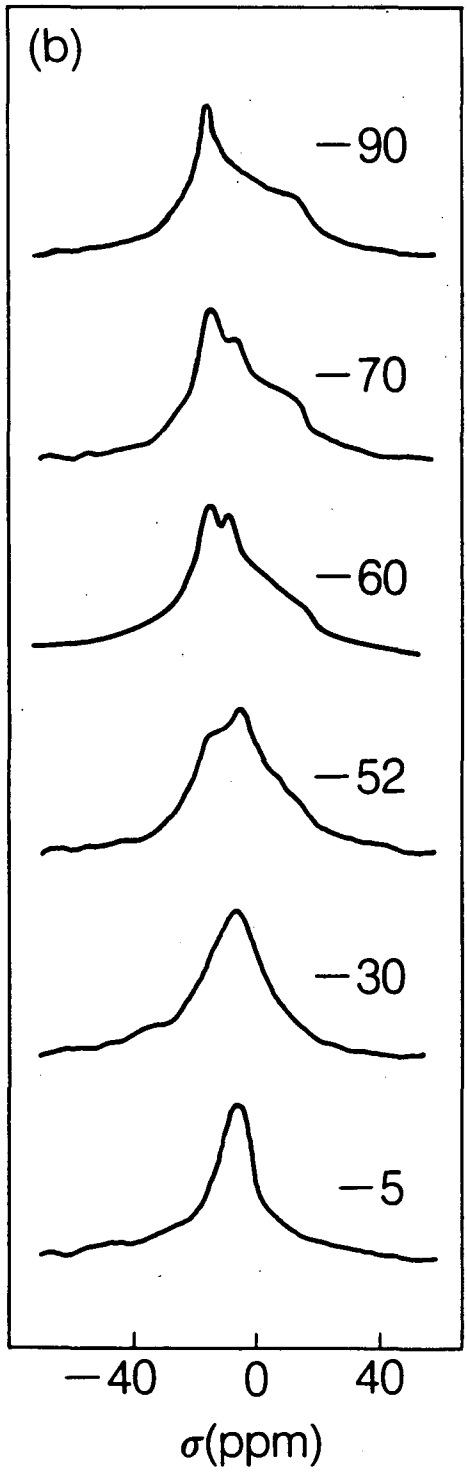

Pines, Fermi Lectures, Figure 30b

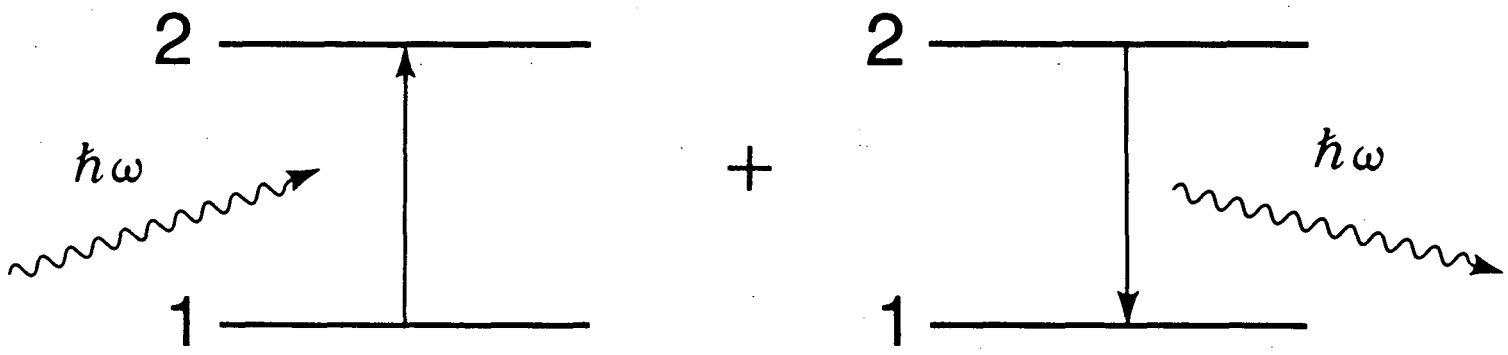

XBL 866-6327 A

Pines, Fermi Lectures, Figure 31

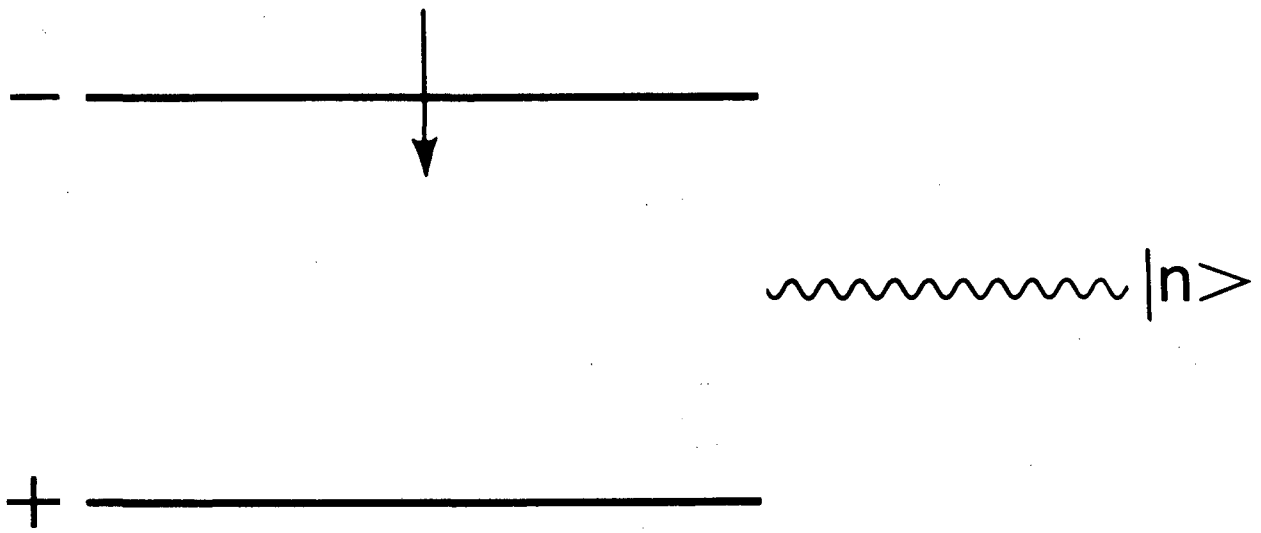

XBL 866-6322 A

Pines, Fermi Lectures, Figure 32

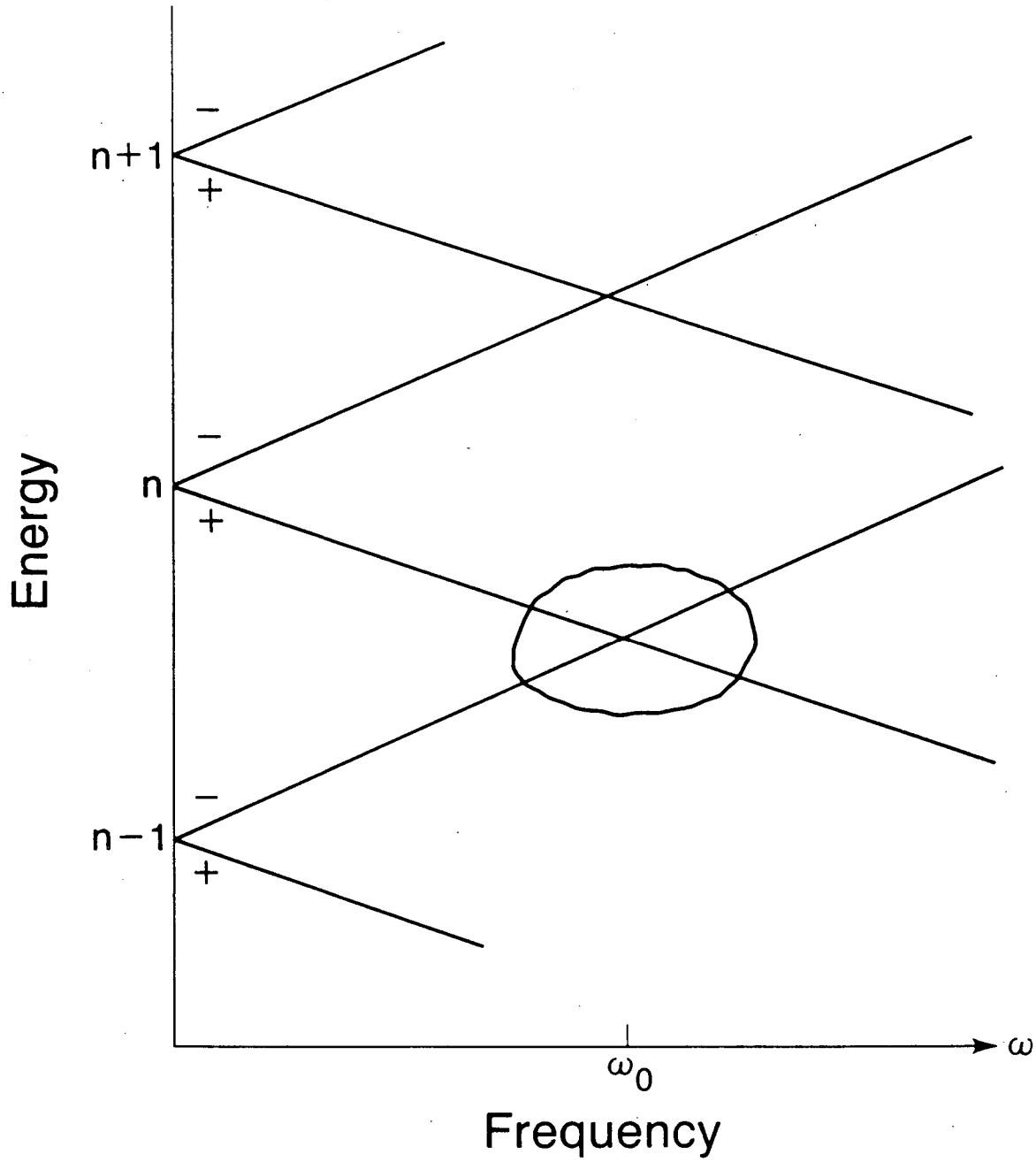

Pines, Fermi Lectures, Figure 33

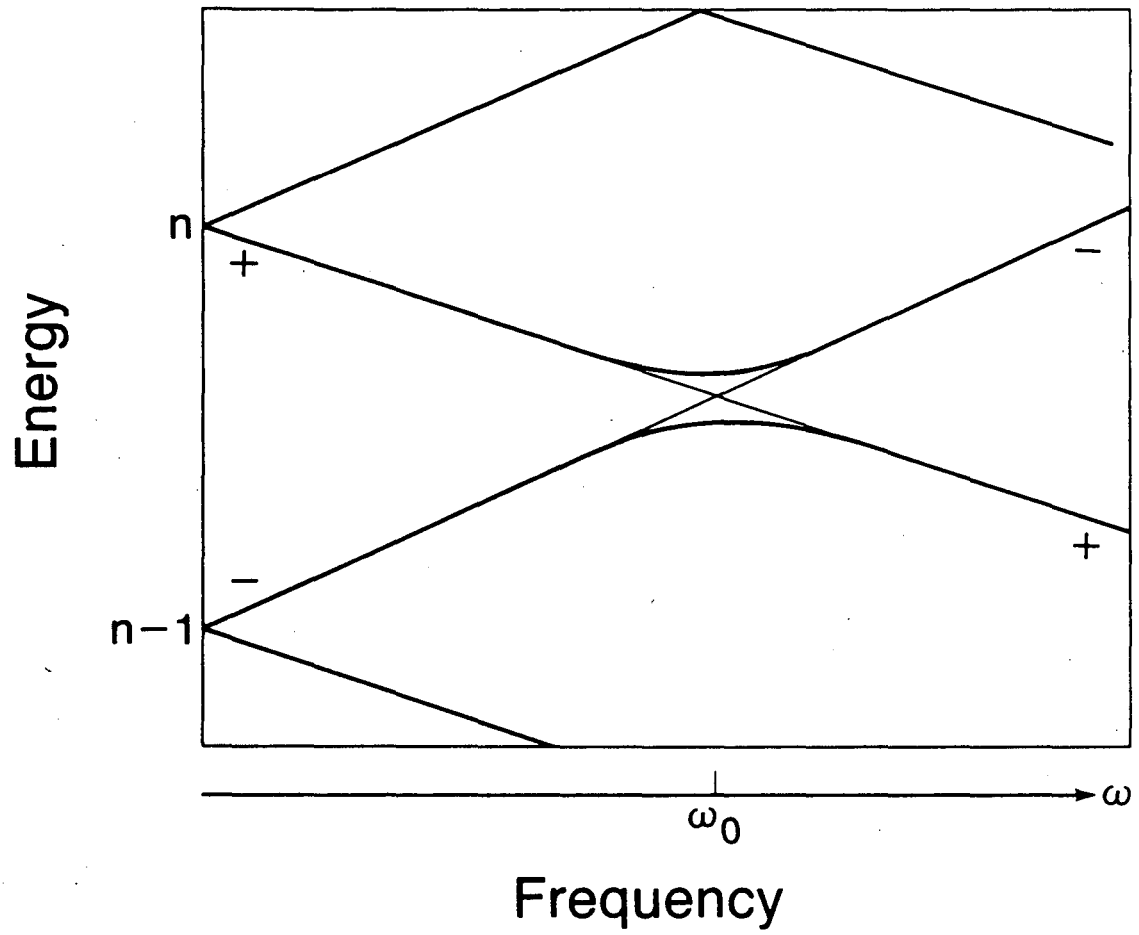

XBL 866-6314 A

Pines, Fermi Lectures, Figure 34

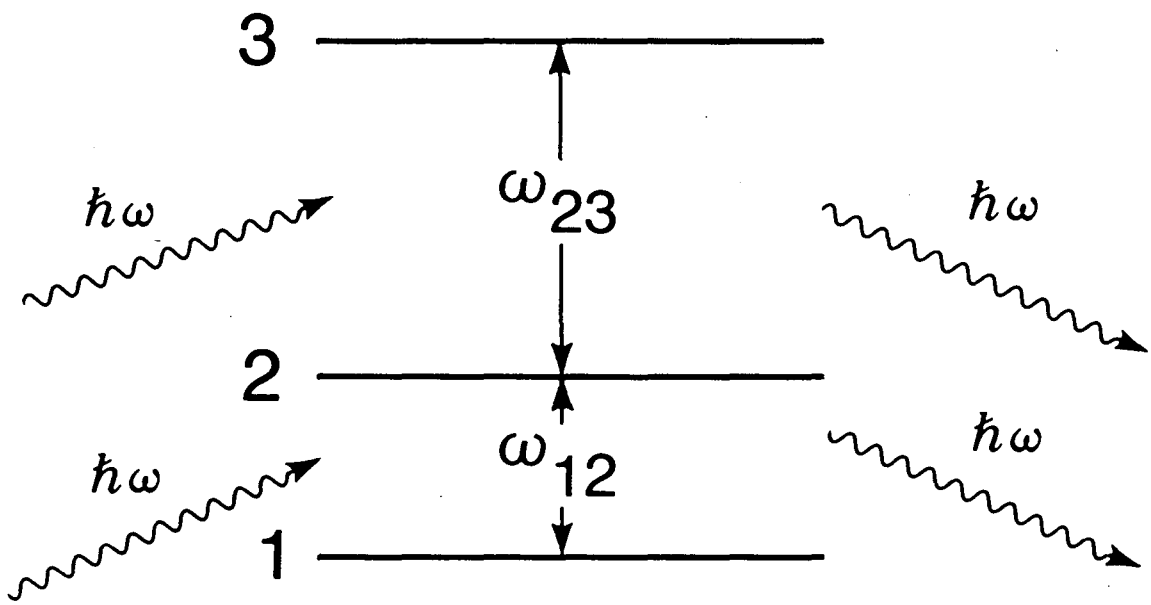

XBL 866-6320 A

P nes, Fermi Lectures, Figure 35a

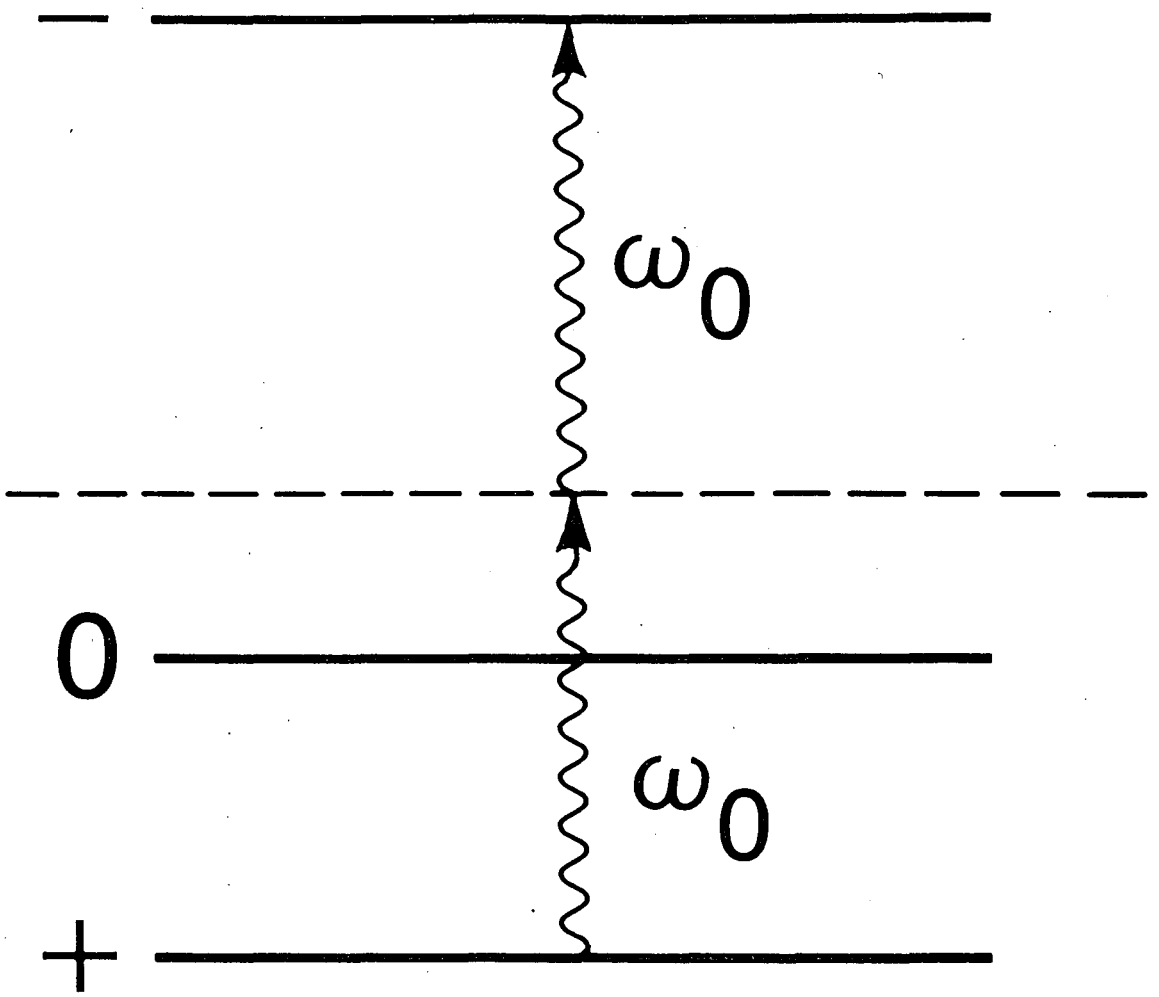

XBL 866-6316 A

Pines, Fermi Lectures, Figure 35b

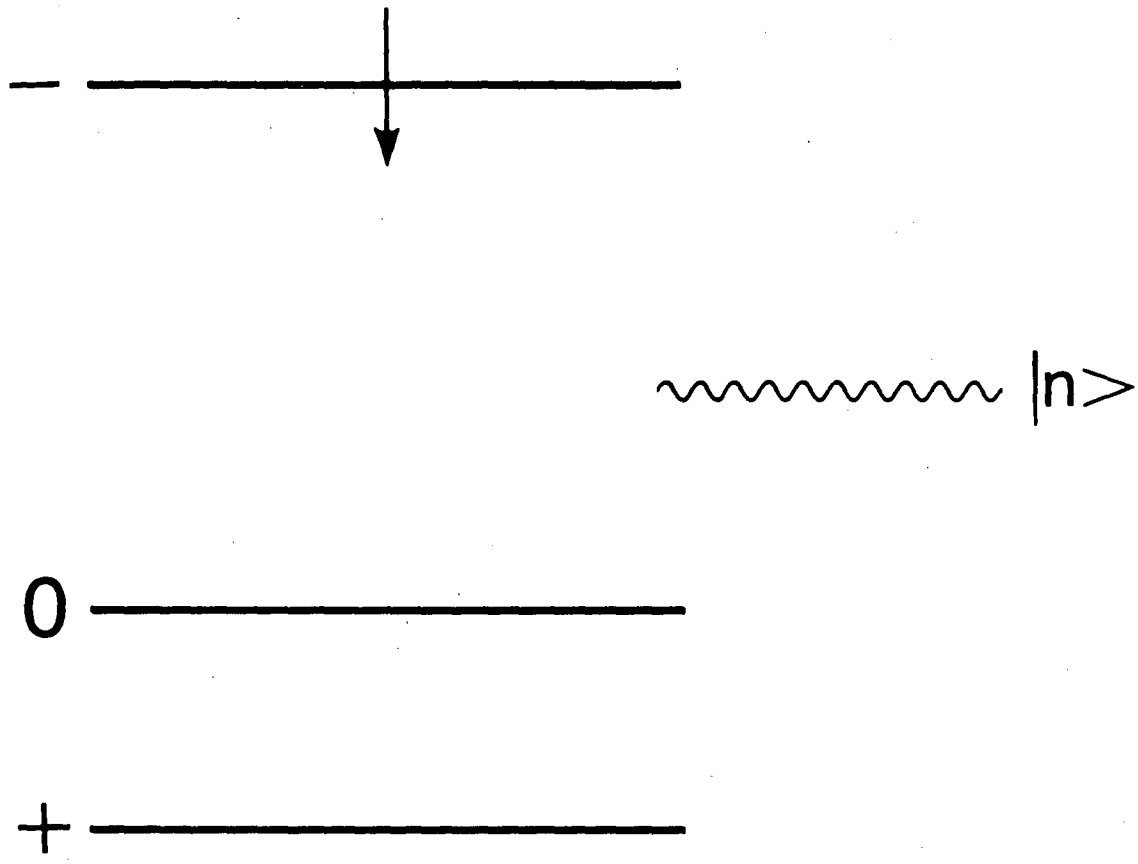

XBL 866-6319 A

Pines, Fermi Lectures, Figure 36

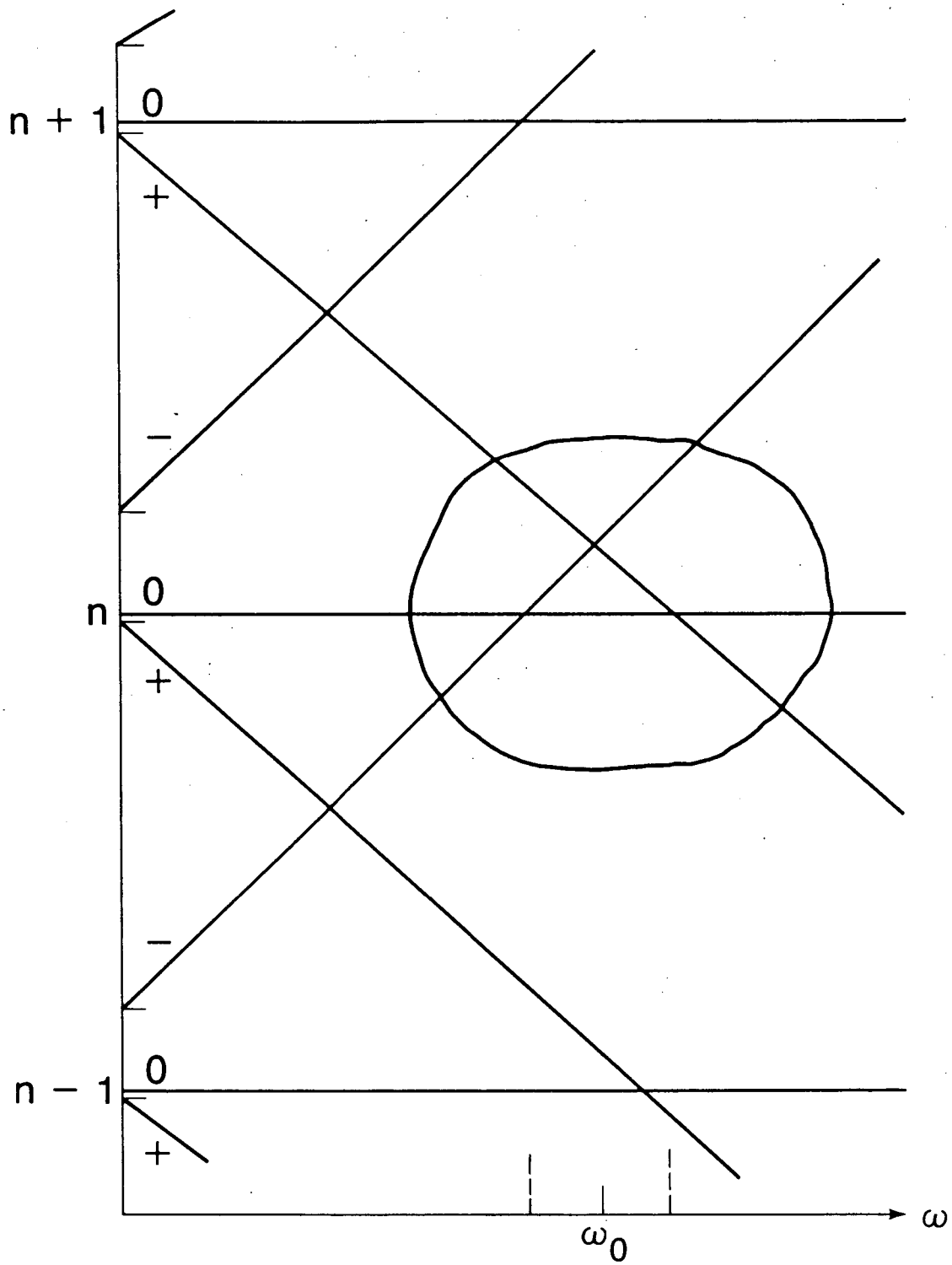

XBL 866-6309 A

Pines, Fermi Lectures, Figure 37

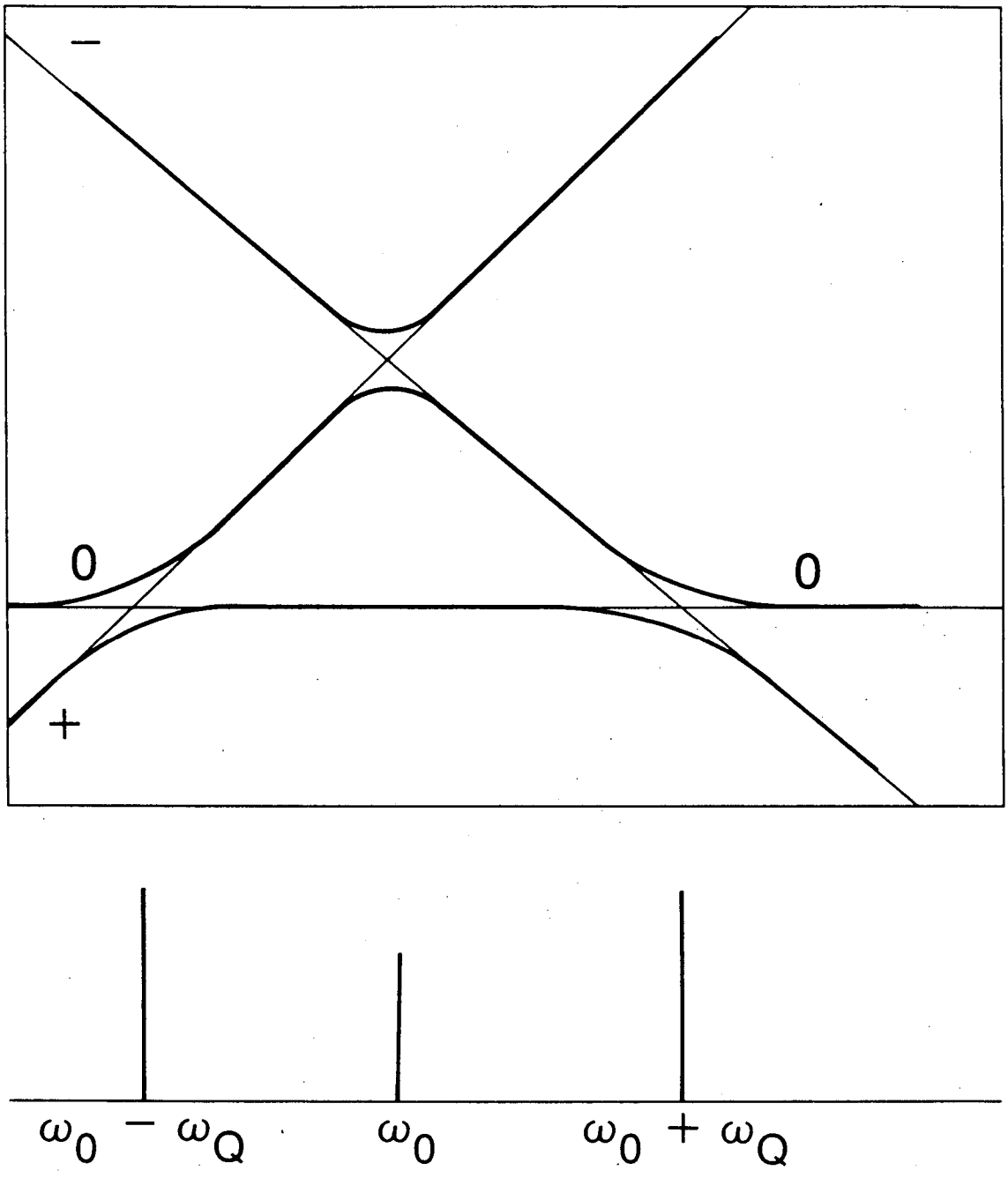

XBL 866-6310 A

Pines, Fermi Lectures, Figure 38

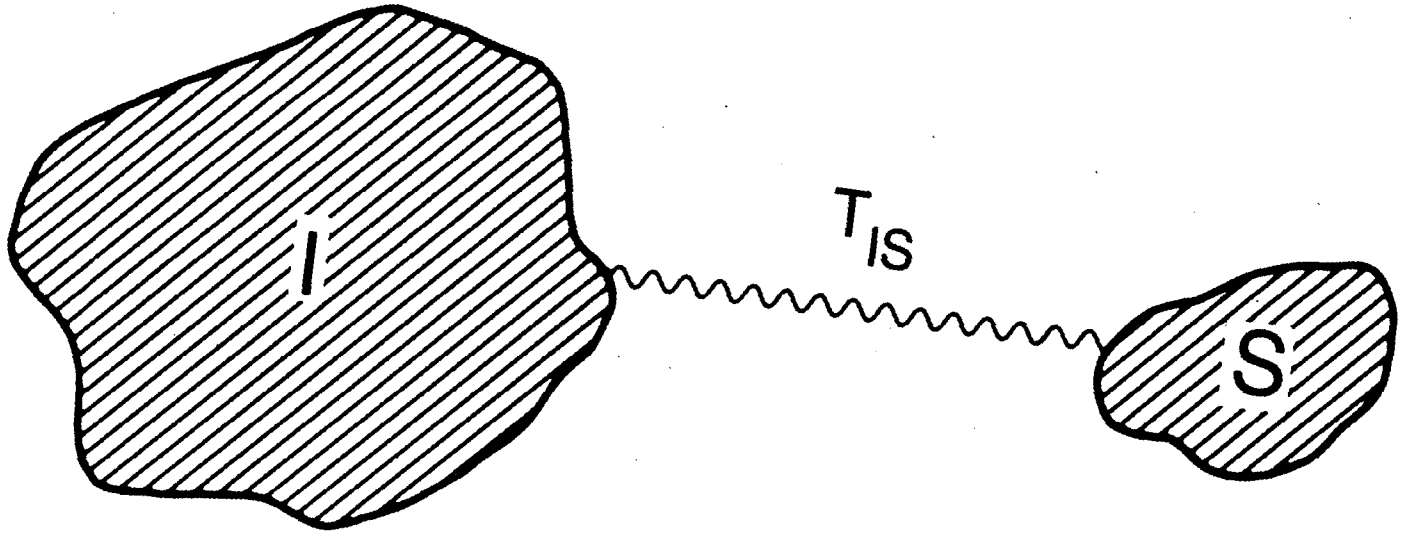

XBL 866-6328 A

Pines, Fermi Lectures, Figure 39

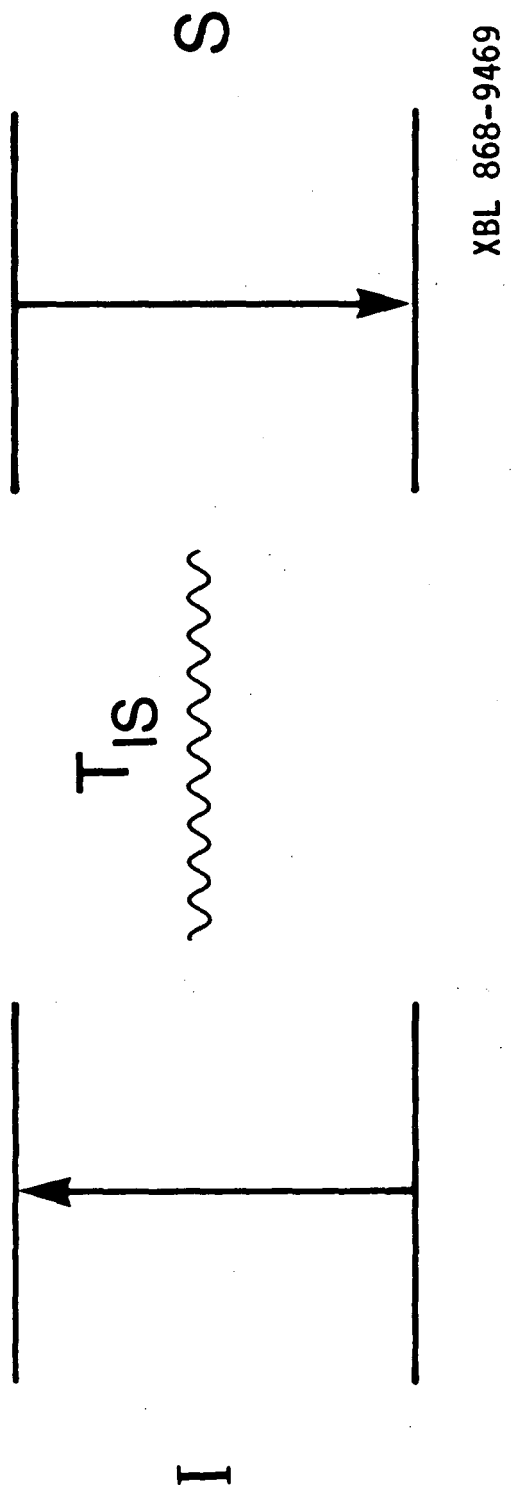

Pines, Fermi Lectures, Figure 40

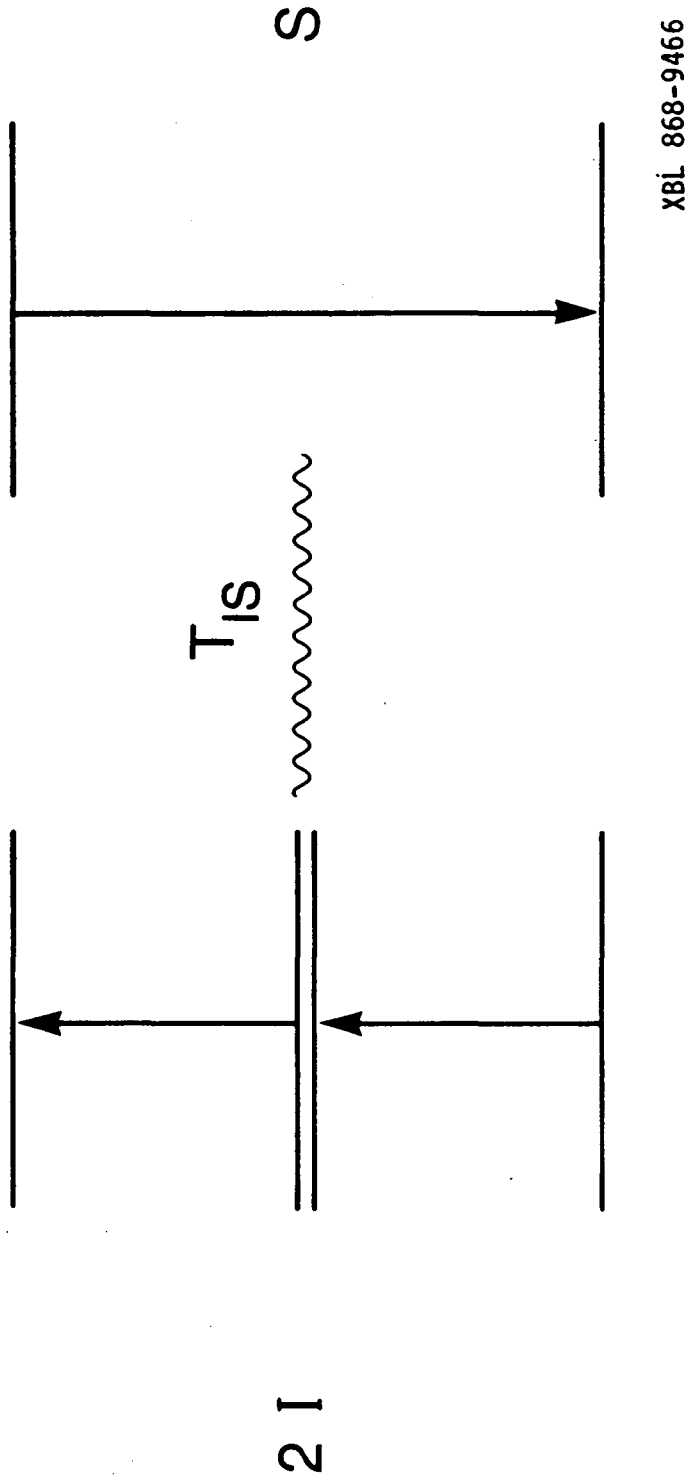

Pines, Fermi Lectures, Figure 41

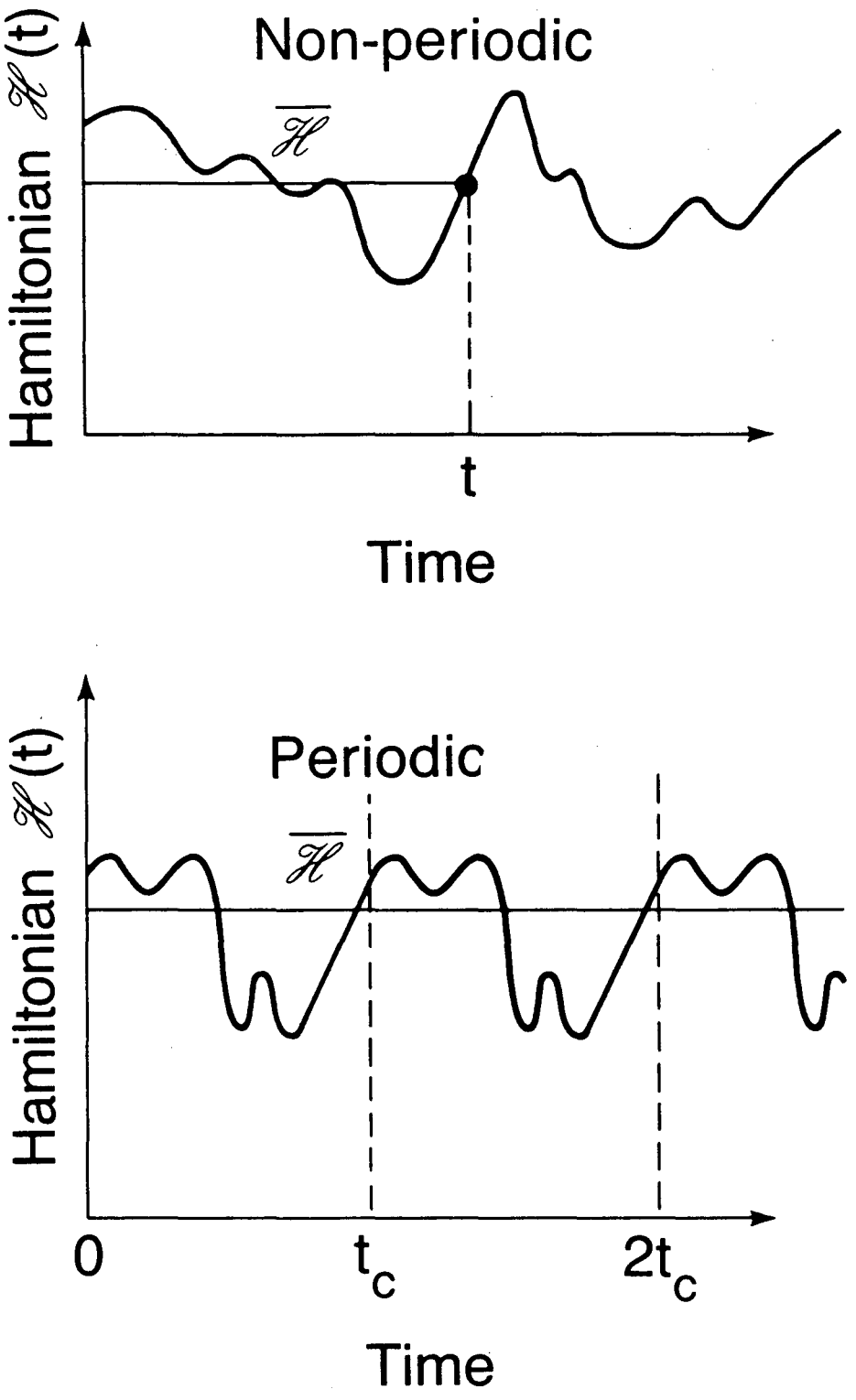

XBL 866-6323A

Pines, Fermi Lectures, Figure 42

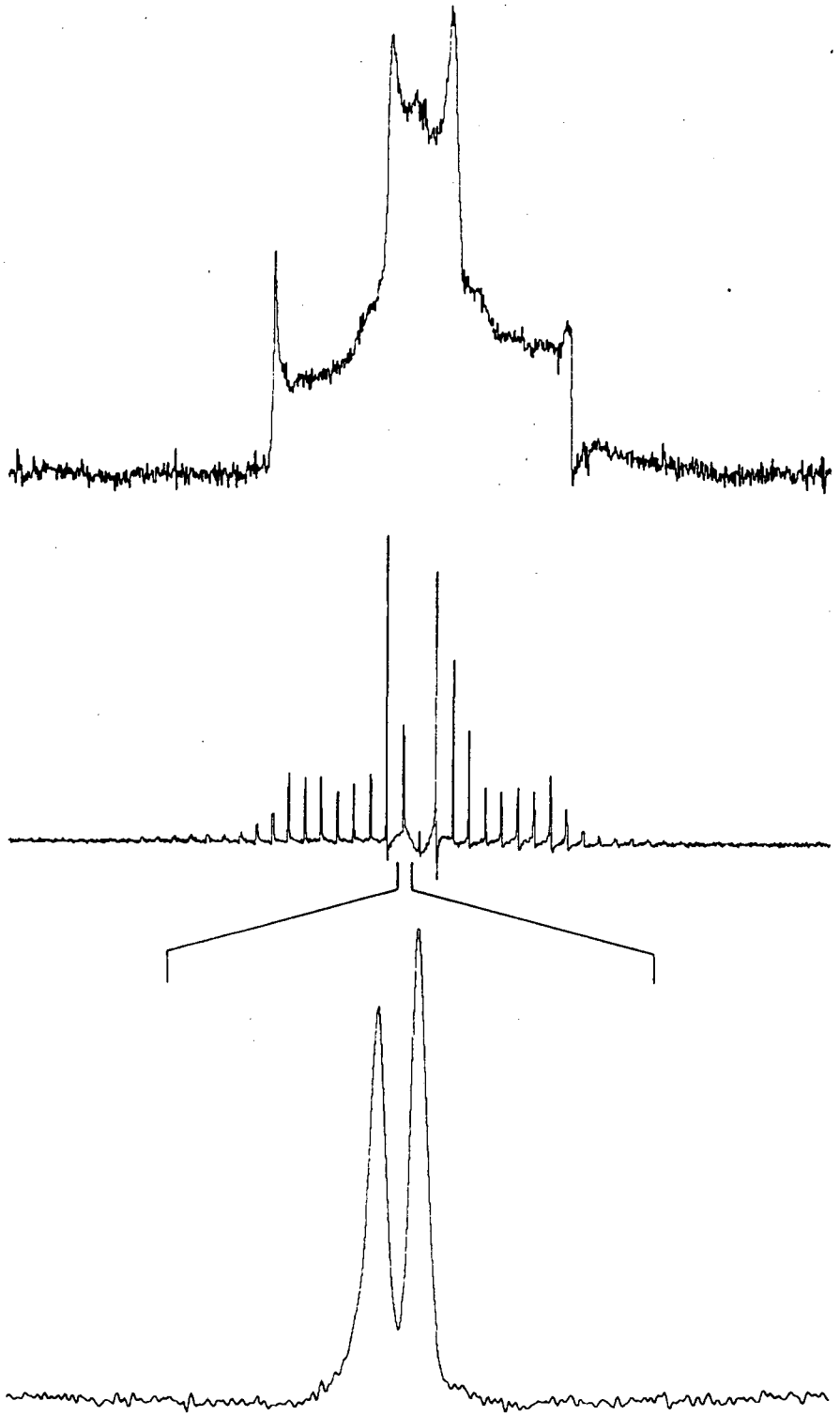

XBL 7710-6843

Pines, Fermi Lectures, Figure 43

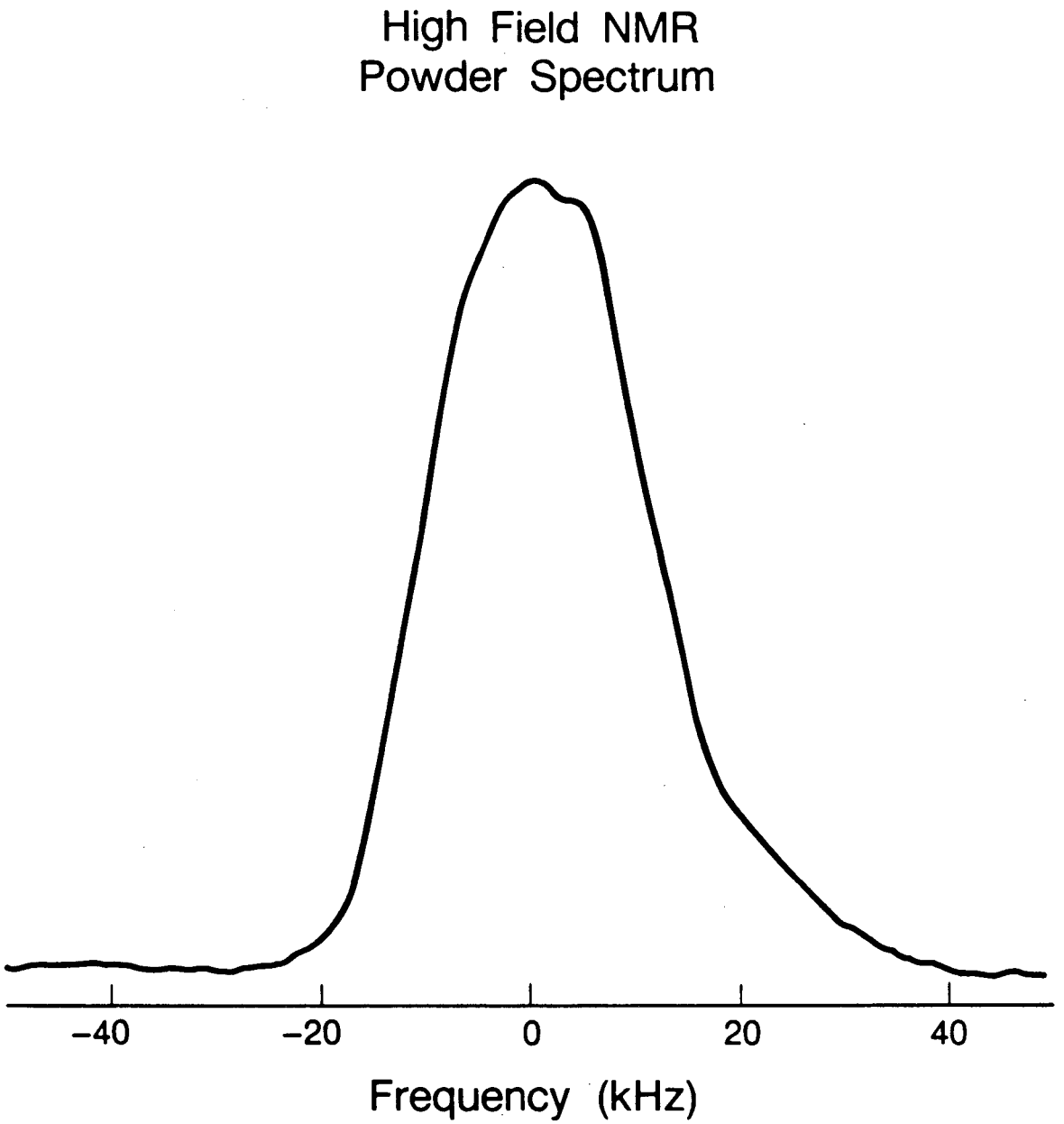

XBL 854-9808A

Pines, Fermi Lectures, Figure 44

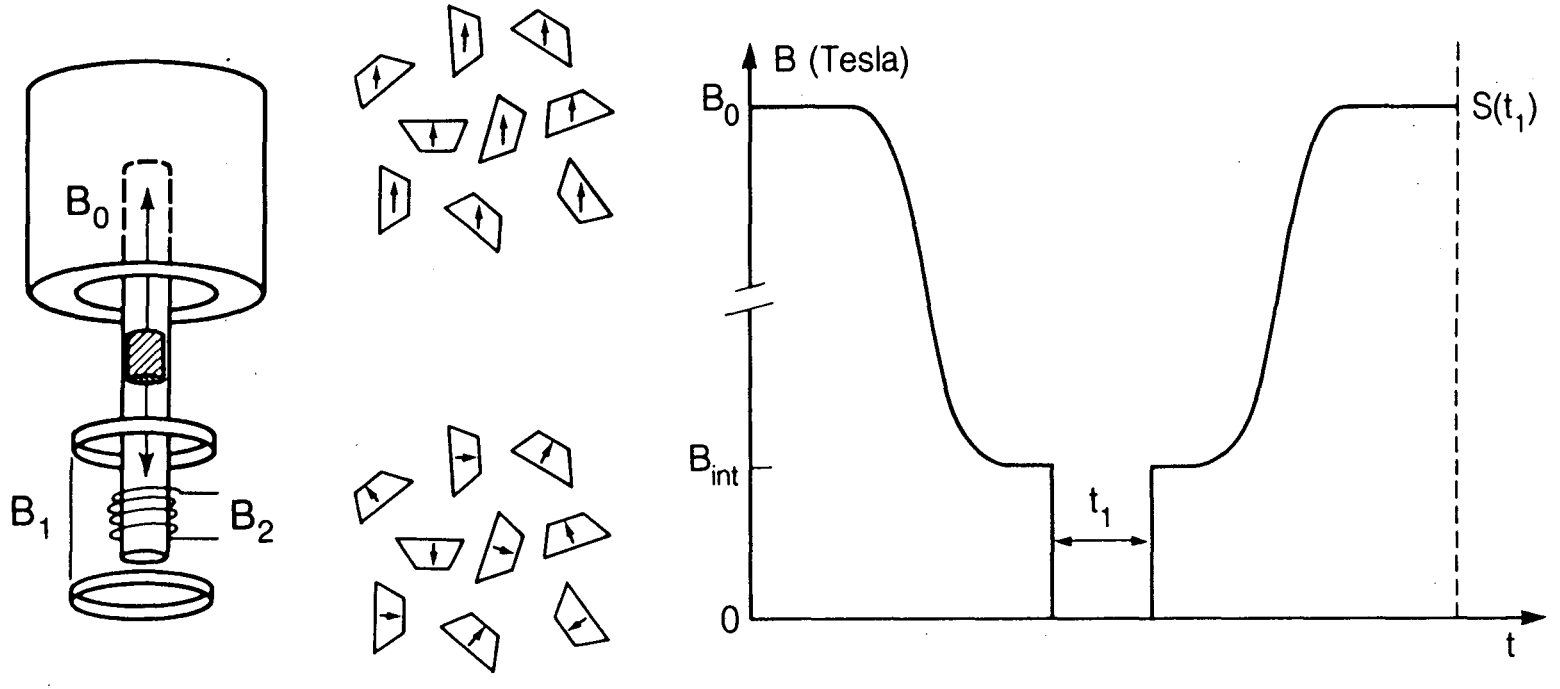

XBL 863-11046

Pines, Fermi Lectures, Figure 45

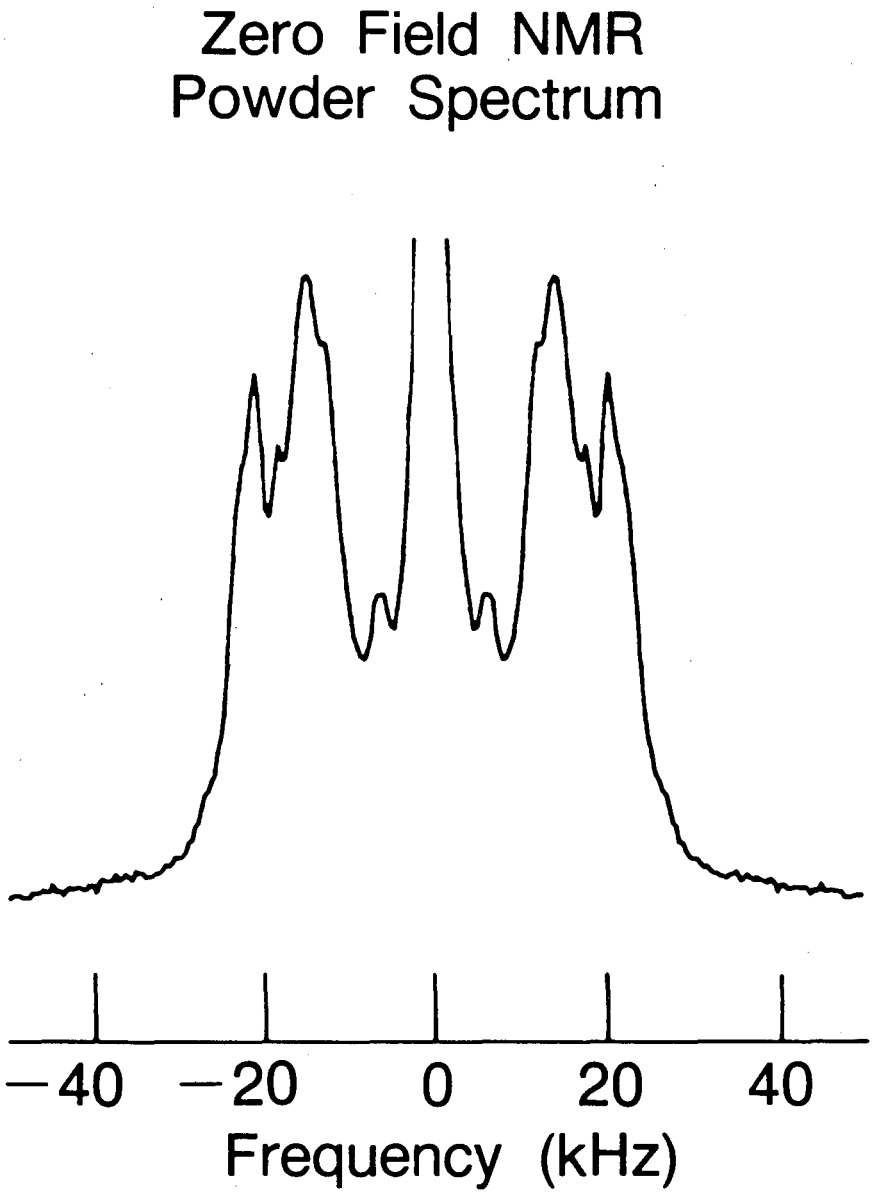

Pines, Fermi Lectures, Figure 46

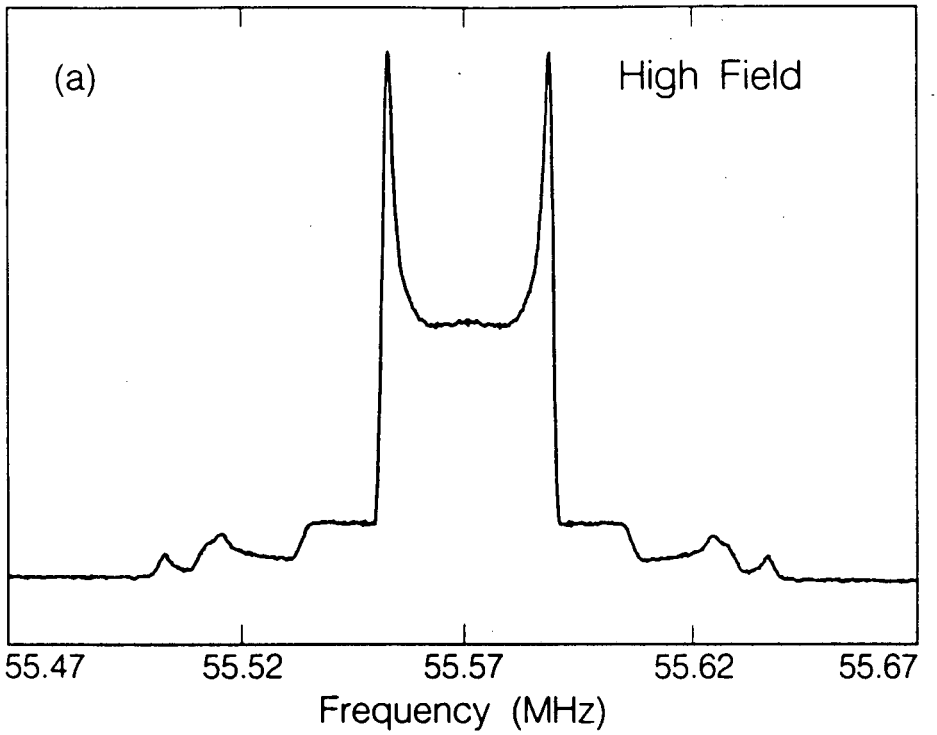

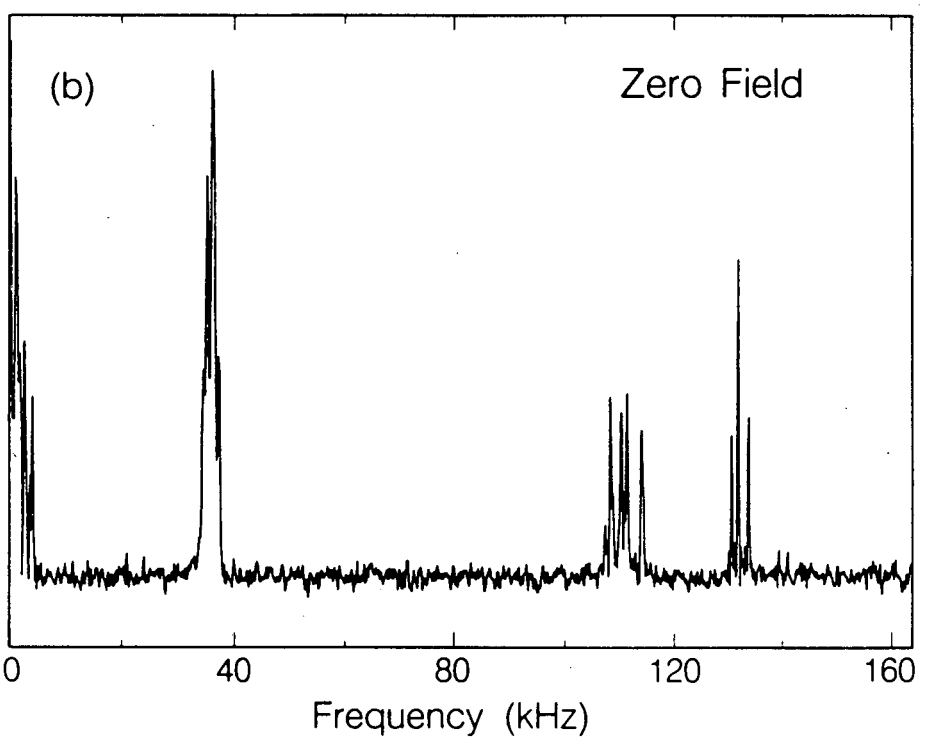

XBL 863-11045

Pines, Fermi Lectures, Figure 47

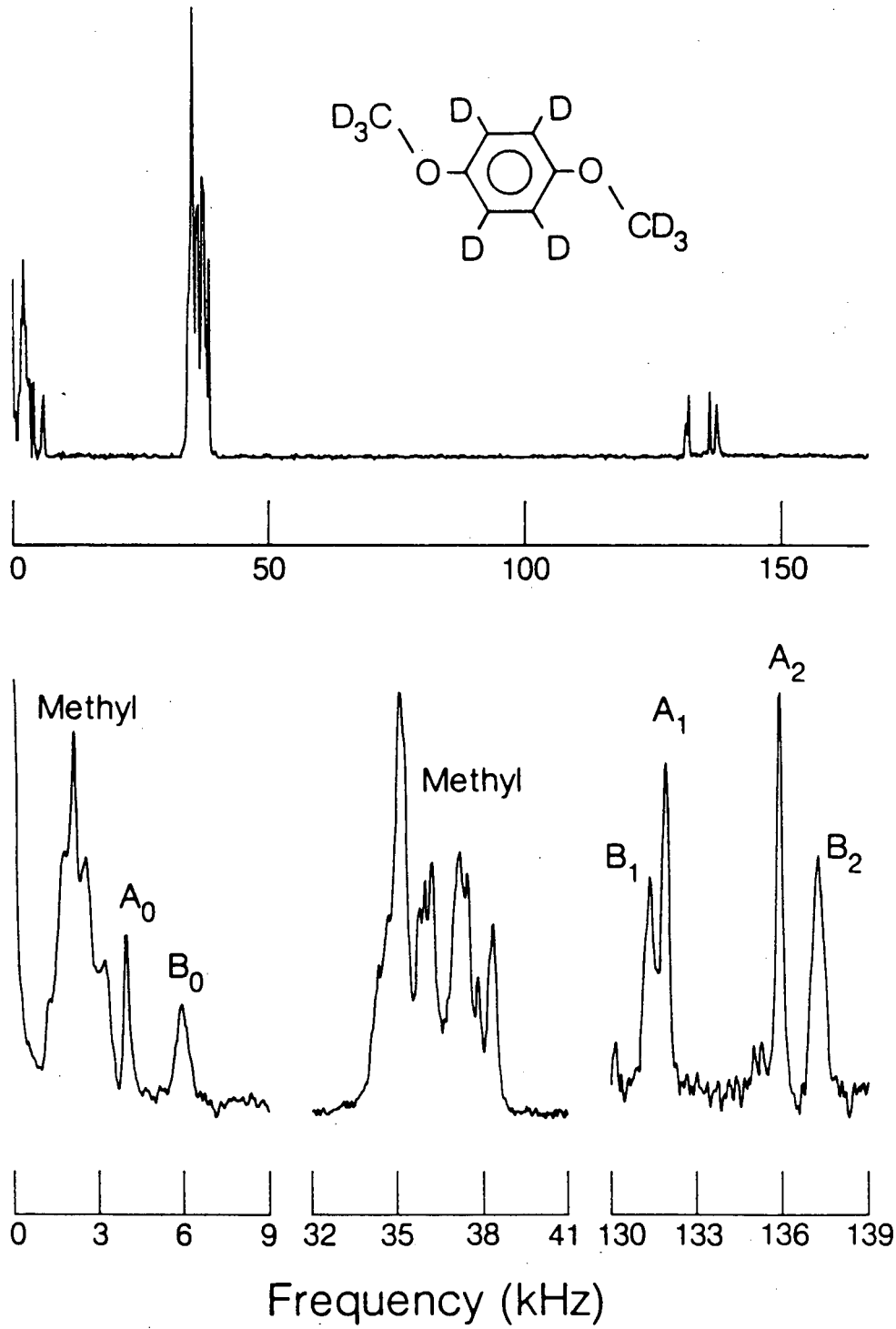

XBL 8310-12107

Pines, Fermi Lectures, Figure 48

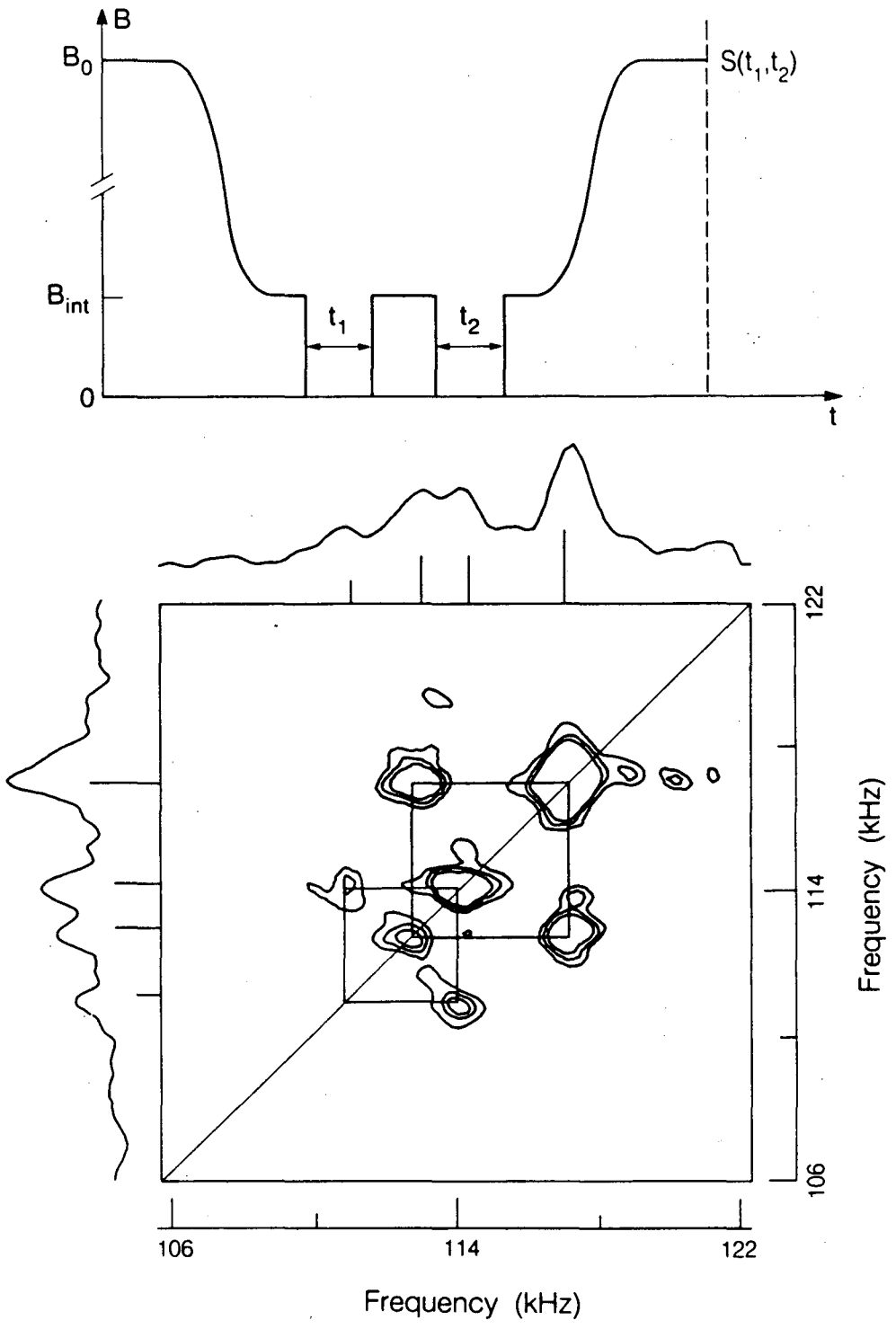

Pines, Fermi Lectures, Figure 49

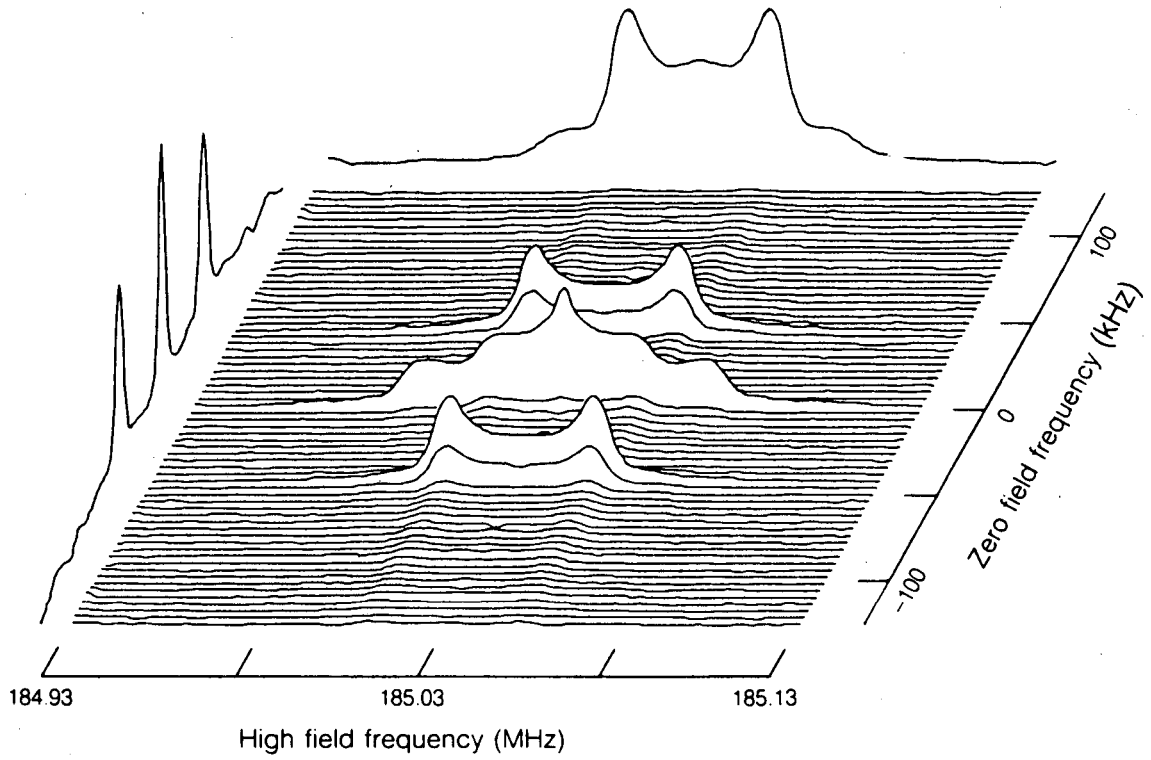

XBL 852-1105

Pines, Fermi Lectures, Figure 50

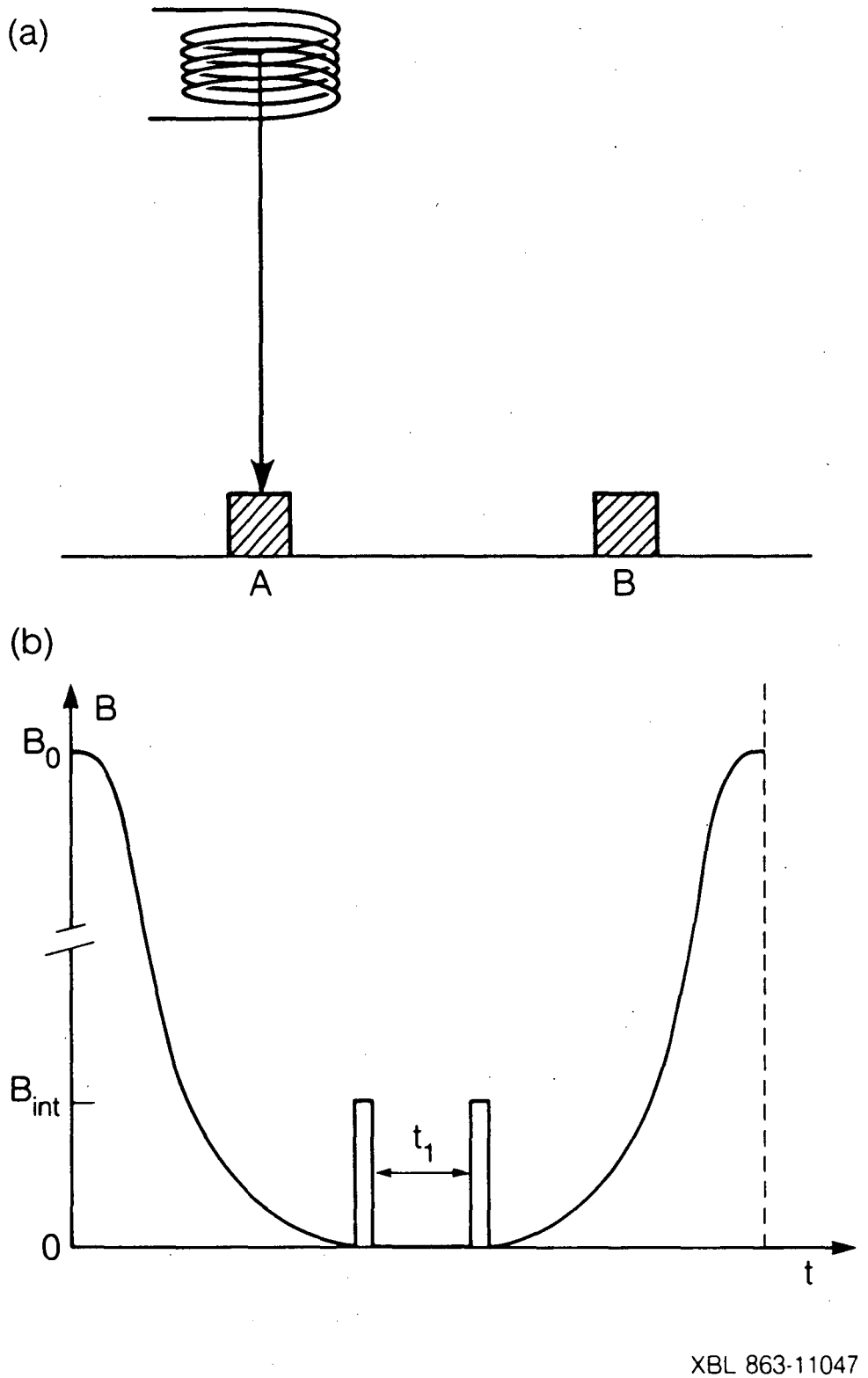

XBL 863-11047

Pines, Fermi Lectures, Figure 51

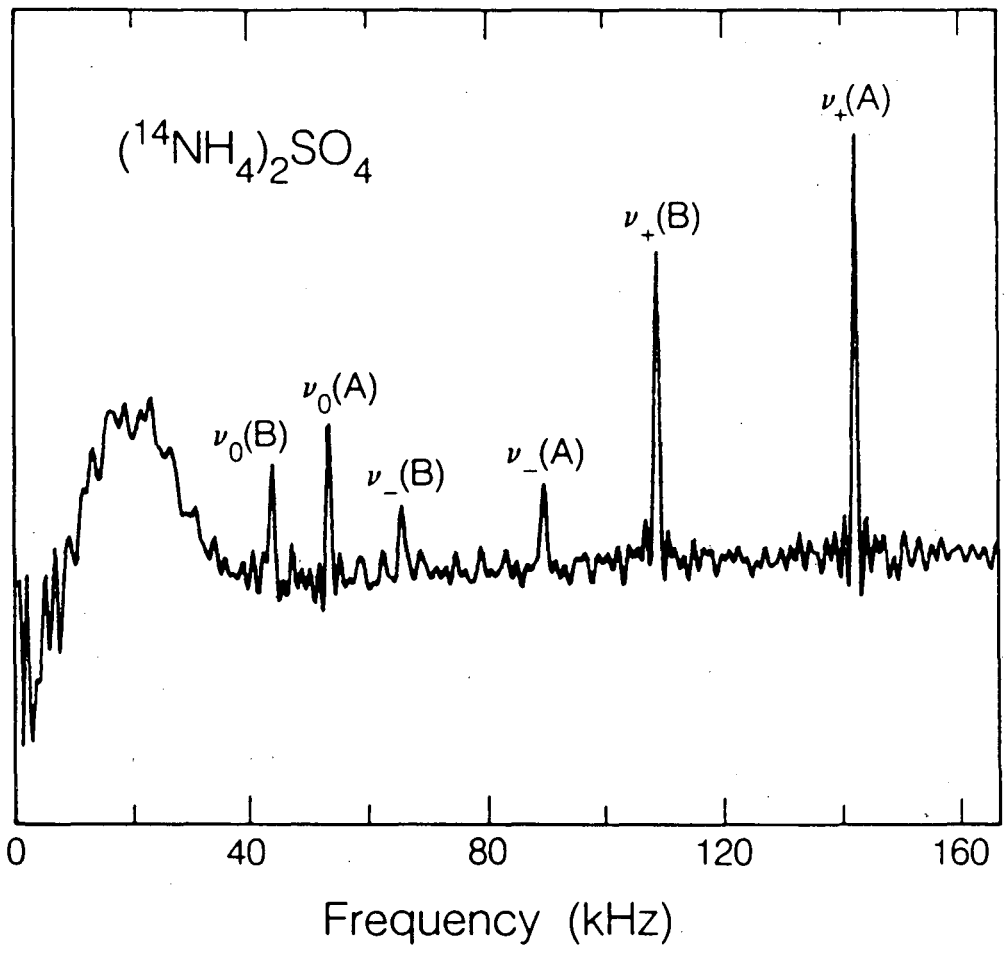

XBL 853-8830

Pines, Fermi Lectures, Figure 52

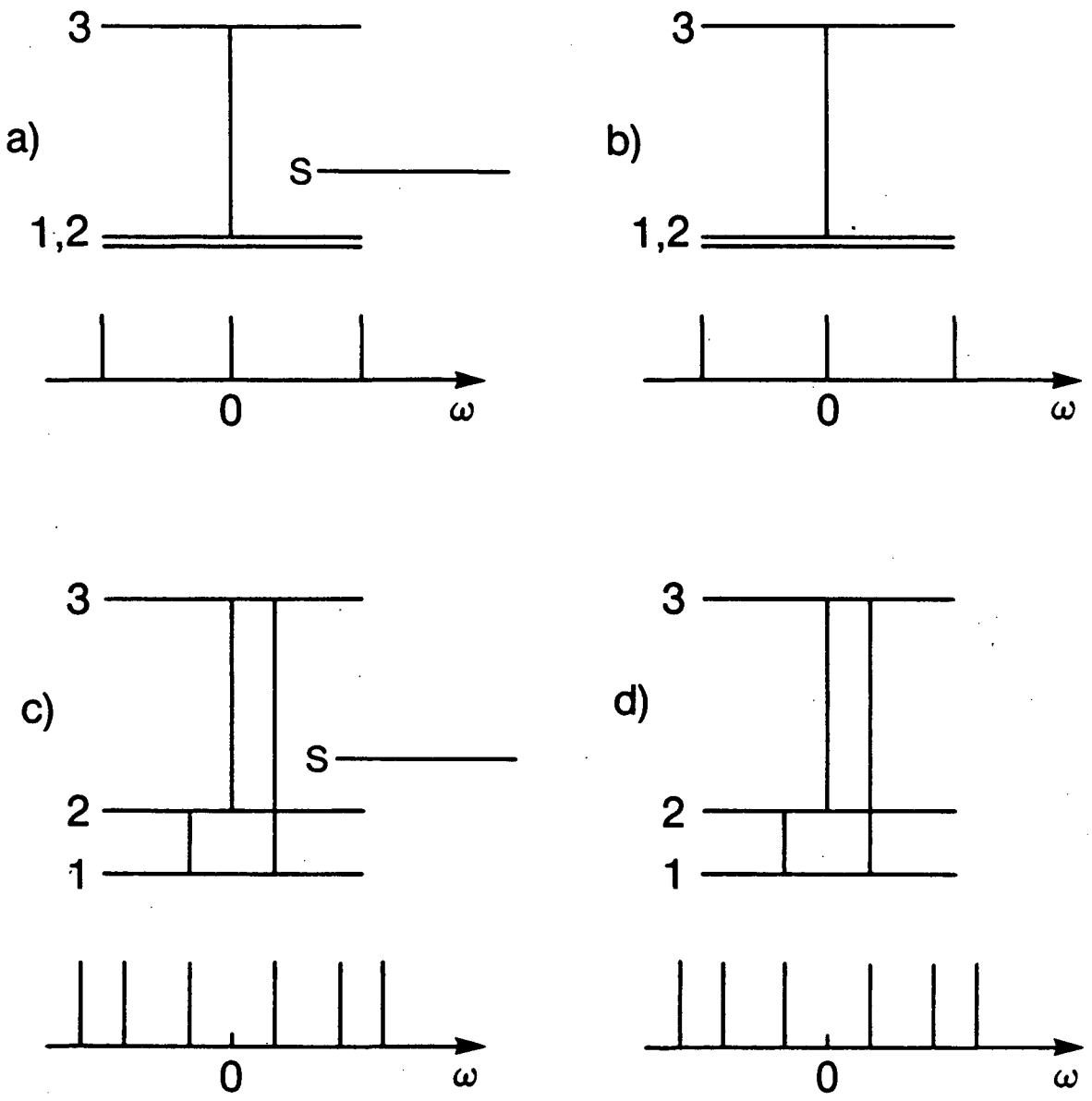

XBL 868-3204

Pines, Fermi Lectures, Figure 53

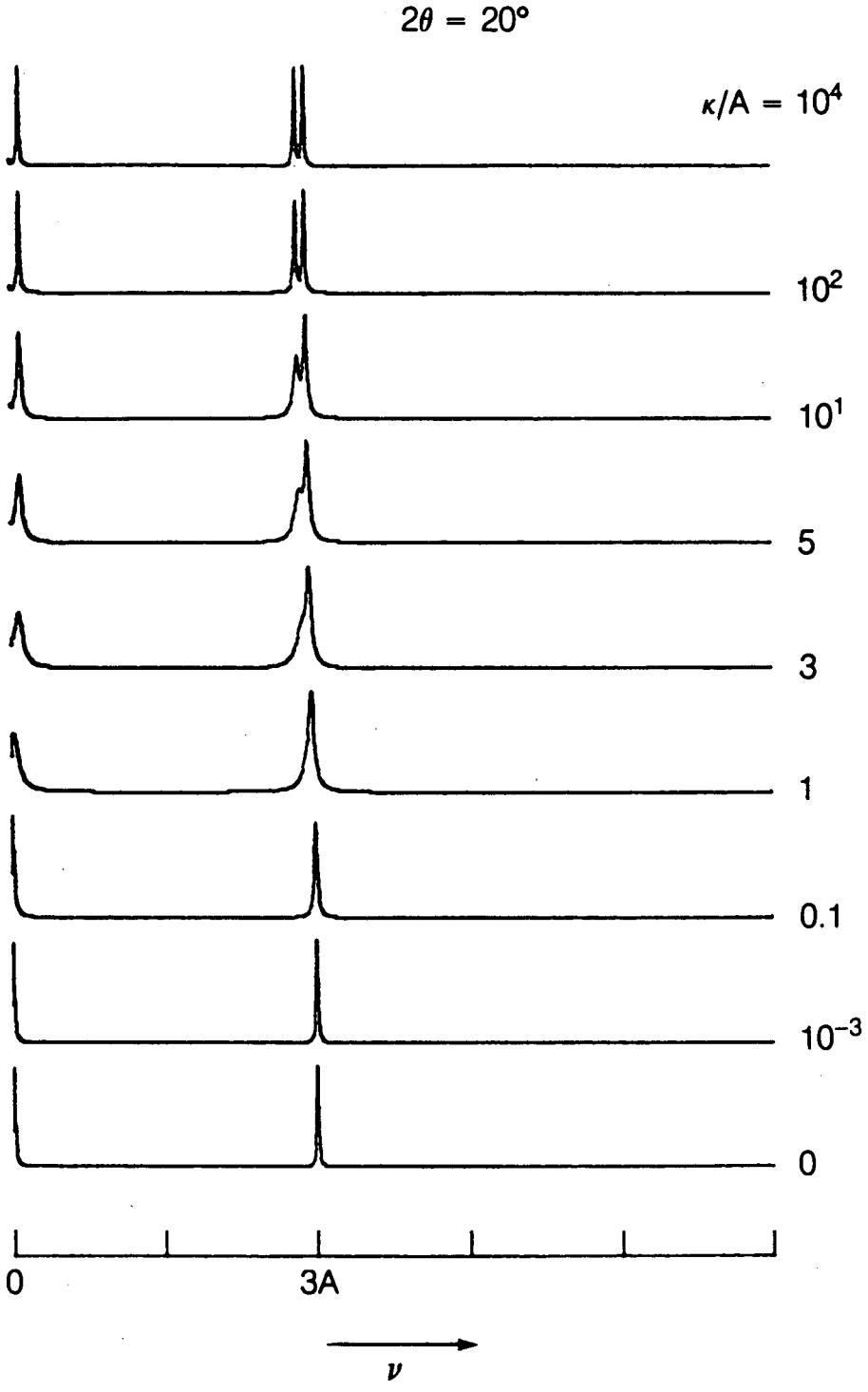

XBL 8511-12513

Pines, Fermi Lectures, Figure 54

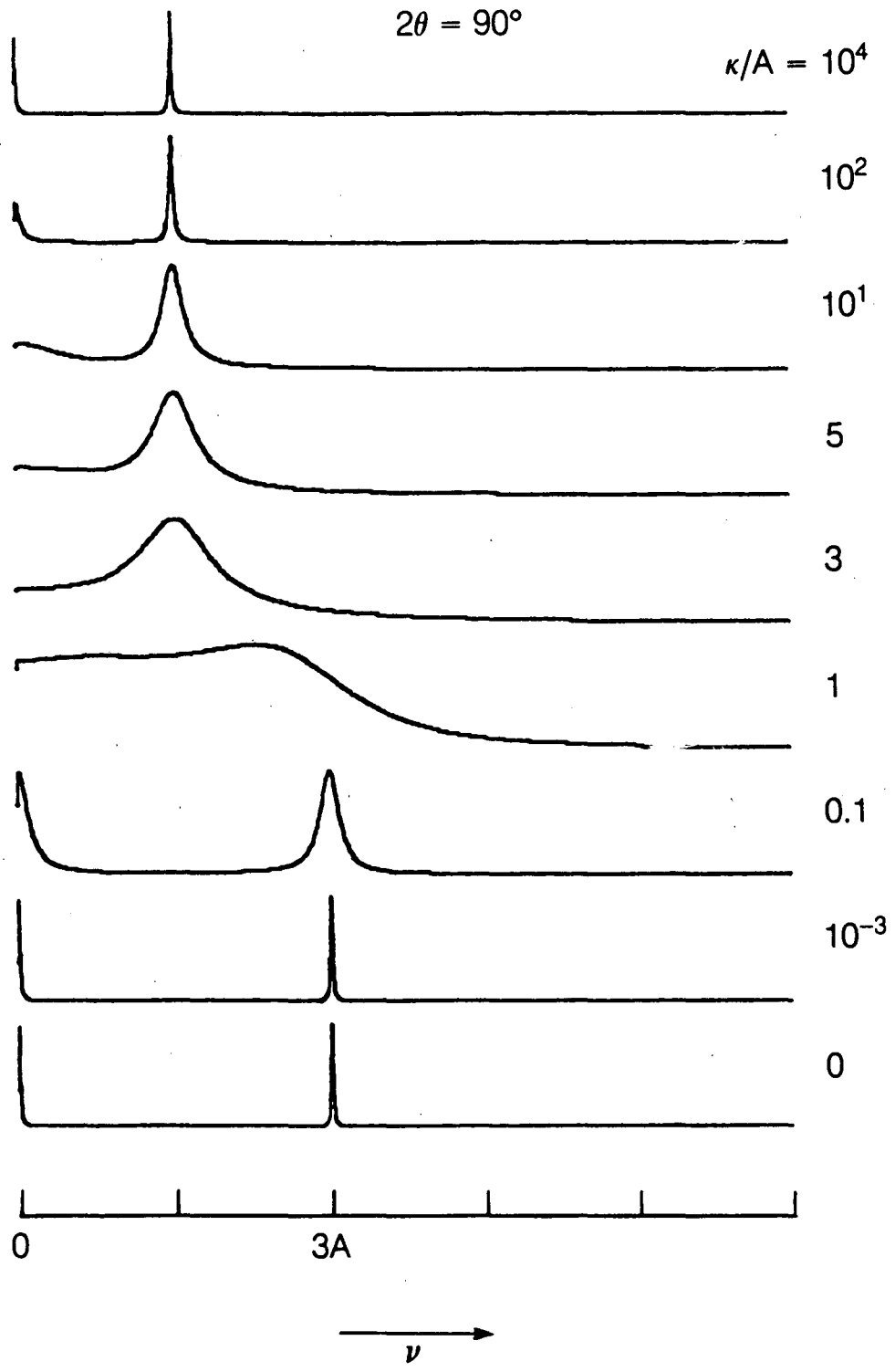

XBI 8511-12517

Pines, Fermi Lectures, Figure 55

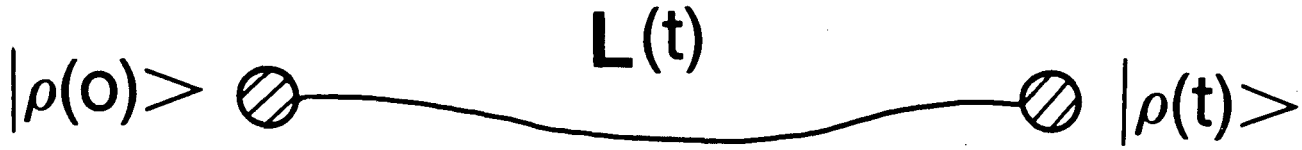

XBL 868-9472

Pines, Fermi Lectures, Illustration page 9

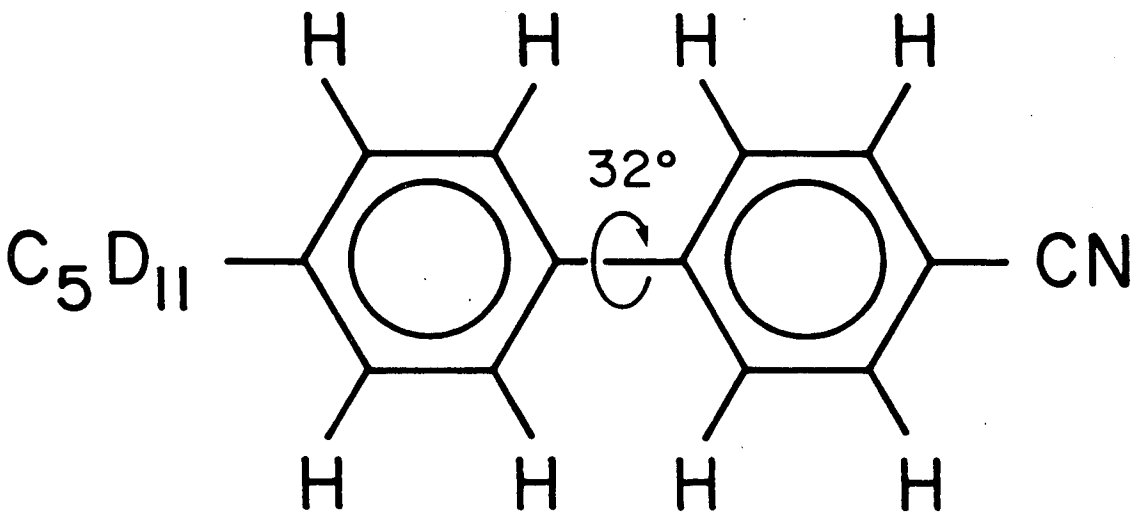

XBL 851-932

Pines, Fermi Lectures, Illustration page 19

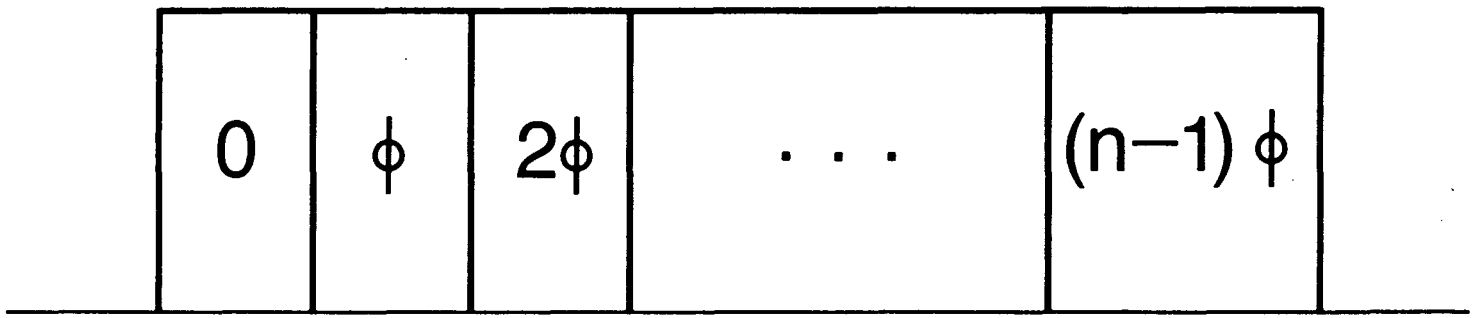

XBL-866-6351

Pines, Fermi Lectures, Illustration page 20

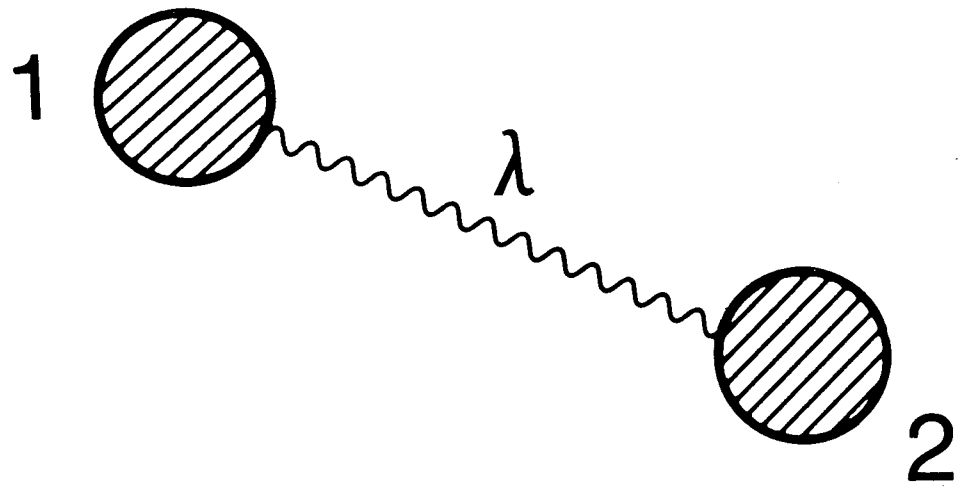

XBL-866-6324

Pines, Fermi Lectures, Illustration page 33.

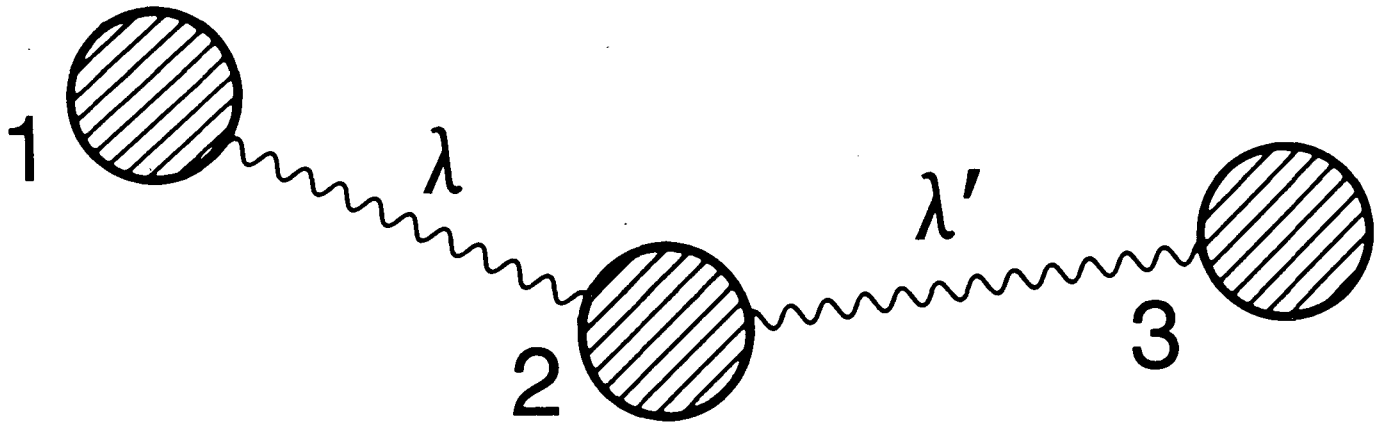

XBL-866-6325

Pines, Fermi Lectures, Illustration page 38.

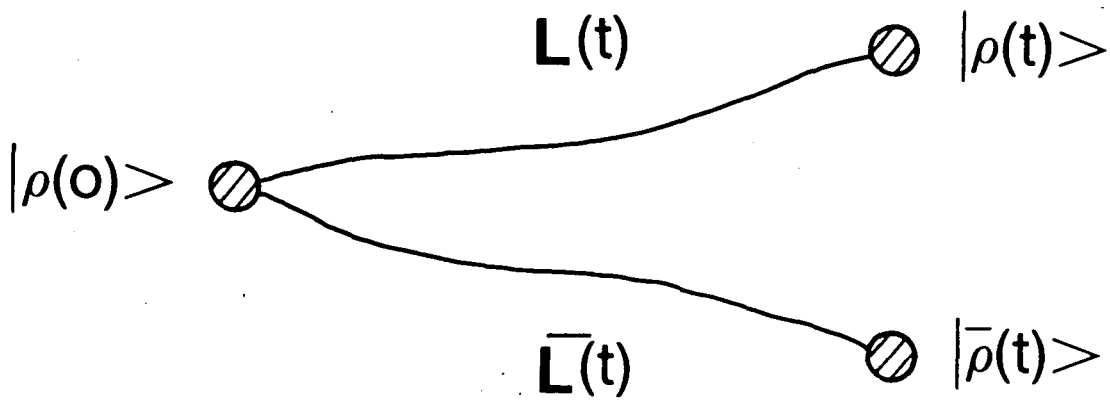

XBL 868-9471

Pines, Fermi Lectures, Illustration page 51.

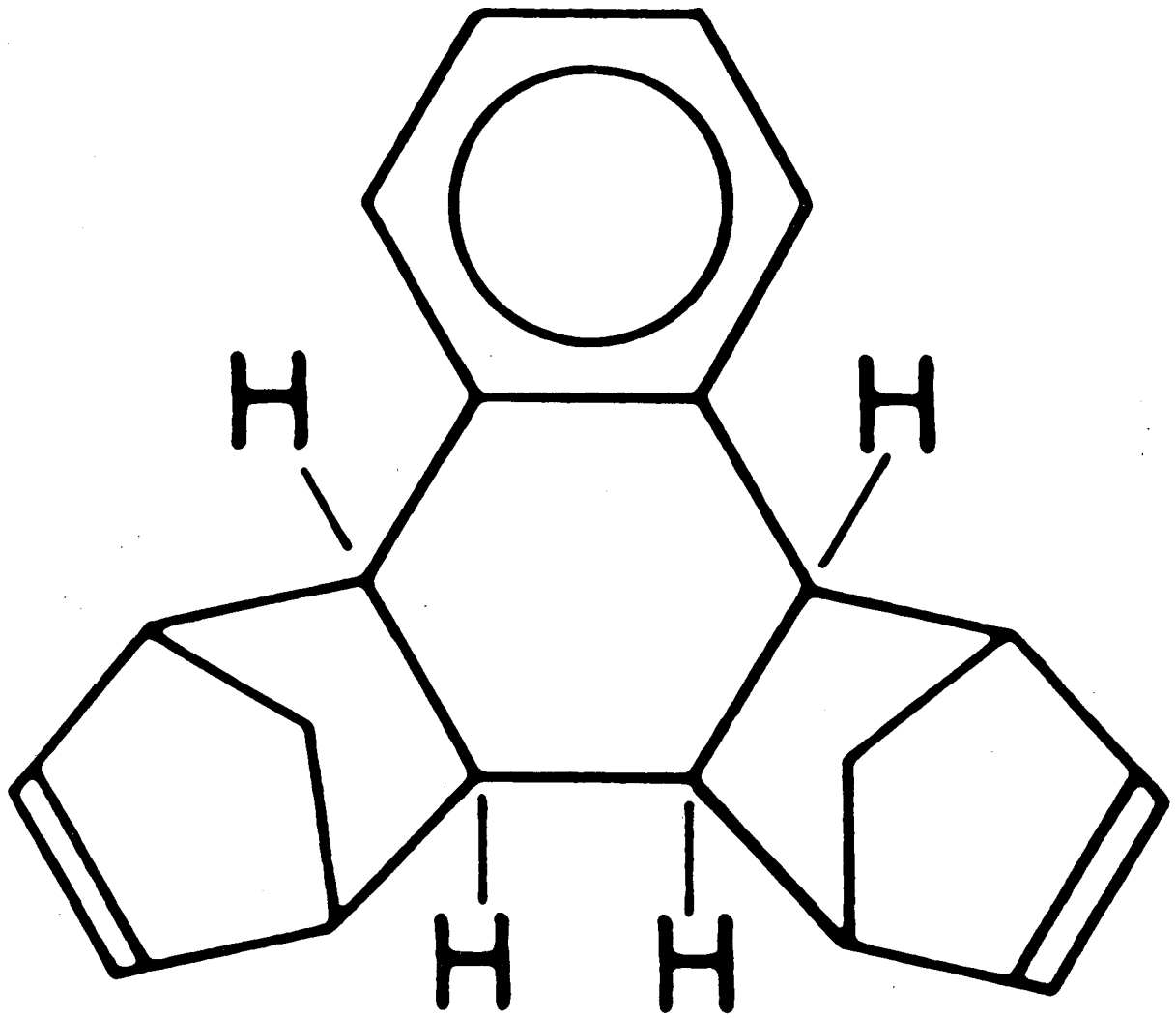

XBL 868-9470

Pines, Fermi Lectures, Illustration page 55.

LAWRENCE BERKELEY LABORATORY
TECHNICAL INFORMATION DEPARTMENT
UNIVERSITY OF CALIFORNIA
BERKELEY, CALIFORNIA 94720